University of Salerno
Department of Chemistry and Biology

Ph.D. Thesis in Chemistry

New Technologies in Tires: From Layered Nanofillers to Metathesis Reactions

Marco Mauro

Tutor: Prof. Gaetano Guerra
Co-tutors: Prof. Maurizio Galimberti, Dr. Luca Giannini
Supervisor: Prof. Pasquale Longo

XII Cycle 2011-2014

Dedicated to Sheila and to my wonderful family

The true sign of intelligence is not knowledge but imagination.

Albert Einstein

Abstract

Tires are annually manufactured in more than one billion of artefacts and the ever increasing demand is on the basis of the efforts in finding new solutions for more performant, sustainable and durable products. This PhD thesis presents highly new contributions to the nanotechnology applied to rubber nanocomposites, particularly focussing on clays and graphitic fillers with tunable periodicities and degree of order of their structures. The interaction of layered nanofillers with the rubber matrix was investigated, correlating nanocomposites structure and morphology, studied by means of X-ray diffraction and transmission electron microscopy, with measured tensile and dynamic-mechanical properties. Unique reversible thermal transitions of nanocomposites containing organoclays and graphite oxide intercalation compounds were also investigated through differential scanning calorimetry. Metathesis applied to the rubber chemistry is presented as a strongly innovative technology to produce novel rubber materials, hardly obtainable with conventional synthetic methods and to promote the degradation of rubbers, when the latter process is desired.

Abbreviations

2HT: Dimethyl ditallow ammonium
6PPD: N-(1,3-dimethylbutyl)-N′-phenyl-1,4-benzenediamine
ADMET: Acyclic diene metathesis polymerization
AIPEA: Association Internationale pour l'Etude des Argiles
B_C: 1,4-*cis*-butadiene unit
BET: Brunauer-Emmett-Teller
B_T: 1,4-*trans*-butadiene unit
B_V: 1,2-butadiene unit
CB: Carbon black
CEC: Cation-exchange-capacity
CM: Cross-metathesis
CMS: Clay Minerals Society
CNTs: Carbon nanotubes
CRGO: Chemically reduced graphite oxide
CTAB: Cetyl trimethylammonium bromide
Cy: Cyclohexyl group
DBP: Dibutyl phthalate
DCB: 1,2-dichloro benzene
DCBS: N-dicyclohexylbenzothiazol-2-sulfenamide
DCUP: Dicumylperoxide
DMA: Dynamic-mechanical analysis
DSC: Differential scanning calorimetry
DTGS: Deuterated triglycine sulfate
eGO: Exfoliated graphite oxide
FTIR: Fourier transform infrared spectra
$FWHM_D$: Full width at half maximum of the D-band in the Raman spectra of a graphitic material
G: High surface area graphite
G1: First generation Grubbs catalyst
G2: Second generation Grubbs catalyst

GICs: Graphite intercalation compounds
GO/2HT/GTS: Graphite oxide intercalated with dimethyl ditallow ammonium and glyceryl tristearate
GO/2HT/SAES: Graphite oxide intercalated with dimethyl ditallow ammonium and 2-stearamidoethyl stearate
GO/2HT-H: Graphite oxide intercalated with higher content of dimethyl ditallow ammonium
GO/2HT-L: Graphite oxide intercalated with lower content of dimethyl ditallow ammonium
GO/PP2: Graphene oxide layers functionalized with second generation phosphinated Piers catalyst
GO: Graphite oxide
GO-Cl: Chlorinated Graphene oxide layers
GO-G2: Graphene oxide layers functionalized with second generation Grubbs catalyst
GO-Gly: GO-Cl esterified with ethylene glycol
GOICs: Graphite oxide intercalation compounds
GO-Nor: GO-Gly reacted with 5-acid chloride 2-norbornene
GPC: Gel permeation chromatography
GTS: Glyceryl tristearate
HG1: First generation Hoveyda-Grubbs catalyst
HG2: Second generation Hoveya-Grubbs catalyst
H-GO: Graphite oxide with higher oxygen content
HT: Hydrotalcite
Ic: 1,4-*cis*-isoprene unit
iPr: Isopropyl group
It: 1,4-*trans*-isoprene unit
JNCs: Joint Nomenclature Committees of the AIPEA and the CMS
LDH: Layered double hydroxides
L-GO: Graphite oxide with lower oxygen content
MCM: Macromolecular cross-metathesis
Me: Methyl group
MMT/2HT/SA: Montmorillonite intercalated with dimethyl

ditallow ammonium and stearic acid (also referred as **OC 6nm**)

MMT/2HT/SAES: Montmorillonite intercalated with dimethyl ditallow ammonium and 2-stearamidoethyl stearate

MMT/2HT: Montmorillonite intercalated with dimethyl ditallow ammonium (also referred as **OC 4nm**)

MMT: Montmorillonite

MWCNTs: Multi-wall carbon nanotubes

NHC: *N*-heterocyclic carbene

NMR: Nuclear magnetic resonance

NXT: 3-octanoylthio-1-propyltriethoxysilane

O: Octahedral sheet within a clay Layer

OC 2.5nm: OC obtained by extraction of MMT/2HT with ethyl acetate

OCs: Organically modified clays

PBR: 1,4-*cis*-polybutadiene

Ph: Phenyl group

Phr: Parts per hundred grams of rubber

PIR/GO: PIR grafted to GO sheets

PIR/H: PIR-based nanocomposites containing GO/2HT-H

PIR/L: PIR-based nanocomposites containing GO/2HT-L

PIR/OCs: PIR-based nanocomposites containing OCs (OC 4nm, OC 6nm an OC 2.5nm)

PIR: 1,4-*cis*-polyisoprene

RCM: Ring-closing metathesis

rGO: Reduced graphite oxide

ROM: Ring-opening metathesis

ROMP: Ring-opening metathesis polymerization

RT: Room temperature

SA: Stearic acid

SAES: 2-stearamidoethyl stearate

$scCO_2$: Supercritical carbon dioxide

SEM: Scanning electron microscopy

SIC: Strain-induced crystallization

sPS/OC: sPS aerogels containing OCs
sPS/rGO: sPS aerogels containing rGO
sPS: Syndiotactic polystyrene
SWCNTs: Single-wall carbon nanotubes
T: Tetrahedral sheets within a clay Layer
TGA: Thermogravimetric analysis
THF: tetrahydrofuran
TMS: Tetramethylsilane
WAXD: Wide angle X-ray diffraction

Symbols

%mol.: Mole percent
%wt.: Weight percent
x_{hkl}: Angle between the normal to the film surface and the normal to the hkℓ crystallographic plane
χ_{hkl}: Azimuthal angle measured from the equator of the Debye ring
$I(\chi_{hkl})$: Intensity distribution of a hkℓ diffraction on the Debye ring
$\overline{M}_n$**:** Number average molecular mass
$\overline{M}_w / \overline{M}_n$**:** Polydispersity index
$\overline{\cos^2 x_{hkl}}$: Squared average cosine value of the angle x_{hkl}
2θ: Peak position in a X-ray diffraction pattern
a: Crystallographic a axe
A: sp^2-hybridized carbon layer within the …$ABABAB$… stacking sequence of the hexagonal graphite
a_0: a_0 lattice constant of the hexagonal graphite
A_C: Cross-section perpendicular to the outstretched hydrocarbon chains
a_g: a_g lattice constant of the graphite oxide
a_o: a_o lattice constant of the orthorhombic order
a_r: a_r lattice constant of the hexagonal rotator order
A_S: Available clay surface per amphiphile
b: Crystallographic b axe
B: sp^2-hybridized carbon layer within the …$ABABAB$… stacking sequence of the hexagonal graphite
c: Crystallographic c axe
c_0: c_0 lattice constant of the hexagonal graphite
$D_\parallel / D_\perp$: Shape anisotropy
$D_\parallel$: In-plane correlation length

$D_{\perp}$: Out-of-plane correlation length
$d_{hk\ell}$: Bragg’s distance between hkℓ lattice planes
$D_{hk\ell}$: Correlation length perpendicular to hkℓ lattice planes
E': Tensile storage modulus
$f_{hk\ell}$: Degree of uniplanar orientation of the crystallites with respect to the film plane
g: Reflection relative to the graphite oxide planes
G'': Shear loss modulus
G': Shear storage modulus
hkℓ: Miller indices for a family of lattice planes in a crystal structure
K: Scherrer constant
n: Stage number or number of graphene layers that separate adjacent intercalate layers in GICs
o: Reflection relative to the orthorhombic order
P/P_0: Ratio between the measured pressure and the atmospheric pressure
p: p orbital
P: Porosity of sPS aerogels
r: Reflection relative to the hexagonal rotator order
S_{BET}: Total area evaluated following the BET model in the standard $0.05<P/P_0<0.3$ pressure range
sp^2: sp^2 carbon hybridization
sp^3: sp^3 carbon hybridization
$\tan\delta$: Loss tangent
T_g: Glass transition temperature
α layer: Type of layers of hydrocarbon chains with orthorhombic order in the interlayer space
β layer: Type of layers of hydrocarbon chains with orthorhombic order in the interlayer space
$\beta_{hk\ell}$: Integral breadth, defined as the ratio between the integral intensity and the maximum intensity of a diffraction peak
ΔH_m: Melting enthalpy

ΔH_r: Enthalpy relative to the loss of rotator order of the intercalated hydrocarbon chains
$\varepsilon_{\parallel}$: In-plane lattice strain
$\varepsilon_{\perp}$: Out-of-plane lattice strain
ε_B: Elongation at break
θ: Diffraction angle
λ: Wavelength of the incident X-rays (1.5418 Å, Cu Kα radiation)
π: pi C-C bond
ρ_{app}: Aerogel apparent density calculated from the mass/volume ratio of the monolithic aerogels
ρ_{pol}: Density of polymer (sPS) matrix
σ: Sigma C-C bond
σ_B: Tensile strength
φ: Tilting angle of the hydrocarbon chains with respect to the normal to the clay or graphite oxide layers

Contents

Abstract / v
Abbreviations / vii
Symbols / xi
Introduction / 1
Section 1 Layered Nanofillers for Rubber Nanocomposites / 3
Chapter 1 Cationic Clays and Organoclays / 5
- 1.1 Clays and Their Structures / 5
  - 1.1.1 Multiscale Organization of Clays / 8
- 1.2 Organoclays / 10
  - 1.2.1 Preparation of Organoclays at the Solid State / 13
  - 1.2.2 Characterization of Organoclays / 14
  - 1.2.3 Structural Reversibility of Organoclays with Temperature / 18
  - 1.2.4 Structures of Organoclays / 21
- 1.3 Clay Exfoliation and Polymer/Clay Aerogels by Supercritical Carbon Dioxide / 23
  - 1.3.1 Organoclay Exfoliation by Supercritical Carbon Dioxide / 26
  - 1.3.2 Monolithic Nanoporous Polymeric Aerogels with Large Organoclay Content / 28
  - 1.3.3 Comparison between Aerogels with Intercalated and Exfoliated Organoclays / 32
- References / 36

Chapter 2 Graphites and Derived Compounds / 41
- 2.1 Carbon Allotropes / 42
- 2.2 Structures of Layered Carbons / 43

        - 2.2.1 Graphites / 43
        - 2.2.2 Turbostratic Graphites / 45
        - 2.2.3 Amorphous Carbons / 47
        - 2.2.4 Carbon Blacks / 48
    - 2.3 Structural Characterization of Graphitic Materials for the Preparation of Anisotropic Carbon Nanofillers / 50
    - 2.4 Graphite Oxide / 54
        - 2.4.1 Preparation, Composition and Surface Areas of Graphite Oxide Samples / 55
        - 2.4.2 Characterization of Graphite Oxide Samples / 57
    - 2.5 Graphite and Graphite Oxide Intercalation Compounds / 61
        - 2.5.1 Preparation and Composition of Graphite Oxide Intercalation Compounds / 63
        - 2.5.2 Characterization of Graphite Oxide Intercalation Compounds / 64
        - 2.5.3 Structural Reversibility of Graphite Oxide Intercalation Compounds with Temperature / 65
        - 2.5.4 Structures of Graphite Oxide Intercalation Compounds / 70
    - 2.6 Disordered Structures from Graphite Oxide: Chemically Modified Graphenes / 76
        - 2.6.1 Chemical Exfoliation of Graphite Oxide / 77
        - 2.6.2 Mechanical Exfoliation of Graphite Oxide / 83
        - 2.6.3 Syndiotactic Polystyrene Aerogels with Reduced Graphite Oxide / 88
    - References / 94

Section II Rubber Nanocomposites / 103

Chapter 3 Rubber/Organoclay Nanocomposites / 105

    - 3.1 Structure and Morphology of Organoclays in Rubber

Nanocomposites / 105
3.2 Properties of Rubber/Organoclay Nanocomposites / 112
References / 115
Chapter 4 Rubber/Graphite Oxide Intercalation Compound Nanocomposites / 117
4.1 Structure and Morphology of Graphite Oxide Intercalation Compounds in Rubber Nanocomposites / 117
4.2 Properties of Rubber/Graphite Oxide Intercalation Compound Nanocomposites / 120
References / 125
Section III Metathesis Reactions in Rubber Chemistry / 127
Chapter 5 Olefin Metathesis / 129
5.1 Introduction / 129
5.2 Grubbs Catalysts / 132
References / 135
Chapter 6 Rubber-Scrambling Metathesis Reactions / 137
6.1 Macromolecular Cross-Metathesis / 137
6.2 Multiblock Copolymers of High-*cis* Polybutadiene and Polyisoprene by Macromolecular Cross-metathesis / 141
  6.2.1 Characterization of the Starting Homopolymers / 142
  6.2.2 Characterization of the PBR-PIR Copolymers / 148
  6.2.3 Extraction of PBR-PIR Copolymers with Solvent / 154
6.3 Metathetic Degradation of Rubbers / 158
  6.3.1 Degradation of Homopolymers / 158

6.3.2 Degradation of PBR-PIR Mixtures / 160
References / 164
Chapter 7 Grafting of Rubbers to Graphene Oxide Layers through Grubbs and Piers Catalyst-Functionalized Graphite Oxides / 167
7.1 Covalent and Non-Covalent Functionalization of Graphene Oxide Layers with Grubbs and Piers Catalysts / 167
7.2 Grafting Reactions of Polyisoprene to Graphene Oxide Layers / 173
References / 178
Section IV Experimental Part / 181
Chapter 8 Materials and Preparation Procedures / 183
8.1 Materials / 183
8.2 Preparation of Organoclays / 185
8.3 Extraction of Organoclay with Ethyl Acetate / 185
8.4 Clay Exfoliation by Supercritical CO$_2$ / 186
8.5 Preparation of sPS/Clay Gels and Aerogels / 186
8.6 Preparation of GO with Higher Content of Oxygenated Groups / 187
8.7 Preparation of GO with Lower Content of Oxygenated Groups / 188
8.8 Preparation of GOICs / 188
8.9 Preparation of GO and GOIC films / 189
8.10 Preparation of Chemically Reduced Graphite Oxide / 189
8.11 Graphite Oxide Exfoliation by Ball-Milling / 190
8.12 Solvo-thermal Reduction of Graphite Oxide / 190
8.13 Preparation of sPS/rGO Gels and Aerogels / 190
8.14 Preparation Organoclays in Rubber Medium / 191
8.15 Preparation of Rubber/Organoclay Nanocomposites by Melt Blending / 191

8.16 Preparation Rubber/Graphite Oxide Intercalation Compound Nanocomposites by Melt Blending / 192
8.17 Crosslinking of Rubber Nanocomposites / 193
8.18 Macromolecular Cross-Metathesis of High-*cis* Polybutadiene and Polyisoprene / 193
8.19 Metathetic Degradations of Polybutadiene and Polyisoprene and their Mixtures / 194
8.20 Covalent Functionalization of Graphene Oxide Layers with Grubbs Catalyst / 195
8.21 Non-Covalent Functionalization of Graphene Oxide Layers with Piers Catalyst / 196
8.22 Grafting of Polyisoprene to Grubbs and Piers Catalyst-Functionalized Graphene Oxides / 197
References / 197

Chapter 9 Characterization Techniques / 199

9.1 Wide Angle X-ray Diffraction / 199
9.2 Fourier Trasform Infrared Spectroscopy /201
9.3 Differential Scanning Calorimetry /202
9.4 Thermogravimetric Analysis / 202
9.5 Elemental Analysis / 202
9.6 BET Surface Area Measurements / 202
9.7 Scanning Electron Microscopy / 203
9.8 Trasmission Electron Microscopy / 203
9.9 Back Titration of Graphite Oxides / 203
9.10 Gel Permeation Chromatography / 203
9.11 NMR Spectroscopy / 204
9.12 Raman Spectroscopy / 204
9.13 Dynamic-Mechanical Analysis / 204
9.14 Tensile Tests / 205
9.15 Strain Sweep Tests / 205
9.16 Crosslinking Tests / 206
References / 206

Conclusions / 207
Acknowledgements / 209

Introduction

Tires are, by definition, composite artefacts in both structure and composition. A vehicle tire generally can contain different types of synthetic and natural rubbers, different types of fillers, steel cord, polyester, nylon, steel bead wire and various kinds of chemicals, waxes, oils and pigments.

Tire technology has always been based on nanostructured fillers. Carbon black and silica, in fact, are the most used reinforcing fillers for tires and have their internal structure in the nanoscale, so tires are primary nanocomposites.

Research and development of new nanofillers, able to produce an extended interface with the rubber matrix, play a role of increasing importance for tire industry, particularly on the commercial scale. Nanotechnology opens a wide range of product opportunities, in particular, allows not only to improve mechanical and barrier properties, but also to produce lighter and more durable tires.

Among nanofillers, clays were first used, in the 90's, for the preparation of polymer nanocomposites and are, still nowadays, the most applied ones in the rubber field, in spite of the large interest for carbon nanotubes and of the increasing number of studies on graphene and on nanofillers made by few layers of graphene, also for rubber composites.

Section I shows the preparation of tailor made layered nanofillers at the solid state, based on clays or graphitic materials, with different interlayer distance and different degrees of crystalline order in the direction parallel and perpendicular to the structural layers and in the interlayer space. In particular, the interaction of layered hosts with long-chain amphiphilic guests able to intercalate in the interlayer space, in presence or in absence of polar molecules, is investigated. Methods for the exfoliation of nanofillers are successfully implemented at the solid state and the conservation of the filler exfoliation state in polymeric aerogels is discussed.

Section II deals with the effect of organoclays and graphite oxide intercalation compounds in nanocomposites of 1,4-*cis*-polyisoprene, trying to attempt a correlation between the nanocomposite properties and the nanofiller structure.

Section III was completely devoted to metathesis of polydienes as a powerful technology to obtain not only novel polymer-polymer materials, but also hybrid polymer-filler nanocomposites with suitably functionalized fillers. Furthermore, degradation reactions of rubbers are also investigated by using metathesis catalysts.

Finally, **Section IV** collects details on materials, all experimental procedures and characterization techniques used in this work.

Section I

Layered Nanofillers for Rubber Nanocomposites

The text in this section is reproduced in part with permission from the following published works:

- V. Cipolletti, M. Galimberti, M. Mauro, G. Guerra. *Appl. Clay Sci.* **2014**, *87,* 179–188.
- S. Longo, M. Mauro, C. Daniel, M. Galimberti, G. Guerra. *Front. Chem.* **2013**, *1,* 1–9.
- M. Mauro, M. Maggio, V. Cipolletti, M. Galimberti, P. Longo, G. Guerra. *Carbon* **2013**, *61,* 395–403.
- M. Mauro, V. Cipolletti, M. Galimberti, P. Longo, G. Guerra. *J. Phys. Chem. C* **2012**, *116,* 24809–24813.
- M. R. Acocella, M. Mauro, L. Falivene, L. Cavallo, G. Guerra. *ACS Catalysis* **2014**, *4,* 492–496.

Chapter I

Cationic Clays and Organoclays

I.1 Clays and Their Structures

According to the definition of the Joint Nomenclature Committees (JNCs) of the Association Internationale pour l'Etude des Argiles (AIPEA) and the Clay Minerals Society (CMS), a clay is "a naturally occurring material composed primarily of fine-grained minerals, which is generally plastic at appropriate water contents and will harden when dried or fired".[1]

Clays are layered materials with strong iono-covalent bonds inside each layer and weaker forces along the stacking direction. The volume included between two successive layers is called the "interlayer space".[2]

Clays are classified in three different categories according to the electrical charge of the layer (see **Scheme I.1**). Pyrophyllite, talc, and kaolinite are composed by neutral layers held together by van der Waals interactions and/or hydrogen bonds. Cationic clays, as phyllosilicates, are composed by negatively charged layers compensated exactly by an equal amount of positive charges, provided by cations located in the interlayer space (compensating cations). Anionic clays are composed by positively charged layers with compensating anions in the interlayer space. The most common natural mineral in this group is hydrotalcite (HT), but this belongs to a broader family of "HT-like" materials called layered double hydroxides or LDH.

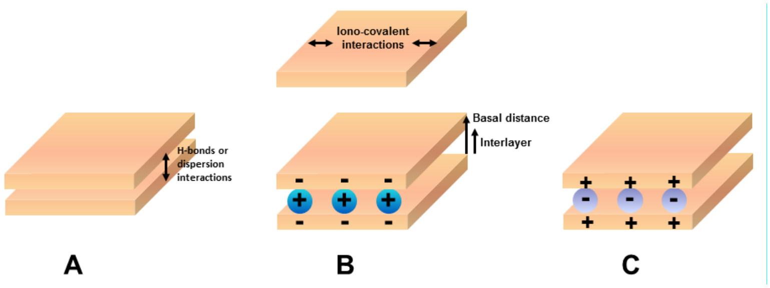

Scheme I.1. The basic structure of a clay mineral at the nanometric scale: (A) neutral layers, (B) negatively charged layers with compensating cations (cationic clays) and (C) positively charged layers with compensating anions (anionic clays), after ref. 2.

In this chapter we focused on phyllosilicates, such as montmorillonite (MMT), belonging to the group of smectites, composed by two tetrahedral (T) sheets linked to both sides to a central octahedral (O) sheet (2:1 or TOT type clay layers). Weak forces held together the layers and alkaline and alkaline-earth cations, as well as water molecules are located in the interlayer space. Tetrahedral sheets are constituted of corner sharing [XO_4] units, where X is a small cation, which may be either Si^{4+}or Al^{3+}; oxide ions (formally O^{2-}) occupy the corners. Octahedral sheets consist of edge-sharing [$MO_4(OH)_2$] units, where M can be either a trivalent (such as Al^{3+}), a divalent (such as Mg^{2+}).[3]

The general formula of MMT is $[^{IV}(Si_4)\ ^{VI}(Al_{2-y}Mg_y)\ O_{10}\ (OH_2)]^{y-}\ (M^{n+})_{y/n} \cdot mH_2O$, M^{n+} may be nearly any alkaline and alkaline-earth cation and y is the divalent cation substitution degree. The X-ray diffraction pattern of sodium MMT (Dellite® HPS from Laviosa Chimica Mineraria S.p.A.) is shown in **Fig. I.1**, while a plausible structure of the MMT is reported in **Fig. I.2**.

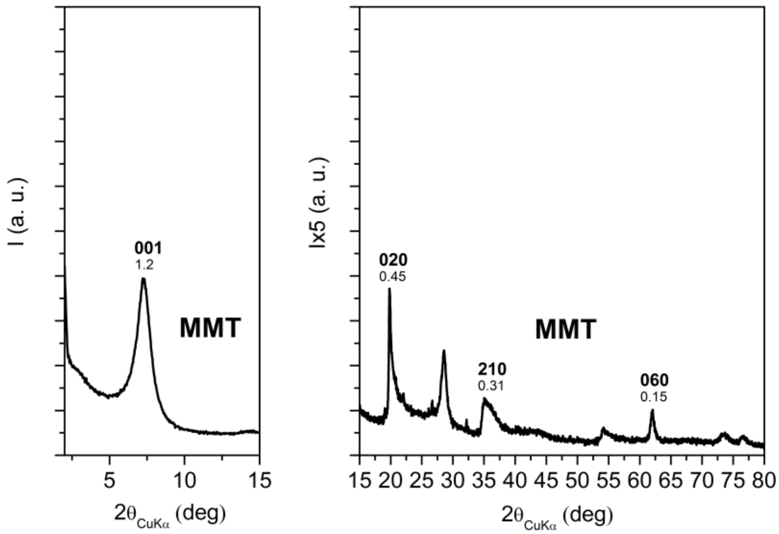

Fig. 1.1. X-ray diffraction patterns (Cu Kα) of the commercially available sodium MMT, Dellite® HPS, from Laviosa Chimica Mineraria S.p.A.

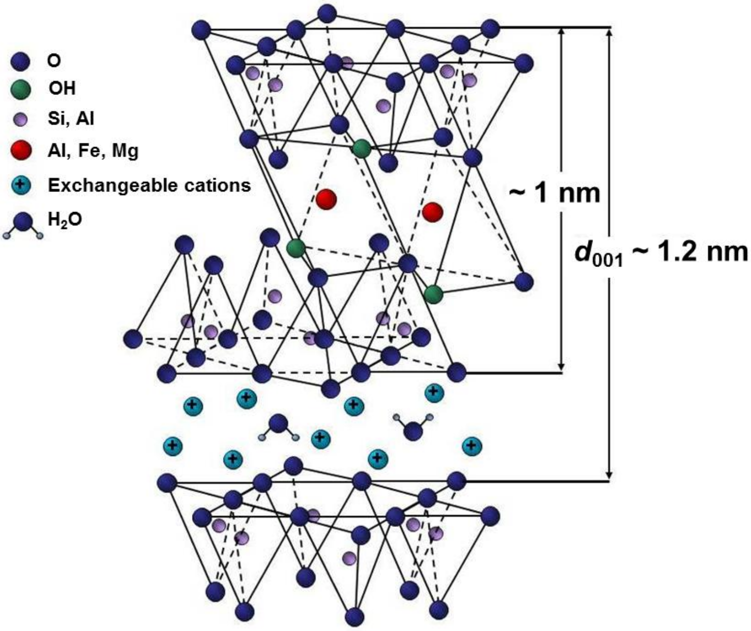

Fig. 1.2. Structure of MMT.

The pattern of the sodium MMT in **Fig. 1.1** presents a broad 001 reflection, corresponding to an interlayer distance of 1.2 nm, with a correlation length of 5 nm. Narrow 020 and 060 reflections, corresponding to a long-range order in the clay layers (correlation length perpendicular to the 020 planes higher than 18 nm) are also observed.[4,5]

1.1.1 Multiscale Organization of Clays

Clays are characterized by structural features particularly suitable to substantially improve rubber properties, namely mechanical and barrier properties: a high average ratio of the width to the thickness of the particles, the so-called aspect ratio, the availability of a space between two opposite layers, suitable to accommodate molecules, the tunability of properties such as hydrophilicity and hydrophobicity. In fact, clays are characterized by a multiscale organization.[3]

At the upper level (macroscopic) of said organization, clay particles of micrometric size form millimetric-size aggregates. Accordingly we may distinguish between interlayer space, interparticle space, and interaggregate space (pores) (see **Scheme 1.2**).

The arrangement of the particles or aggregates leads to different morphologies, such as platelets or "tactoids", tubules, laths, and fibres. Phyllosilicates are composed by platelets and are porous, containing pores of varied size and shape.[3]

Clay particles can interact in different ways, such as face-to-face, edge-to-edge, or edge-to-face. Extended edge-to-face aggregates are sometimes called "house-of-cards" structures (see **Scheme 1.2**). The type of dispersion of clay particles in a polymer matrix is a very important feature of polymer nanocomposite.[2]

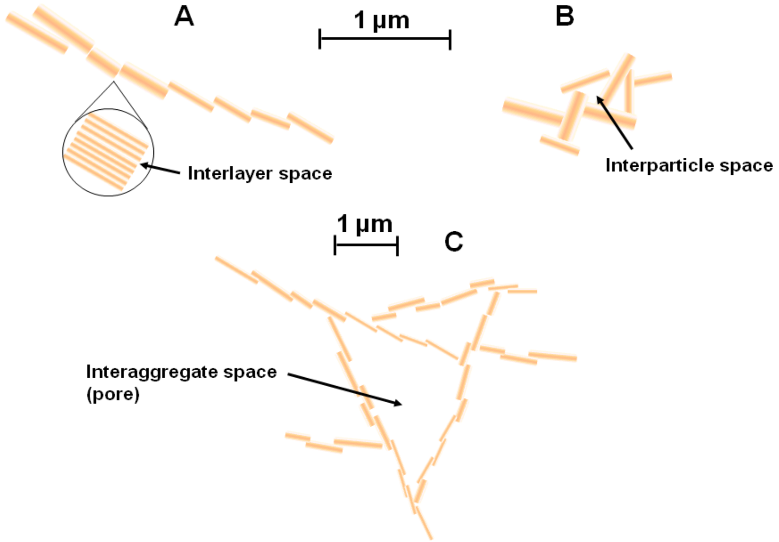

Scheme I.2. Top: aggregation of clay particles at the micrometer scale, mostly edge-to-edge (A) the inset shows the stacking of elementary layers within a particle; and mostly edge-to-face (B). Bottom: higher level organization of aggregates (C), after ref. 2.

At the lowest (molecular) level, the individual particles shown in **Scheme I.2** are composed of the stacking of elementary layers, alternating with interlayer spaces containing the compensating cations, and whatever other molecules may happen to be intercalated (see next paragraph). The stacking exhibits crystallographic periodicity along the *c* axis, even though successive layers may be oriented differently according to the *a* and *b* directions. A single clay layer is characterized by lateral dimensions from 100 to 1000 nm and by a thickness of about 1 nm.

The term exfoliation is used to designate the separation between the planar faces of two adjacent layers. The layers may eventually become completely independent from one another and isotropically dispersed in the solvent or polymer matrix (see **Scheme I.3**).

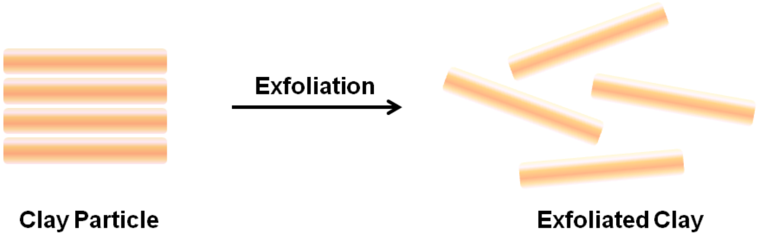

Scheme 1.3. Schematic representation of the exfoliation of a clay particle.

1.2 Organoclays

Most of the technological applications of clays are related to their ability to intercalate organic cations by exchange reactions with the cations in their interlayer spaces. Here, we define the cation exchange capacity (CEC) of a clay as the total amount of cations available for exchange at a given pH, which is commonly expressed as milliequivalent/100 g of calcined clay.

The organically modified clays of organoclays (OCs) are used, since long time, for important applications,[6,7] such as waste-water treatment and waste disposal,[8–11] as rheological control agents,[12] in the environmental field,[13,14] for cosmetics [15] and for drug delivery.[16–18]

In the last decades, modified clay minerals, based in particular on MMT, have played a key role for the development of clay polymer nanocomposites.[19–22]

Clay minerals have a hydrophilic nature and, to be evenly distributed and dispersed in a hydrocarbon polymer matrix, they need a compatibilizer [6]: organophilic ammonium cations have been mostly used as MMT modifier. OCs are prepared with the help of liquids, such as water and alcohols,[23] but also at the solid state.[7] Over the last years, an alternative route for the synthesis of OCs to be used in polymer-clay nanocomposites was developed [24,25]: the reaction of the pristine clay mineral with the ammonium cation was performed *in situ* in the polymer matrix, adopted as the reaction medium.

The *neat* synthesis of OCs appears of great interest for the development of a large variety of polymer-clay nanocomposites, as the absence of solvents makes this process environmentally friendly and suitable for industrialization, with a favourable impact on economic aspects. As anticipated above, OCs preparation at the solid state is well known in clay minerals field. Ogawa *et al.* first reported the intercalation in MMT of acrylamide, n-alkylamine and 2,2'-bipyridine [26,27] and of naphthalene and anthracene into alkyltrimethylammonium modified MMT.[28] Reactions with smectites at the solid state were then reported for octadecylamine,[29,30] also in the presence of stearic acid,[31] 2HTCl,[32] alcohols, aldehydes, n-alkyl pyrrolidones,[33] aniline salts,[34] polycarbazole [35] and distearyl dimethyl ammonium chloride.[36]

In this work, OCs were prepared at the solid state, in the absence of any solvent, according to the experimental procedure described in paragraph 8.2 in Section IV. The preparation of the OCs was performed by the group of Prof. Maurizio Galimberti at the Polytechnic of Milan.

A commercially available OC with roughly 40 %wt. of 2HT, such as Dellite® 67G from Laviosa Chimica Mineraria S.p.A, was first characterized, as reference sample. The X-ray diffraction (Cu Kα) pattern in the 2θ range 2-80° of Dellite® 67G is reported in **Fig. I.3**.

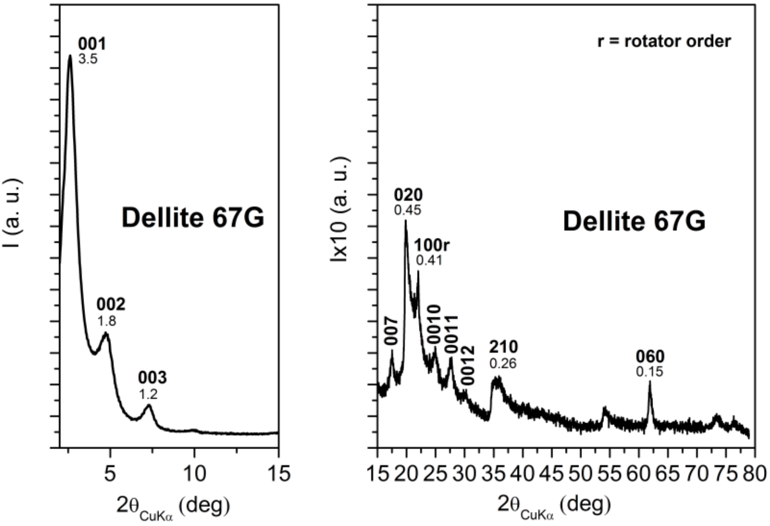

Fig. 1.3. X-ray diffraction patterns (Cu Kα) of commercially available Dellite® 67G from Laviosa Chimica Mineraria S.p.A. The symbol **r** indicates the reflection relative to the rotator order.

Besides many 00ℓ reflections (up to $\ell = 12$) that indicate a high degree of order perpendicular to the clay layers and an interlayer spacing of 3.5 nm, the pattern shows well defined weak reflections, corresponding to the typical 020, 210 and 060 in-plane MMT periodicities.

It is worth adding that a well defined narrow reflection is also present at $2\theta = 21.7°$, corresponding to $d = 0.41$ nm, which suggests the occurrence of a hydrocarbon rotator order,[37–42] i.e. of an hexagonal order of the intercalated long hydrocarbon chains. Analogous hexagonal rotator order in the packing of long hydrocarbon tails has been observed for intercalates of anionic clays [43] and of graphite oxide [44] (see paragraph 2.5).

The thickness of the clay layer (≈ 1 nm) and the length of the alkylammoniums [45] (≈ 5 nm) indicate that the tilting angle of the hydrocarbon chains with respect to the normal to the clay layers is not far from $\varphi = 60°$. Hence, the X-ray diffraction pattern of

Dellite® 67G in **Fig. 1.3** indicates the presence of an intercalate structure, whose schematic projections, parallel and perpendicular to the clay layers, are shown in **Fig. 1.4A** and **Fig. 1.4B**, respectively.

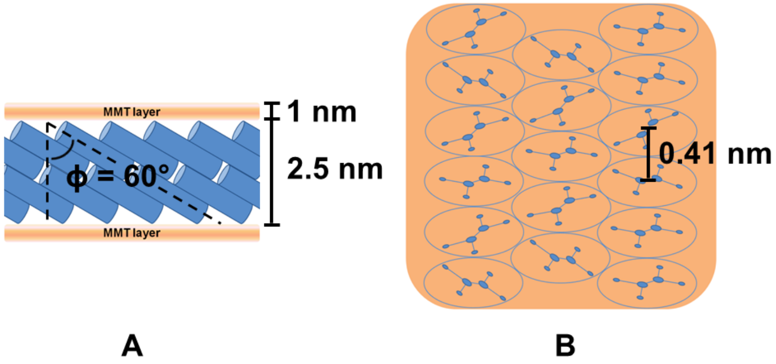

Fig. 1.4. Schematic projections parallel (A) and perpendicular (B) to the clay layers of the starting OC intercalate structure (Dellite® 67G). The hydrocarbon tails of the ammonium cations are represented as cylinders in the lateral view (A) and as ellipses in the top view (B). The distance between the axes of adjacent cylinders (0.41 nm) is shown in B while the definition of the alkyl chains tilt angle φ is shown in A.

1.2.1 Preparation of Organoclays at the Solid State

For the preparation of OCs at the solid state, pristine MMT (Dellite® HPS from Laviosa Chimica Mineraria S.p.A.) and dimethyl ditallow ammonium chloride (2HTCl) (the molecular structure of 2HT is reported in **Fig. 1.5**) were used as the clay mineral and as the ammonium salt, respectively. The molar amount of the ammonium salt was equal to the nominal CEC of pristine MMT (128 mmol/ 100g).

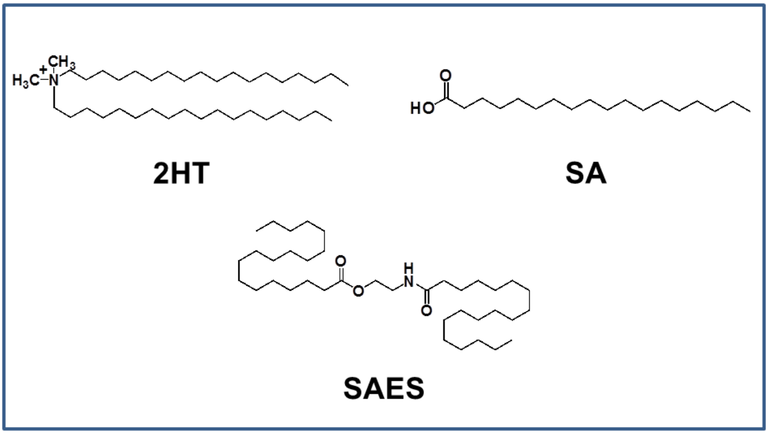

Fig. 1.5. Molecular structures of ionic and polar compounds intercalated with MMT: dimethyl ditallow ammonium (2HT), stearic acid (SA) and 2-stearamidoethyl stearate (SAES).

The *neat* synthesis is composed of two steps, characterized by the use of two different forms of energy for promoting the reaction between MMT and 2HTCl. In the first step, mechanical energy is given to the reaction mixture, by ball milling it at 380 rpm for 1 hour. In the second step, the mixture is kept (for about 1 hour) at a temperature well above the melting point of the ammonium salt. OC samples were also prepared, through the *neat* synthesis, by adding to the reaction mixture, before the ball milling step, either stearic acid (SA) and 2-stearamidoethyl stearate (SAES) (see the molecular structures in **Fig. 1.5**), used in a molar amount equal to the molar amount of the ammonium salt. As the OC samples were not washed with any solvent after their preparation, they were characterized by the presence of NaCl, arising from the cation exchange reaction.

1.2.2 Characterization of Organoclays

OC samples were first characterized through thermogravimetric analysis reported in **Fig. 1.6**. The organic contents of MMT/2HT, MMT/2HT/SA and MMT/2HT/SAES were evaluated as 44 %wt., 54 %wt. and 61 %wt., respectively.

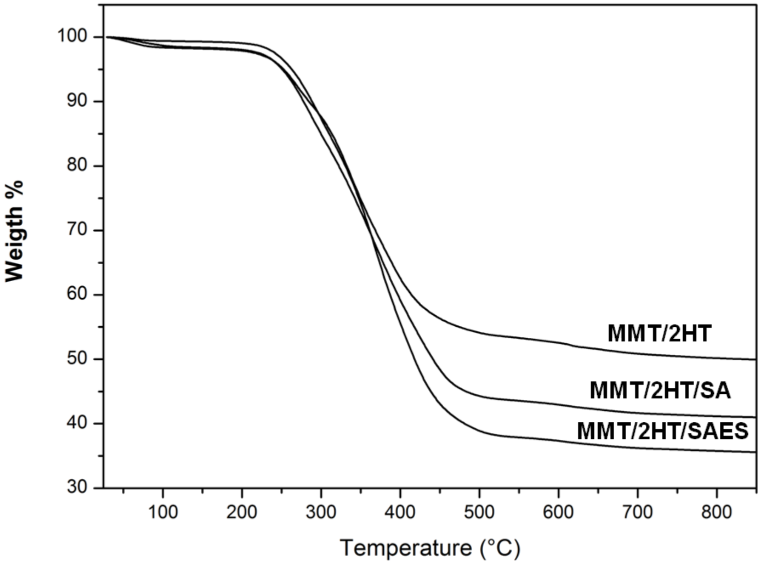

Fig. 1.6. Thermogravimetric analysis in N_2 of: MMT/2HT, MMT/2HT/SA and MMT/2HT/SAES.

The X-ray diffraction pattern of the OC, prepared by mixing MMT and 2HT, in **Fig. 1.7** shows four 00ℓ reflections and a basal spacing of 4.0 nm with a correlation length increased up to 17 nm.

More ordered OCs were obtained by adding a second polar guest, such as SA or SAED to the pristine MMT and 2HT. Both patterns of MMT/2HT/SA and MMT/2HT/SAES show al least six 00ℓ reflections with an increased correlation length (D = 31 nm) and with a largely increased spacing (d = 6.0 nm).

The X-ray diffraction pattern of the OC after extraction of MMT/2HT in a Kumagawa extractor with a good solvent such as ethyl acetate for 12 h is shown in the upper part of **Fig. 1.7**. The same results were obtained for the extraction of MMT/2HT/SA and MMT/2HT/SAES in the same conditions. The basal spacing decreases from the initial 4 nm or 6 nm value to a value of 2.5 nm and the correlation length also decreases down to 8 nm.

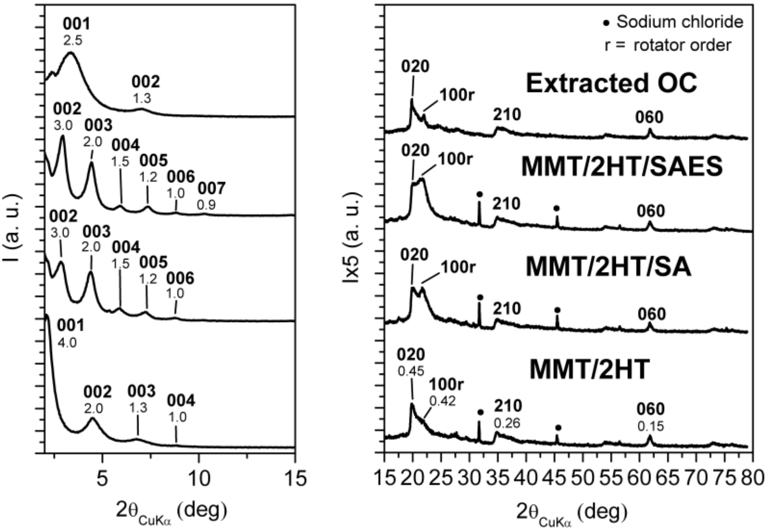

Fig. I.7. X-ray diffraction patterns (Cu Kα) of MMT/2HT, MMT/2HT/SA and MMT/2HT/SAES. The pattern of the OC obtained by extraction of MMT/2HT with ethyl acetate is also reported in the upper part. The symbol **r** indicates the reflection relative to the rotator order.

An analogous structure was obtained by extraction of Dellite® 67G with ethyl acetate from 2 to 6 hours (see **Fig. I.8**). The interlayer distance decreased from the initial 3.5 nm value to a plateau value of 2.5 nm. A lower value was not observed even by protracting the extraction. The organic content detected in the extracted OC samples with 2.5 nm as the d_{001} interlayer distance, as evaluated from TGA measurements, was about 36 %wt. The value of 2.5 nm as interlayer distance seems thus to correspond to a minimum of energy.

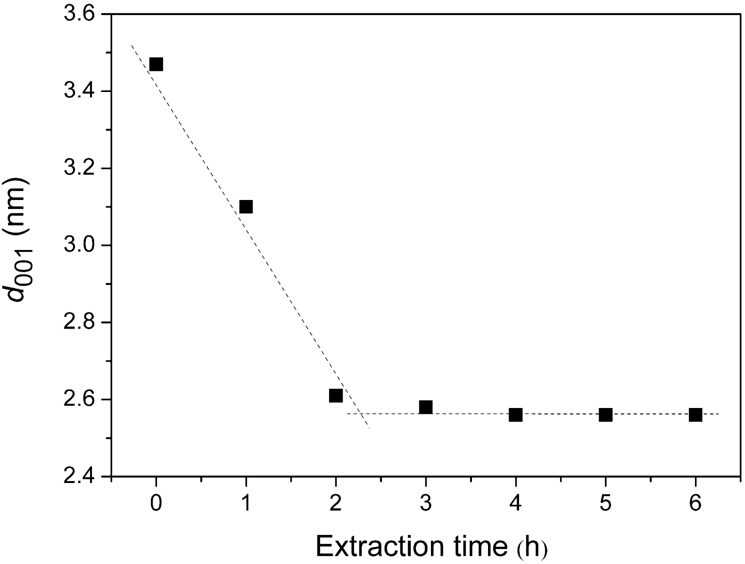

Fig. 1.8. d_{001} interlayer distance as a function of the extraction time for a sample of commercially available organoclay (Dellite® 67G).

The patterns of **Fig. 1.7** also presents an intense reflection at $d = 0.42$ nm, i.e. the distance between long hydrocarbon chains in their rotator order,[37–42] already observed for Dellite® 67G. In the patterns of MMT/2HT/SA and MMT/2HT/SAES the reflection attributed to the rotator order is more intense and narrower than in the pattern of MMT/2HT, as a consequence of addition of a second polar guest.

The influence of SA on the formation of MMT/2HT/SA organoclay, with 6.0 nm as interlayer distance (see **Fig. 1.7**), was further explored by Fourier transform infrared (FTIR) measurements.[25] The co-intercalation of SA and of 2HT in the MMT/2HT/SA organoclay is clearly confirmed by analysis of the carbonyl region of the FTIR spectra in **Fig. 1.9**. In particular, the carbonyl peak of SA, for the molecules in the crystalline solid is centered at 1704 cm^{-1}. On the other hand, the carbonyl peak of SA is largely shifted (up to nearly 1725 cm^{-1}) after mixing with the

2HT ammonium salt (at 100 °C, weight ratio close to 1:1) or after mixing with 2HT and MMT in the solid state (nearly 1726 cm^{-1}). The observed shift to higher frequencies of the acid carbonyl stretching mode indicates weaker hydrogen bonding in the mixed systems, with respect to the pure acid.[**46**] Analogous results were obtained for the carbonyl stretching of the MMT/2HT/SAES organoclay with respect to SAES amide.

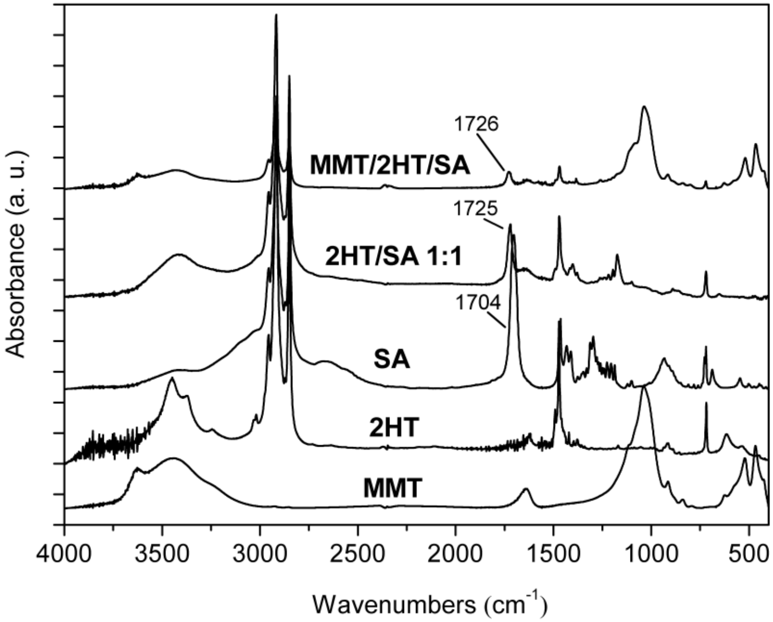

Fig. 1.9. Infrared spectra of: MMT, 2HT, SA, solid mixture of 2HT and SA (1:1) and MMT/2HT/SA.

1.2.3 Structural Reversibility of Organoclays with Temperature

DSC heating scans of MMT/2HT, MMT/2HT/SA, MMT/2HT/SAES samples and of the OC obtained by extraction of MMT/2HT with ethyl acetate are shown in **Figs 1.10A–D**. The data on transition temperature and enthalpy corresponding to the loss of rotator order of the hydrocarbon tails, as detected in the first heating scan, are also shown. As expected on the basis of X-ray diffraction findings, calorimetric results reveal that the transition temperatures increase from MMT/2HT to MMT/2HT/SA and, in particular, to MMT/2HT/SAES. These endothermic phenomena detected by heating OC samples have been also described as 2D melting of ammonium cations, that can not give rise to the 3D melting, as they are linked to the inorganic layer.[45]

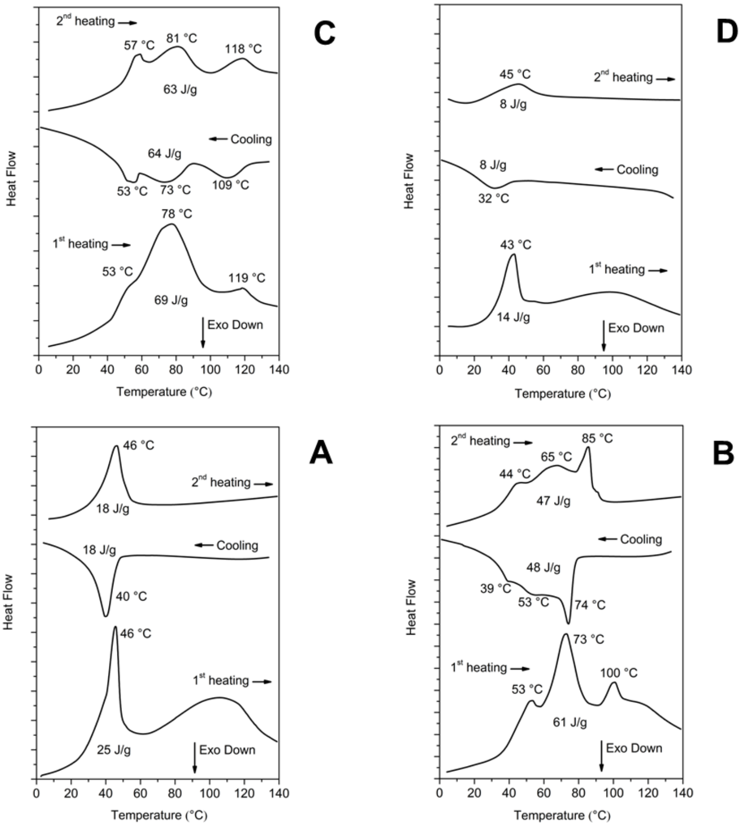

Fig. 1.10. DSC heating scans of: (A) MMT/2HT, (B) MMT/2HT/SA, (C) MMT/2HT/SAES and (D) OC obtained by extraction of MMT/2HT with ethyl acetate.

Moving from DSC findings, X-ray diffraction analysis was repeated on MMT/2HT and MMT/2HT/SA samples, exploring a temperature range from 20 °C to 85 °C. For both OC, diffraction patterns were taken every 5 °C and d_{001} basal spacing was determined, by first heating and then cooling the samples. In **Fig. I.11**, d_{001} values are plotted against the temperature at which the pattern was taken. The lower part of **Fig. I.11** refers to MMT/2HT sample, whose heating causes a fully reversible increase of the interlayer distance, of nearly 0.3 nm. The upper part of **Fig. I.11** refers to MMT/2HT/SA, whose heating leads to a reversible decrease of the interlayer distance of nearly 1.0 nm. In this case, however, a substantial hysteresis in the interlayer spacing recovery is observed.

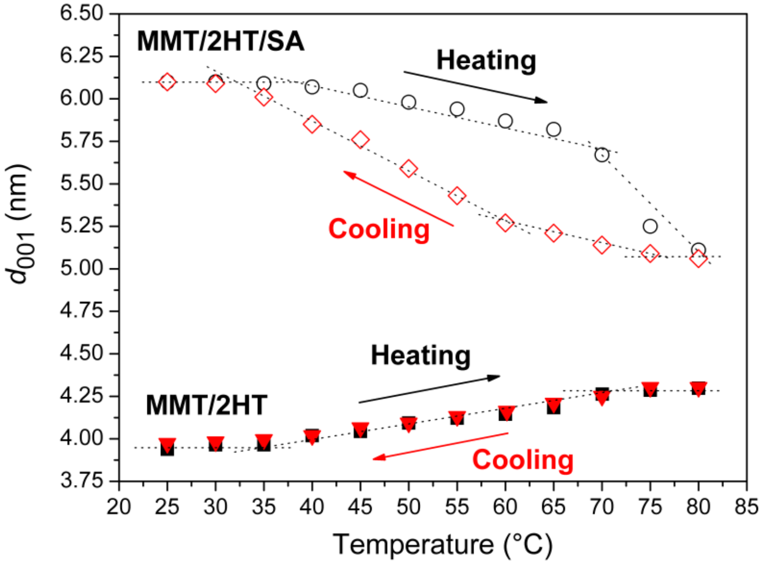

Fig. I.11. d_{001} values determined in the temperature range 25°C – 80°C, every 5 °C, for MMT/2HT and MMT/2HT/SA.

The hexagonal rotator order for the packing of paraffinic chains belonging to the ammonium cation and to the guest (either SA or SAES) was further investigated by performing successive WAXD analysis of the MT/2HT/SA organoclay: at room temperature (RT), then at 80 °C and, finally, at RT, upon cooling the OC.

Fig. 1.12 shows the X-ray diffraction patterns taken at the mentioned temperatures. It can be clearly seen that the hexagonal rotator order is present at RT, is then lost at 80 °C and is again visible, when the OC is cooled to RT.

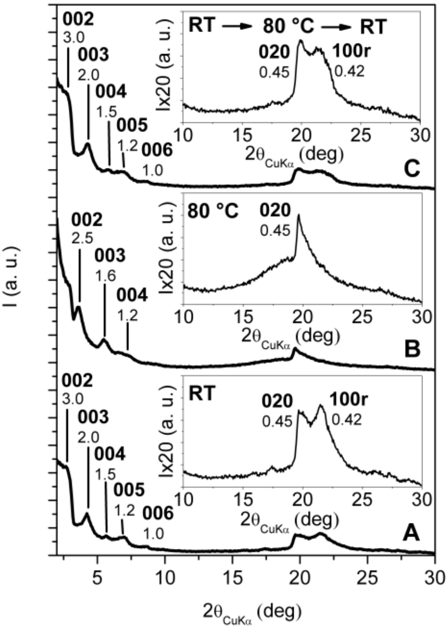

Fig. 1.12. X-ray diffraction patterns (Cu Kα) of MMT/2HT/SA sample prepared through the neat synthesis. Patterns subsequently taken at: (A) RT, (B) 80 °C and at (C) RT upon cooling the OC.

1.2.4 Structures of Organoclays

The overall analysis of data arising from the characterization of OCs reveals that three main types of organically modified MMT are obtained from the *neat* synthesis of MMT with 2HTCl and, optionally, either SA or SAES. Said three main types of organically modified MMT are characterized by a typical d_{001} interlayer distance: 2.5 nm, 4.0 nm, 6.0 nm. The d_{001} clay interlayer distance depends on the placement of the paraffinic chains of the amphiphile modifier of the clay layer, and, more in particular, is a function of the tilting angle of said chains. The structures shown in **Fig. I.13** could be preliminary proposed to justify the experimental findings. Bilayer tilted placements, with tilting angles of φ = 72° and of 54° with respect to the normal to the clay layers, are proposed to justify the 2.5 nm and 4.0 nm interlayer distances, respectively. These distances depend on the amount of the compensating cation present in the interlayer space. A perpendicular placement of paraffinic chains accounts for the 6.0 nm distance. These d_{001} values can be considered to correspond to minima of energy for the organically modified MMT.

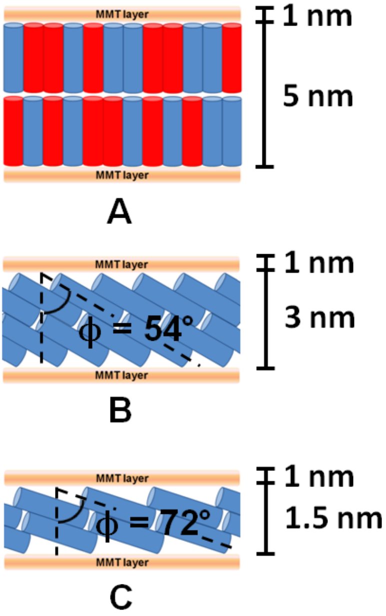

Fig. I.13. Plausible structures for OCs with: (A) 2HT + SA or SAES, (B) 2HT, (C) 2HT, after extraction with ethyl acetate. The cylinders indicate hydrocarbon tails of the ammonium cation (blue) or of the additional polar guest (red). The definition of the alkyl chains tilt angle φ is shown in B and C.

The structures proposed above can be also rationalized taking into account that the orientation of the alkyl chains is a function of the cross-sectional area of the paraffinic chains of the amphiphile (A_C), defined as the cross-section perpendicular to the outstretched hydrocarbon chains in relation to the available clay surface per amphiphile (A_S).[47]

The increase of the cross-sectional area of the paraffinic chains of the amphiphile generally leads to a reduction of the tilting angle and, when A_C is very close to A_S, the paraffinic chains become perpendicular to the clay layer surfaces.[47]

In the case of the OC with stearic acid as the guest, the interaction of the acid group of stearic acid with the ammonium group of the amphiphile exhibiting two long alkyl chains (2HT), leads to three parallel alkyl chains, which locally produce large cross-sectional areas, and thus in turn leading to their perpendicular orientation with respect to the clay layers.

Ordered OCs structures were prepared by the *neat* synthesis of MMT with 2HTCl, adding optionally, either SA or SAES. The interaction of rubber with OCs prepared both in the solid state and by using the rubber matrix as reaction medium will be discussed in chapter 3 in Section II. In the next paragraph the exfoliation of intercalated clays by supercritical carbon dioxide and the conservation of their exfoliation state in clay rich polymer/clay aerogels will be discussed.

I.3 Clay Exfoliation and Polymer/Clay Aerogels by Supercritical Carbon Dioxide

Intercalated clays are interesting intermediate materials that allow to prepare not only ordered intercalate structures, but also disordered structures. Mechanical treatments of intercalated clays are reported as effective routes to produce exfoliated clays.[48,49]

Many reports show that different processing techniques based on supercritical carbon dioxide ($scCO_2$) constitute effective ways to increase dispersion and exfoliation in polymer/clay nanocomposites. However, X-ray characterization of most samples show the presence of basal 00ℓ reflections, clearly indicating that treatments with $scCO_2$ are generally unsuitable to induce complete organoclay exfoliation.[50–56]

Only some reports, from the Kannan's group, show that a complete disappearance of the 00ℓ reflections (and hence a complete exfoliation) can be achieved by $scCO_2$ treatments on pure organoclays, where alkali counterions have been exchanged with long-chain alkylammoniums.[57,58] However, as a consequence of preparation of polymer nanocomposites, the 00ℓ reflections reappear with peak height and location essentially independent of the processing conditions.[58]

$scCO_2$ treatments are also effective to prepare monolithic aerogels, by drying of wet gels. Aerogels constitute a unique class of materials, characterized by a highly porous network being attractive for many applications such as thermal and acoustic insulation, capacitors or catalysis.[59–63]

In recent years, the $scCO_2$ extraction of gels of suitable thermoplastic polymers, like syndiotactic polystyrene (sPS) [64–66] has allowed the preparation of a special class of monolithic aerogels,[67–70] that present, beside disordered amorphous micropores (typical of all aerogels), identical nanopores of *nanoporous-crystalline* phases (see **Fig. 1.14**).

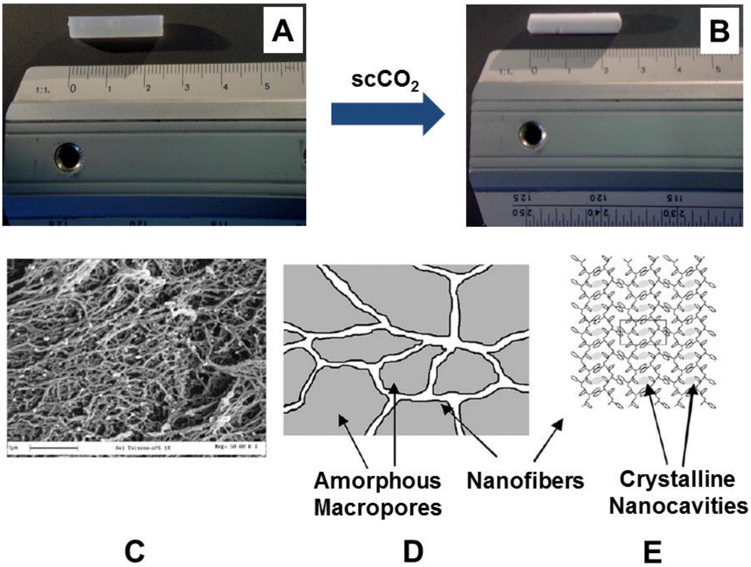

Fig. 1.14. (A) Gel sPS/toluene 1/99, (B) δ-form of sPS aerogel with a porosity of 99%, containing 1 %wt. of polymer, (C) Scanning electron microscopy of the sPS aerogel, (D) Schematic presentation of the nanofibrils and of the amorphous porosity. In (E), the grey regions indicate the presence of all identical crystalline nanocavities, after ref. 68.

A first aim of the present discussion is a deeper investigation of the scCO$_2$ induced organoclay exfoliation, by a more complete X-ray diffraction characterization of organoclays before and after scCO$_2$ treatments. The second aim of the discussion is the preparation of composite aerogels containing large amounts of exfoliated organoclay as well as a nanoporous-crystalline polymer phase. The basic idea is that aerogel preparation processes, also based on scCO$_2$ extraction, could help to maintain the clay exfoliation, which is generally lost in the nanocomposite processing. Monolithic sPS/exfoliated clay aerogels not only could be helpful to an easier handling of exfoliated clays, removing the risks connected with inhalable nanoparticles, but also, due to their thermoplastic nature, could be used as exfoliated clay "masterbatches" for composite processing, also for rubber compounds. The commercial Dellite® 67G was selected as the starting OC. The preparation and the characterization of polymer/clay aerogels were performed in collaboration with Dr. Simona Longo of the Department of Chemistry and Biology of the University of Salerno.

1.3.1 Organoclay Exfoliation by Supercritical Carbon Dioxide

The X-ray diffraction patterns of Dellite® 67G of **Fig. 1.15A**, after short term and long term treatments by $scCO_2$ are shown in **Fig. 1.15B** and **1.15C**, respectively.

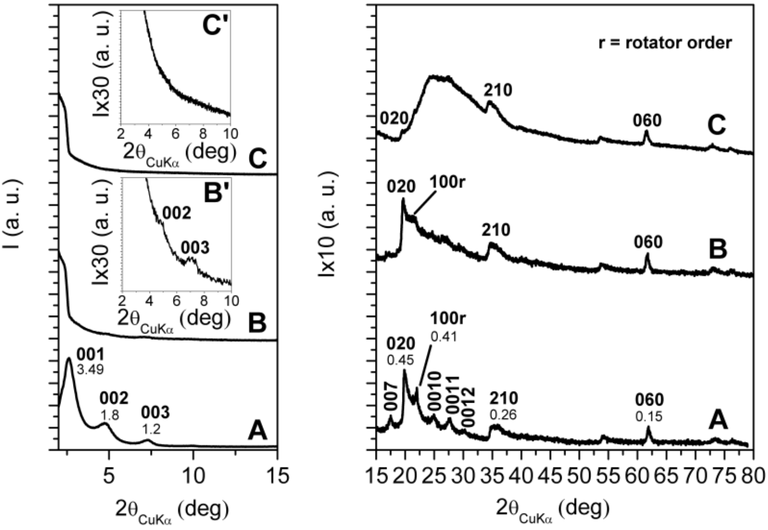

Fig. 1.15. X-ray diffraction (Cu Kα) patterns in the 2θ range 2-80° of Dellite® 67G before (A) and after 16h (B) and 32h (C) $scCO_2$ treatments. The inset in B and C enlarges the 2θ range 2-10°.The Miller index 110r indicate the reflection relative to the rotator order of the long hydrocarbon chains within the interlayer space.

For the intermediate pattern of **Fig. 1.15B**, the intensities of the 00ℓ peaks as well as of the rotator order peak (100r) are strongly reduced (see also the inset of **Fig. I.15B**). The in-plane 020, 210 and 060 peaks maintain their intensity and narrowness. This indicates that short term $scCO_2$ treatments lead to a nearly complete clay exfoliation with maintenance of the in-plane order. In agreement with previous results,[58] the X-ray diffraction pattern of the OC, after long-term $scCO_2$ treatments, does not show anymore the 00ℓ reflections (see also the inset of **Fig. I.15C**): clay exfoliation is achieved. It is worth adding that the in-plane 020, 210 and 060 reflections are still present, although become less intense than a broad amorphous halo that appears in the 2θ range 20°-30°. This amorphous halo can be attributed to a loss of order in the stacking of the clay layers, also associated with a complete loss of order in the packing of the hydrocarbon tails.

In summary, the described long-term $scCO_2$ treatments lead to exfoliation of the OC, and to a complete loss of long-range lateral order of the hydrocarbon tails of the cationic surfactant. The maintenance of hk0 reflections (mainly of the isolated 060 reflection), not yet reported in the literature, assures the maintenance of a long-range order in the clay layers. In this respect, it is worth adding that the half-height width of the 060 reflection, after exfoliation, remains equal to 0.45°, indicating a correlation length $D_{060} = 28$ nm.

Relevant additional information, relative to the as received and $scCO_2$-treated OC, can be obtained by DSC scans (see **Fig. I.16**). The scan of the as received OC (**Fig. I.16A**) presents a reversible transition nearly located at 47°C ($\Delta H_r \approx 24$ J/g) that corresponds to the loss of rotator order of the hydrocarbon tails of the cations intercalated in the interlayer space. The DSC scan of the $scCO_2$ treated OC does not present any thermal transition in the considered temperature range (**Fig. I.16B**) and hence indicates the loss of 3D order in the packing of the hydrocarbon tails of the ammonium surfactant, which is compatible with clay exfoliation.

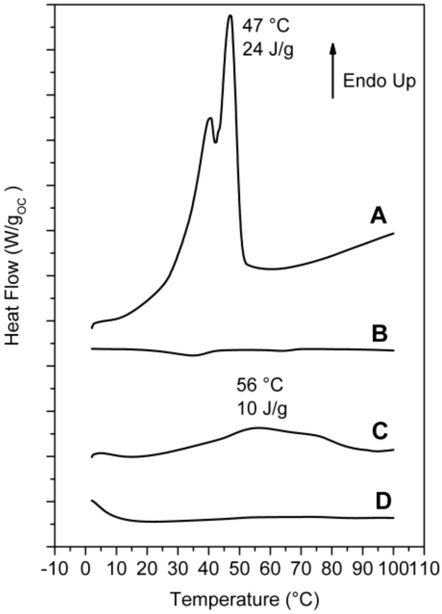

Fig. 1.16. DSC heating scans of: (A) as received intercalated OC (Dellite® 67G); (B) OC after treatment by scCO$_2$ (exfoliated); (C, D) aerogels with 90% of porosity, with 50/50 weight ratio of sPS/intercalated OC (C) and of sPS/exfoliated OC (D).

The overall information arising from X-ray diffraction and DSC characterization allows to conclude that the as received and scCO$_2$ treated OC can be described as intercalated and exfoliated OC, respectively.

1.3.2 Monolithic Nanoporous Polymeric Aerogels with Large Organoclay Content

Monolithic composite aerogels, filled with large fractions of intercalated and exfoliated OC, have been prepared by using an sPS matrix. This polymer choice is mainly due to the ability of sPS to produce monolithic aerogels in a very broad range of porosity (from

50% up to 99%).[**67,68**]

Aerogels with a porosity of nearly 90% were obtained by $scCO_2$ extraction of gels with a 1,2-dichloro benzene (DCB) content of 90 %wt. and with different sPS/OC weight ratios. For all aerogels with polymer/OC ratio equal or higher than 80/20, monolithic structures were obtained. Moreover, as usual for sPS based aerogels,[**67,68**] the size and shape of sPS/clay aerogels are essentially the same of the precursor gels. Aerogels with a 50/50 polymer/OC ratio are brittle and are generally obtained as powders.

X-ray diffraction (Cu Kα) patterns of sPS based aerogels, containing intercalated and exfoliated OC, are shown in **Fig. I.17** and **I.18**, respectively.

All patterns of **Fig. I.17** show the typical reflections of the nanoporous-crystalline δ form. In particular, the isolated intense 010 reflection is always clearly apparent and located at $2\theta \approx 8.4°$. The 00ℓ reflections of the OC are not detected for the aerogels with low clay content (4 and 8 %wt.) while for higher clay contents (20 and 50 %wt.) a narrow and intense 001 reflection is present, while the 002 and 003 reflections of the starting clay have disappeared. Moreover, the 001 reflection is markedly shifted with respect to its original position (from $2\theta = 2.6°$ up to $2\theta = 3.8°$), indicating a decrease of the interlayer spacing from $d = 3.5$ nm down to $d = 2.3$ nm.

The results of **Figs I.17A-C** suggest that the aerogel preparation procedure involving $scCO_2$ extraction, for low OC content, could lead to clay exfoliation, as already observed for $scCO_2$ treatment of the neat OC in **Fig. I.15**. **Figs I.17D,E** show that, for high OC content in the aerogels, the used procedure is not suitable to generate OC exfoliation but, on the contrary, a reduction of the interlayer spacing is observed. An analogous phenomenon of reduction of interlayer spacing has been observed for OC extraction with ethyl acetate, as already described in paragraph I.2. The observed reduction of basal spacing can be attributed to the extraction of excess cationic surfactant, not being ionically bonded to the negatively charged clay layers, but being simply included in the interlayer space by non-bonded interactions and contributing to the crystalline order of the hydrocarbon tails.

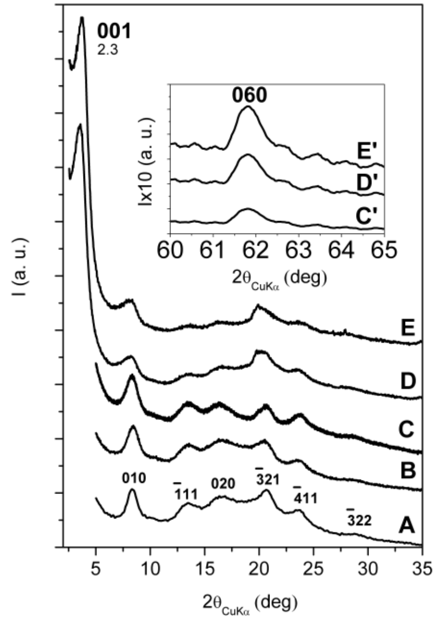

Fig. 1.17. X-ray diffraction (Cu Kα) patterns in the 2θ range 2-35° of sPS aerogels with as received OC, as obtained from gels with a solvent content of 90 %wt. and presenting different polymer/OC weight ratios: (A) 100/0; (B) 96/4; (C) 92/8; (D) 80/20; (E) 50/50. The insets C', D' and E' enlarge the 060 in-plane reflection of the clay. The Miller indexes of the main reflections of the nanoporous-crystalline δ form of sPS are indicated in A.

Additional information on the structural organization in the sPS/OC aerogels comes from DSC analyses. In particular, DSC heating scan of a 50/50 by %wt. sPS/as-received-clay aerogel is shown in **Fig. 1.16C**. The endothermic peak, corresponding to loss of rotator order in the interlayer spacing becomes broader and its maximum is shifted up to 50-60°C, with only a minor reduction of the related enthalpy ($\Delta H_r \approx 10$ J/g ≈ 20 J/g_{OC}).

The combined information of the X-ray diffraction patterns of **Figs I.17D,E** and the DSC scans of **Fig. I.16C** indicates that, for high clay content, the aerogel preparation procedure brings to a reduction of the OC basal spacing (d_{001}) from 3.5 nm down to 2.3 nm, with only partial loss of the hydrocarbon rotator order in the interlayer space.

The X-ray diffraction patterns of the sPS aerogels prepared with the exfoliated OC (**Fig. I.18**), independently of the aerogel composition, do not show 00ℓ clay reflections, while show the isolated weak 060 in-plane clay reflection (as shown by the inset of **Fig. I.18C',D'**). This clearly indicates that the gel and aerogel preparation procedures, also for high clay concentrations, allow to maintain clay exfoliation without re-aggregation.

In this respect, it is worth citing that X-ray diffraction patterns of polymer-clay aerogels as obtained by freeze-drying of polymer solutions including clays [71–73] show the presence of 00ℓ clay reflections, which exclude the occurrence of exfoliation.

The patterns of **Fig. I.18** also show that sPS is generally crystallized in the nanoporous δ form (**Figs I.18A-C**) while, for the 50/50 polymer/exfoliated-OC aerogel, the sPS crystallization does not occur (broad amorphous halo of **Fig. I.18D**). This is probably due to the good dispersion of a large amount of exfoliated OC, leading to a diluting effect on sPS that reduces its crystallization kinetics. This loss of polymer crystallinity leads to a loss of the typical fibrillar structure, which in turn allows rationalizing the loss of monolithic structure.

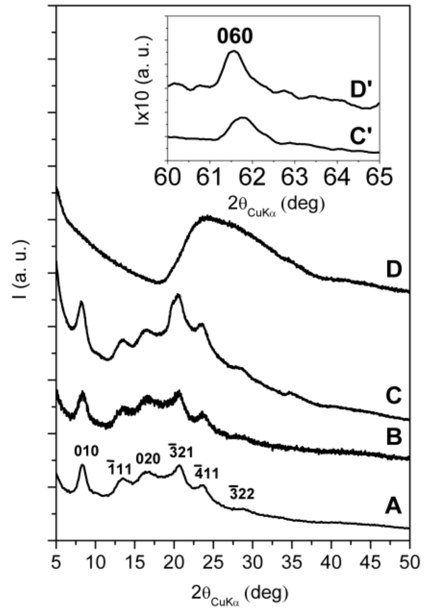

Fig. I.18. X-ray diffraction (Cu Kα) patterns in the 2θ range 5-50° of sPS aerogels with exfoliated OC, as obtained from gels with a solvent content of 90 %wt. and presenting different polymer/OC weight ratios: (A) 100/0; (B) 95/5; (C) 80/20; (D) 50/50. The inset C', D' enlarges the 060 in-plane reflection of the clay.

I.3.3 Comparison between Aerogels with Intercalated and Exfoliated Organoclays

This section presents a strict comparison between properties of sPS monolithic aerogels exhibiting a porosity of 90% and a OC content of 20 %wt., as obtained by using intercalated or exfoliated OC, that present the X-ray diffraction patterns shown in **Figs I.17D** and **I.18C**, respectively.

On the basis of quantitative evaluations on the X-ray diffraction patterns, the two aerogels present similar degree of polymer crystallinity (≈ 40%). However, aerogels with the exfoliated clay (**Fig. I.19A**) are much more homogeneous than aerogels obtained with the intercalated OC (**Fig. I.19B**), which clearly present rough surfaces.

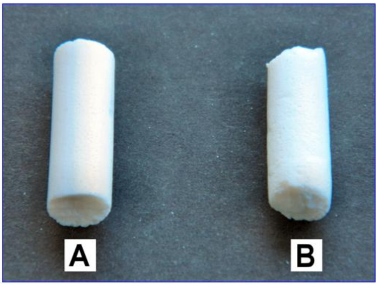

Fig. I.19. Photographs of cylindrical monolithic (diameter of 7 mm) sPS/OC aerogels, with porosity *P*= 90%, as obtained by $scCO_2$ drying and exhibiting a 80/20 weight ratio: (A) with exfoliated clay; (B) with intercalated clay. The shown aerogels essentially present the same size and shape of the precursor gels.

Also the SEM images of the two aerogels are completely different. In fact, the SEM of the aerogel including the intercalated OC is dominated by the micrometric OC particles (**Fig. I.20B**) while the SEM of the aerogel including the exfoliated OC (**Fig. I.20A**) clearly show both nanometric clay platelets and nanometric sPS fibrils (**Fig. I.20A'**).

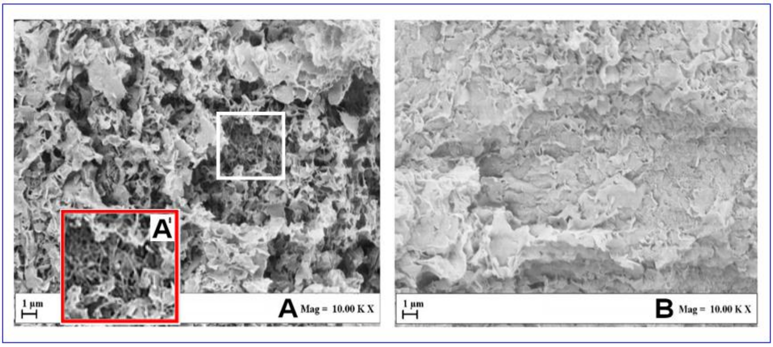

Fig. I.20. SEM of aerogels with porosity *P*= 90%, having 80/20 polymer/OC weight ratio: (A, A') with exfoliated OC; (B) with intercalated OC.

The results of the SEM analyses suggest that also the large difference in the visual appearance between the two aerogels of **Fig. I.19** could be due to micrometric and nanometric size of intercalated and exfoliated clays, respectively.

DMA analyses (see paragraph 9.13 in Section IV for experimental details) indicate that the aerogel based on the exfoliated clay present an elastic modulus definitely higher than for those based on intercalated OC (36 MPa vs 15 MPa).

Surface areas, S_{BET}, as obtained by N_2 adsorption data at 77 K, for the intercalated and exfoliated OC, as well as those of the corresponding aerogels, are compared in **Table I.1.** For the sake of comparison, S_{BET} of the neat sPS aerogel presenting the same porosity is shown in the last row of **Table I.1**. As well known, sPS aerogels exhibit high surface areas, mainly associated with the crystalline cavities of the δ crystalline phase, but also associated with the amorphous aerogel porosity.[67,68] In agreement with literature data,[74] S_{BET} of the OC is rather low and is substantially increased for the exfoliated OC (S_{BET} = 18 m^2/g). The sPS/exfoliated-clay aerogels present values of S_{BET} (281 m^2g^{-1}) much higher than those of the sPS/intercalated-clay aerogels (166 m^2g^{-1}) and not far from those observed for pure sPS aerogels (312 m^2g^{-1}). This indicates that, also for this high OC content (20 %wt.), the exfoliated clay not only does not disturb the formation of the nanoporous crystalline phase but also does not alter the amorphous aerogel porosity.

Table 1.1. Total surface area (S_{BET}) of OC samples and of aerogels with porosity P= 90%, having 80/20 polymer/OC weight ratio.

Sample	S_{BET}[a] (m^2g^{-1})
Intercalated OC (Dellite® 67G)	10
Exfoliated OC ($scCO_2$ treated)	18
sPS/intercalated-OC, 80/20 aerogel	166
sPS/exfoliated-OC, 80/20 aerogel	281
Aerogel δ sPS	312

[a] Total area evaluated following the BET model in the standard $0.05<P/P_0<0.3$ pressure range.

A schematic representation of the sPS/exfoliated-OC aerogels is shown in **Scheme 1.4**.

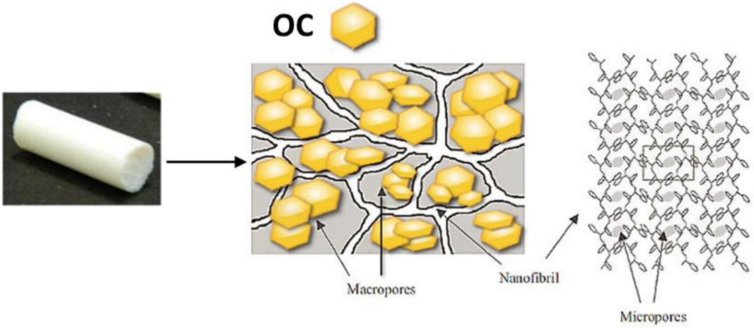

Scheme 1.4. Schematic representation of the sPS/exfoliated-OC aerogels.

So, a thorough investigation of $scCO_2$-induced exfoliation of OCs was conducted mainly by X-ray diffraction and DSC characterization techniques.

A complete control over the degree of order of the OC structures was achieved. In particular ordered clay structures were obtained by intercalation of long-chain ammonium cations in the interlayer spaces of pristine MMT, in presence or in absence of a second polar guest. Instead, disordered clay structures were obtained by $scCO_2$-induced exfoliation of OCs, as reported above. The exfoliation state of exfoliated clays was preserved by preparing clay rich polymer/clay aerogels.

References

[1] S. Guggenheim, R. T. Martin. *Clays and Clay Minerals* **1995**, *43*, 255–256.

[2] M. Galimberti. Rubber Clay Nanocomposites-Science, Technology and Applications, Wiley and Sons, New York, **2011**.

[3] F. Bergaya, G. Lagaly. Handbook of Clay Science, Second Edition. Elsevier, Amsterdam, **2013**.

[4] M. Galimberti, A. Lostritto, A. Spatola, G. Guerra. *Chem. Mater.* **2007**, *19*, 2495−2499.

[5] Powder diffraction database 70-2151 International Centre for Diffraction Data, *PCPDF win. Version2.02*, **1999**.

[6] F. A. Bergaya. *Microp. Mesop. Mater.* **2008**, *107*, 141–148.

[7] L. B. Paiva, A. R. Morales, F. R. Valenzuela Díaz. *Appl. Clay Sci.* **2008**, *42*, 8–24.

[8] I. Natali Sora, R. Pelosato, L. Zampori, D. Botta, G. Dotelli, M. Vitelli. *Appl. Clay Sci.* **2005**, *28*, 43–54.

[9] T. S. Anirudhan, M. Ramachandran. *Appl. Clay Sci.* **2007**, *35*, 276–281.

[10] Q. Yue, Q. Li, B. Gao, A. Yuan, I. Wang. *Appl. Clay Sci.* **2007**, *35*, 268–275.

[11] S. M. Lee, D. Tiwari. *Appl. Clay Sci.* **2012**, *60*, 84–102.

[12] D. W. Litchfield, D. G. Baird. *Rheol. Rev.* **2006**, 1–60.

[13] L. Zampori, P. Gallo Stampino, G. Dotelli, D. Botta, I. Natali Sora, M. Setti. Appl. Clay Sci. **2008**, *41*, 149–157.

[14] L. Zampori, P. Gallo Stampino, G. Dotelli. *Appl. Clay Sci.* **2009**, *42*, 605–610.

[15] M. I. Carretero, M. Pozo. *Appl. Clay Sci.* **2010**, *47*, 171–181.

[16] K. Campbell, D. Q. M. Craig, T. McNally. *Int. J. Pharm.* **2008**, *363,* 126–131.

[17] G. V. Joshi, B. D. Kevadiya, H. A. Patel, H. C. Bajaj, R. V. Jasra. *Int. J. Pharm.* **2009**, *374,* 53–57.

[18] C. Viseras, P. Cerezo, R. Sanchez, I. Salcedo, C. Aguzzi. *Appl. Clay Sci.* **2010**, *48,* 291–295.

[19] P. C. LeBaron, Z. Wang, T. J. Pinnavaia. *Appl. Clay Sci.* **1999**, *15,* 11–29.

[20] M. Alexandre, P. Dubois. *Mat. Scie. Eng.* **2000**, *28,* 1–63.

[21] S. S. Ray, M. Okamoto. *Progr. Polym. Sci.* **2003**, *28,* 1539–1641.

[22] B. Chen, J. R. G. Evans, H. C. Greenwell, P. Boulet, P. V. Coveney, A. A. Bowden, A. Whiting. *Chem. Soc. Rev.* **2008**, *37,* 568–594.

[23] C. Della Porta. Industrial treatments and modification of clay minerals, in: M. Galimberti (Ed.), Rubber Clay Nanocomposites - Science, Technology and Applications, Wiley and Sons, New York, pp. 87–100, **2011**.

[24] M. Galimberti, S. Senatore, L. Conzatti, G. Costa, G. Giuliano, G. Guerra. *Polym. Adv. Technol.* **2009**, *20,* 135–142.

[25] M. Galimberti, S. Giudice, V. Cipolletti, G. Guerra. *Polym. Adv. Technol.* **2010**, *21,* 679–684.

[26] M. Ogawa, T. Handa, K. Kuroda, C. Kato. *Chem. Lett.* **1990**, *19,* 71–74.

[27] M. Ogawa, M. Hirata, K. Kuroda, C. Kato. *Chem. Lett.* **1992**, 365–368.

[28] M. Ogawa, H. Shirai, K. Kuroda, C. Kato. Clays and Clay Minerals **1992**, *40,* 485–490.

[29] J. Bujdak, H. Slosiarikova. *Appl. Clay Sci.* **1992**, *7,* 263–269.

[30] D. Merinska, Z. Malac, M. Pospisil, Z. Weiss, M. Chmielova, P. Capkova, J. Simonik. *Comp. Interf.* **2002**, *9,* 529–540.

[31] P. Capková, M. Pospíšil, M. Válášková, D. Merínská, M. Trchová, Z. Sedláková, Z. Weiss, J. Šimoník. *J. Coll. Intera. Sci.*

2006, *300,* 264–269.

[32] K. I. Breakwell, J. Homer, M. A. M. Lawrence, W. R. McWhinnie. Polyedron **1995**, *14,* 2511–2518.

[33] G. W. Beall, M. Gross. *Appl. Clay Sci.* **2004**, *27,* 179–186.

[34] S. Yoshimoto, F. Osashi, T. Kameyama. *Sol. Sta. Comm.* **2005**, *136,* 251–256.

[35] U. Riaz, S. M. Ashraf. *Appl. Clay Sci.* **2011**, *52,* 179–183.

[36] L. B. Paiva, A. R. Morales. *Braz. J. Chem. Eng.* **2012**, *29,* 525–536.

[37] S. Y. Chazhengina, E. N. Kotelnikova, I. V. Filippova, S. K. Filatov. *J. Mol. Struct.* **2003**, *647,* 243–257.

[38] M. Dirand, Z. Achour-Boudjema. *J. Mol. Struct.* **1996**, *375,* 243–248.

[39] V. Chevallier, D. Petitjean, M. Bouroukba, M. Dirand. *Polymer* **1999**, *40,* 2129–2137.

[40] D. Fu, Y. Liu, Y. Su, G. Liu, D. Wang. *J. Phys. Chem. B* **2011**, *115,* 4632–4638.

[41] D. Fu, Y. Liu, G. Liu, Y. Su, D. Wang. *Phys. Chem. Chem. Phys.* **2011**, *13,* 15031–15036.

[42] G. Ungar, N. Mašić. J. Phys. Chem. **1985**, *89,* 1036–1042.

[43] T. Itoh, N. Ohta, T. Shichi, T. Yui, K. Takagi. *Langmuir* **2003**, *19,* 9120–9126.

[44] M. Mauro, M. Maggio, V. Cipolletti, M. Galimberti, P. Longo, G. Guerra. *Carbon* **2013**, *61,* 395–403.

[45] M. A. Osman, M. Ernst, B. H. Meier, U. W. Suter. *J. Phys. Chem. B* **2002**, *106,* 653–662.

[46] M. E. Rerek, D. Van Wyck, R. Mendelsohn, D. J. Moore. *Chem. Phys. Lipids* **2005**, *134,* 51–58.

[47] H. Heinz, H. J. Castelijns, U. W. Suter. *J. Am. Chem. Soc.* **2003,** *125,* 9500-9510.

[48] Y. C. Lee, C. L. Kuo, S. B. Wen, C. P. Lin. *Appl. Clay Sci.* **2007**, *36,* 265–270.

[49] A. R. Ramadan, A. M.K. Esawi, A. A. Gawad. *Appl. Clay Sci.*

2010, *47,* 196–202.

[50] K. C. Baker, M. Manitiu, R. Bellair, C. A. Gratopp, H. N. Herkowitz, R. M. Kannan. *Acta Biomaterialia* **2011**, *7,* 3382–3389.

[51] C. Chen, J. Samaniuk, D. G. Baird, G. Devoux, M. Zhang, R. B. Moore, J. P. Quigley. *Polymer* **2012**, *53,* 1373–1382.

[52] S. Feng-hua, H. Han-xiong, Z. Yang. *Compos. Part B* **2011**, *42,* 421–428.

[53] J. Ma, E. Bilotti, T. Peijs, J. A. Darr. *Eur. Polym. J.* **2007**, *43,* 4931–4939.

[54] Q. T. Nguyen, D. G. Baird. *Polymer* **2007**, *48,* 6923–6933.

[55] J. Samaniuk, D. Litchfield, D. Baird. *Polym. Eng.& Sci.* **2009**, *49,* 2329–2341.

[56] M. A. Treece, J. P. Oberhauser. *J. Appl. Polym. Sci.* **2007**, *103,* 884–892.

[57] S. Horsch, G. Serhatkulu, E. Gulari, R. M. Kannan. *Polymer* **2006**, *47,* 7485−7496.

[58] M. Manitiu, R. J. Bellair, S. Horsch, E. Gulari, R. M. Kannan. *Macromolecules* **2008**, *41,* 8038–8046.

[59] M. L. Anderson, R. M. Stroud, D. R. Rolison. *Nano Letters* **2002**, *2,* **235–240.**

[60] S. S. Kistler. *Nature* **1931**, *127,* 741.

[61] S. O. Kucheyev, M. Stadermann, S. J. Shin, J. H. Satcher, S. A. Gammon, S. A. Letts, T. Van Buuren, A. V. Hamza. *Adv. Mater.* **2012**, *24,* 776−780.

[62] S. Longo, J. G. Vitillo, C. Daniel, G. Guerra. *ACS Appl. Mater. Interf.* **2013**, *5,* 5493−5499.

[63] S. Malik, D. Roizard, J. M. Guenet. *Macromolecules* **2006**, *39,* 5957–5959.

[64] C. De Rosa, G. Guerra, V. Petraccone, B. Pirozzi. *Macromolecules* **1997**, *30,* 4147–4152.

[65] G. Milano, V. Venditto, G. Guerra, L. Cavallo, P. Ciambelli, D. Sannino. *Chem. Mater.* **2001**, *13,* 1506–1511.

[66] V. Petraccone, O. Ruiz de Ballesteros, O. Tarallo, P. Rizzo, G.

Guerra. *Chem. Mater.* **2008**, *20,* 3663–3668.

[67] C. Daniel, D. Alfano, V. Venditto, S. Cardea, E. Reverchon, D. Larobina, G. Mensitieri, G. Guerra, G. *Adv. Mater.* **2005**, *17,* 1515–1518.

[68] C. Daniel, S. Giudice, G. Guerra. *Chem. Mater.* **2009**, *21,* 1028–1034.

[69] C. Daniel, S. Longo, R. Ricciardi, E. Reverchon, G. Guerra. *Macromol. Rapid. Commun.* **2013**, *34,* 1194–1207.

[70] G. Guerra, C. Daniel, P. Rizzo, O. Tarallo. *J. Polym. Sci. Part B* **2012**, *50,* 305–322.

[71] S. Bandi, M. Bell, D. A. Schiraldi. *Macromolecules* **2005**, *38,* 9216–9220.

[72] T. Pojanavaraphan, D. A. Schiraldi, R. Magaraphan. *Appl. Clay Sci.* **2010**, *50,* 271–279.

[73] Y. Wang, S. M. Alhassan, V. H. Yang, D. A. Schiraldi. *Composites: Part B* **2013**, *45,* 625–630.

[74] Y. Park, G. A. Ayoko, R. L. Frost. *J. Colloid Interface Sci.* **2011**, *360,* 440–456.

Chapter 2

Graphites and Derived Compounds

2.1 Carbon Allotropes

Carbon, the sixth element in the Periodic Table of Elements, is truly remarkable for its extraordinary ability of catenation to combine with itself and other chemical elements in different ways and thereby form the basis of organic chemistry and of life. Diamond and graphite are well-known allotropes of carbon. Elemental carbon with sp^3 hybridization builds up a tetrahedral lattice, giving rise to diamond (**Fig. 2.1A**), while sp^2 hybridized extended networks are responsible for the formation of graphite (**Fig. 2.1B**).

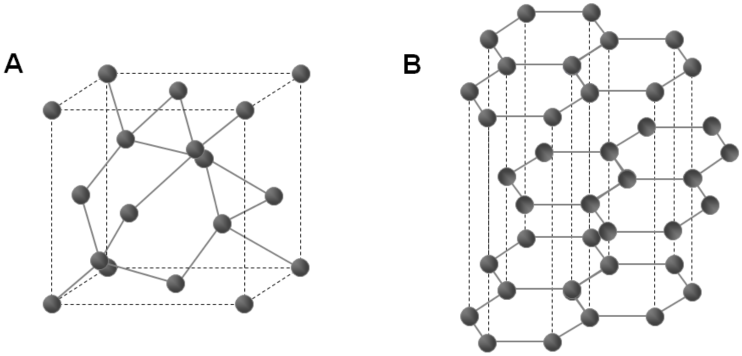

Fig. 2.1. Crystal structures of (A) diamond and (B) hexagonal graphite.

Graphene is an atomically thick, two-dimensional (2D) sheet composed of sp^2 carbon atoms arranged in a honeycomb structure (**Scheme 2.1**). It has been viewed as the building block of all other graphitic carbon allotropes of different dimensionality. For example, graphite (3D carbon allotrope) is made of graphene sheets piled on top of each other with *…ABABAB…* stacking and separated by 0.335 nm. More disordered graphitic structures exist for coals, cokes and carbon blacks. The 0D carbon allotrope, fullerenes (buckyballs), can be envisioned to be made by wrapping a section of graphene sheet. The 1D carbon allotropes, carbon nanotubes (CNT), can be made by rolling graphene sheets.

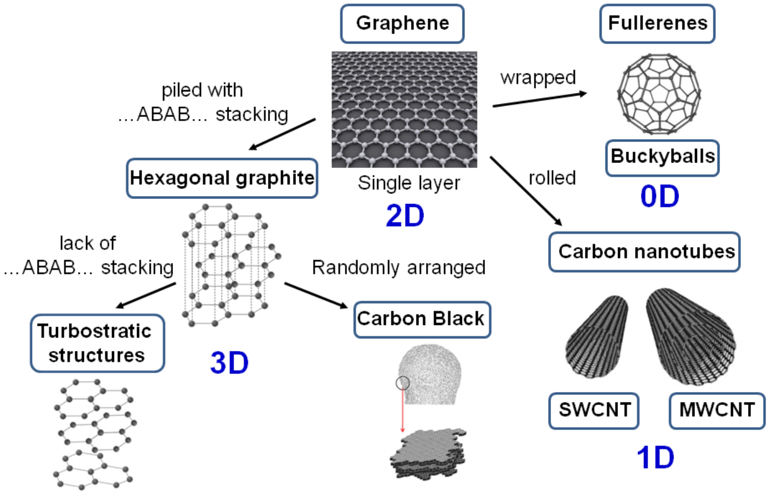

Scheme 2.1. Mother of all graphitic forms. Graphene is a 2D building material for carbon materials of all other dimensionalities. It can be wrapped up into 0D buckyballs, rolled into 1D nanotubes, piled with a *…ABABAB…* stacking into 3D graphite or randomly stacked in primary particles of carbon black.

2.2 Structures of Layered Carbons

Materials with layers of sp^2-bonded carbon atoms exhibit a large variety of structures characterized by different degree of structural order and morphologies. These materials, principally, differ for their degree of order perpendicular to the graphitic layers (out-of-plane order) and in the graphitic layers (in-plane order).

The structures of layered carbons, from ordered graphites to amorphous carbons, are discussed in the following.

A systematic X-ray diffraction characterization of different graphitic materials was also performed, in order to select the most suitable starting material for the preparation of anisotropic carbon nanofillers to be used in rubber nanocomposites.

2.2.1 Graphites

Graphite is a crystalline, polymorphic form of elementary carbon with ordered layers. Each carbon atom in the graphite crystal is hybridised trigonally, forming three σ and one π bonds. The hybridised orbitals of the sp^2 type give σ bonds of a length of 1.42 Å, arranged at 120° angles with respect to one another, with sheets made up of regular hexagons. The fourth electron of each atom, being in the p orbital, forms π bonds with all the neighbouring atoms. The structure of graphite consists of six-membered rings in which each carbon atom has three near neighbours at the apices of an equilateral triangle. Within the large planar layers, there are linkages intermediate between atomic and metallic bonds. The layers in the crystal are held together by van der Waals bonding forces. Weak bonding perpendicular to the layers gives rise to easy gliding parallel to the sheets.[1]

According to the structural model proposed by Hull in 1917 [2] and described by Bernal in 1924,[3] the hexagonal unit cell of hexagonal graphite contains four atoms in the positions listed below compared to the reference system in **Fig. 2.2**:

$$(0,0,0)\ ;\ (0,0,1/2)\ ;\ (1/3,2/3,1/2)\ ;\ (2/3,1/3,0)$$

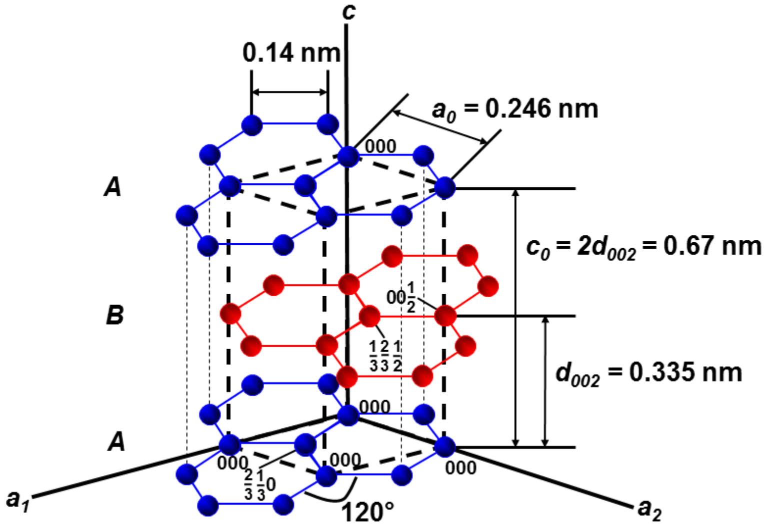

Fig. 2.2. Detailed crystal structure of hexagonal graphite.

Hexagonal graphite consists of sheets stacked along the crystallographic *c* axe with a regular …*ABABAB*… sequence and lattice costant c_0= 0.67 nm (see **Fig. 2.2**).

The X-ray diffraction analysis is the most powerful tool to study the structure of graphites and of carbon materials in general. The hexagonal graphite reflections can be classified into three groups: reflections with 00ℓ, hk0 and hkℓ indices. Reflections with 00ℓ are due to the diffraction from the basal planes stacked along the crystallographic *c* axe. Only even ℓ values are permitted because of the systematic extinction of 00ℓ reflections with odd ℓ values, related to the …*ABABAB*… stacking. Reflections with hk0 are due to the diffraction from the crystal planes perpendicular to the basal planes and the hkℓ reflections are related to the diffraction from the inclined planes respect to the basal planes.

The X-Ray diffraction pattern of hexagonal graphite in **Fig. 2.3** [4] presents the 002, 004 and 006 reflections characteristic of the stacking along the crystallographic *c* axe, while the 100 and 110 reflections are related to the order inside the graphitic layers. The distance between the *A* and *B* planes is the Bragg's distance d_{002} = 0.335 nm and the distance between the *A* and *A* planes is the lattice costant $c_0 = 2d_{002}$ = 0.67 nm. The Bragg's distances $d_{100} = a_0 \cdot cos(30°)$ = 0.213 nm and $d_{110} = a_0 \cdot sin(30°)$ = 0.123 nm, are related to the 100 and 110 planes, orthogonal to the *A* and *B* planes (see **Fig. 2.2**).

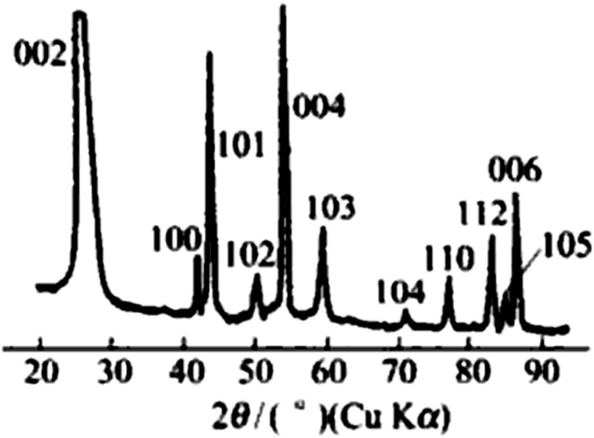

Fig. 2.3. X-ray diffraction (Cu Kα) pattern of hexagonal graphite, after ref. 4.

2.2.2 Turbostratic Graphites

The described hexagonal structure of graphite refers to its crystalline form defined as ideal models. However, in nature graphite usually appears in less perfect forms and in a variety of disordered types from the so-called turbostratic graphites to the amorphous carbons.

According to the random layer lattice structural model proposed by Warren in 1941, turbostratic graphite is characterized by the lack of …*ABABAB*… stacking with graphitic sheets randomly translated to each other and rotated respect to the normal of the layers (see **Scheme 2.2**).[5]

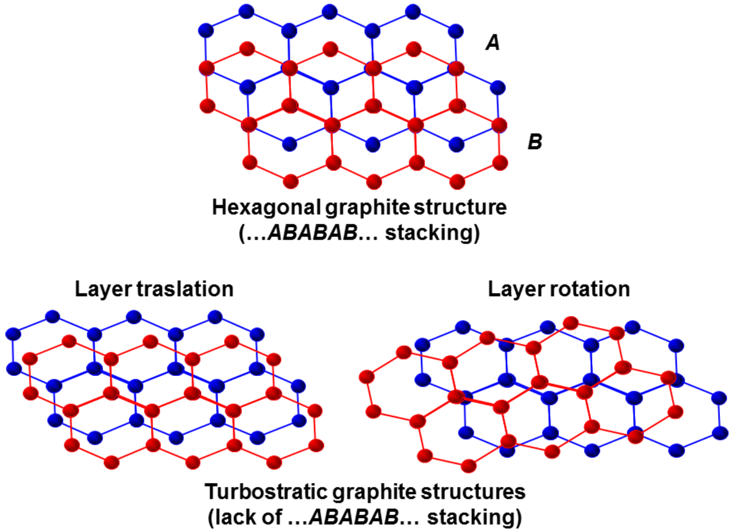

Scheme 2.2. Top view of the turbostratic graphite structures compared with the hexagonal graphite structure, after ref. 4.

Distortions from the hexagonal graphite structure determine the intensity decrease or the disappearance of hkℓ reflections, such as 101, 102, 103, 104, 105 and 112, while the 00ℓ and the hk0 reflections are not suppressed. The Bragg's distance d_{002} and the width at half height β_{002} increase.[6]

Turbostratic structures are often observed in extensively ball-milled graphites [7] or in carbon materials heated at relatively low temperatures of 1300 – 1500 °C,[8] where the size of each layer is small and only a few layers are stacked in ordered manner. By heating these carbons to high temperatures, up to 3000 °C,[9] both the size and number of stacked layers usually increase, and the regularity in stacking is also improved. Heat treatment at intermediate temperatures gives a partial improvement in stacking regularity. A wide range of structures from completely turbostratic structures to graphite structures with pure ...*ABABAB*... stacking is possible, depending primary on the starting materials and the heat treatment temperature.

2.2.3 Amorphous Carbons

Amorphous carbons such as coals, cokes and carbon blacks are materials without long-range crystalline order. Short-range graphite-like order still exists, and the degree of this kind of order gives rise to intermediate structures between the graphitic and the completely amorphous (lack of any crystalline structure) carbons, according to the random layer lattice structural model.[5] Deviations of the interatomic distances and interbonding angles with respect to the graphite lattice as well as to the diamond lattice occur in such materials.

The X-Ray diffraction pattern of petroleum coke heat treated at 1000 °C in **Fig. 2.4** [4] is characterized by very broad 00ℓ reflections, due to the small number of layers stacked in an orered manner, unsymmetrical two-dimensional hk reflections, and no hkℓ reflections, due to random turbostratic stacking of the layers.

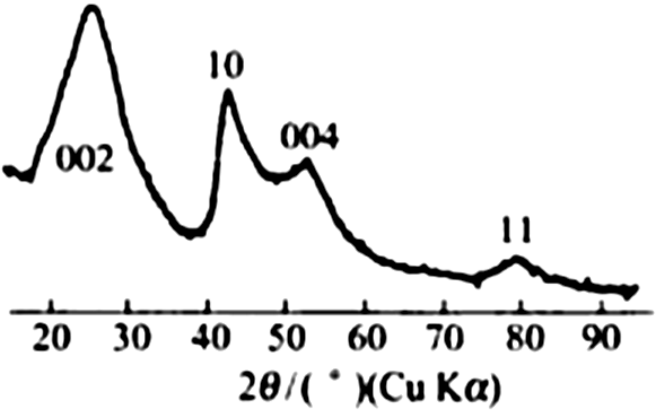

Fig. 2.4. X-ray diffraction (Cu Kα) pattern of petroleum coke heat treated at 1000 °C, after ref. 4.

The structure of amorphous carbons with short-range graphite-like order can be rationalized by the Franklin's model proposed in 1950.[10] According to this model, this kind of carbons are characterized by two types of carbon structures: carbon crystallites and completely amorphous carbon. Small graphitic crystallites, containing few layers, are joined together by cross-links. These cross-links are established by aliphatic chains on the edges of each crystalline domains. The structural units in non-graphitizing carbons are distributed randomly, and the cross-links are sufficiently strong to impede movement of the layers into a more parallel arrangement (see **Fig 2.5A**). The structural units in a graphitizing carbon are approximately parallel to each other, and the links between adjacent units are assumed to be weak (see **Fig 2.5B**).[11]

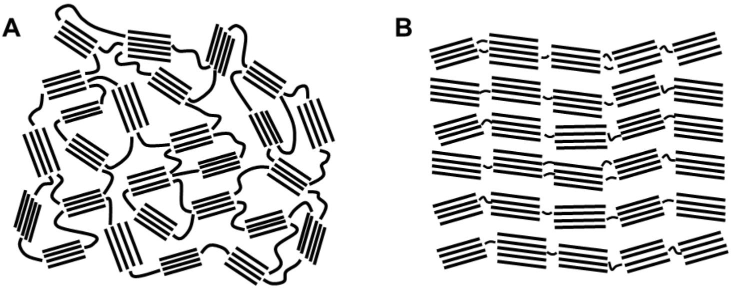

Fig. 2.5. Franklin's structural model of: (A) non-graphitizing and (B) graphitizing carbons, after ref. 11.

2.2.4 Carbon Blacks

Carbon blacks (CBs), formed through incomplete combustion of high molecular weight hydrocarbon fractions of petroleum crude oils, coal tar, ethylene cracking tar, and vegetable oil, are very important industrial products, in particular these materials are the most important reinforcing filler used to improve strenght, rolling resistance and abrasion resistance in tire compounds.

CB samples are characterized by aggregates (200 – 1000 nm) of nearly spherical particles (20 - 100 nm) with an internal structure made of graphite-like units having a random orientation of the graphitic layers, as shown in **Fig. 2.6**.[12]

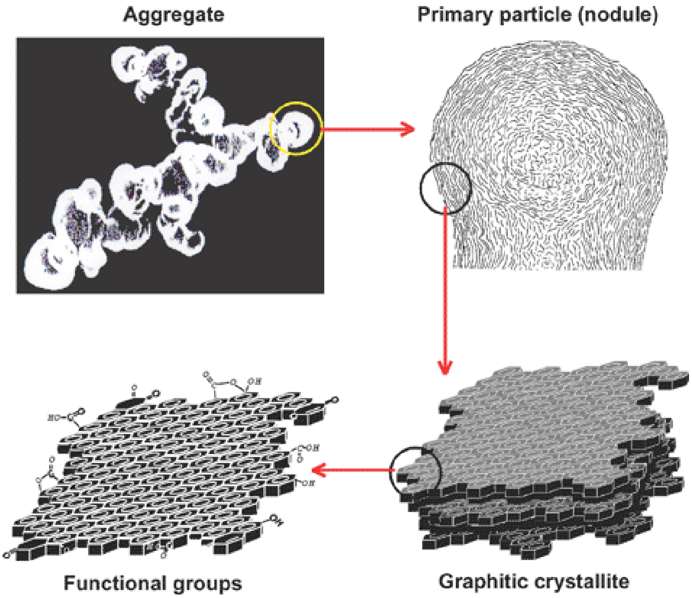

Fig. 2.6. Structure of carbon black aggregates, after ref. 12.

CB powders are characterized by high surface areas, as a consequence of their nanometric primary particles, that determine high filler-polymer interfacial areas, when CB particles are dispersed in a polymer matrix. The degree of aggregation of primary particles defines a very important technological parameter, the so-called "structure" of CBs. High structure CBs are characterized by high degree of aggregation (low void volume) (see **Fig. 2.7**)

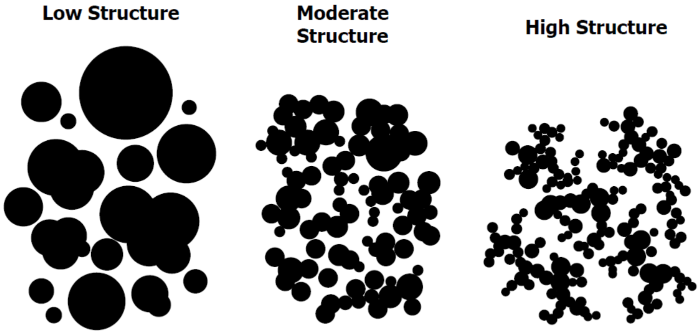

Fig. 2.7. Degree of aggregation of primary particles of carbon black.

Another peculiar feature of CB particles is their surface activity, that derives from both high energy graphitic edges and the oxygen groups (carbonyl, carboxylic, lactonic and phenolic groups), at the edges of each graphitic layer (see **Fig. 2.6**). The surface activity of CB particles is responsible for the filler-filler and filler-polymer interactions in polymeric nanocomposites.

2.3 Structural Characterization of Graphitic Materials for the Preparation of Anisotropic Carbon Nanofillers

Physical properties of fillers and of composites based on them are better when fillers have a high anisotropy,[13–17] that means when they have short and long correlation lengths in the direction perpendicular and parallel to the structural layers, respectively.

Among layered fillers based on sp^2-carbon atoms, highly anisotropic graphites, with a high in-plane order and a reduced out-of-plane order, are the most suitable starting material for the preparation of anisotropic carbon nanofillers. In this respect, aiming to select a graphite with high shape anisotropy of the crystallites and a long-range structural order in graphene layers, a systematic X-ray diffraction characterization of different graphitic materials was performed (for experimental details see paragraphs 8.1 and 9.1 in Section IV).

The X-ray diffraction patterns of six commercial graphitic materials are compared in **Fig. 2.8** and are organized from A to F, on the basis of a progressive reduction of structural order. The relative Williamson-Hall plots are presented in **Fig. 2.9** and the derived correlation lengths and strains, parallel and perpendicular to the structural layers, are reported in **Table 2.1**. Of course, errors in correlation lengths and strains, when only two reflections are available, can be large (up to 10 % for samples D-F).

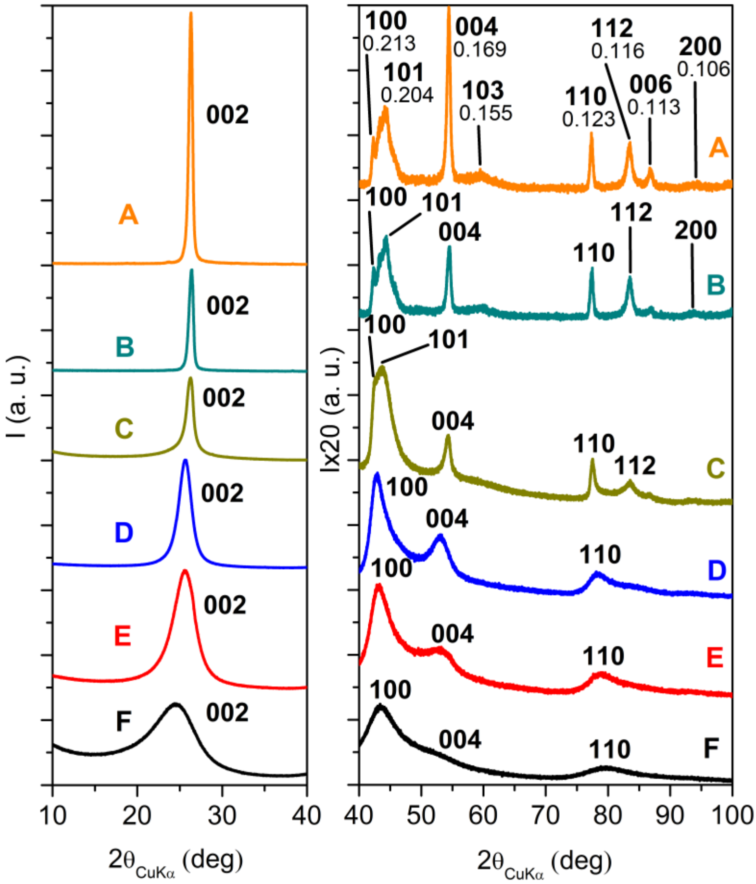

Fig. 2.8. X-ray diffraction patterns (Cu Kα) of six commercial graphitic materials: (A, B) graphites, (C) ball-milled graphite, (D, E) needle coke and calcined petroleum coke and (F) carbon black N326. The patterns are reported from A to F on the basis of a progressive reduction of structural order.

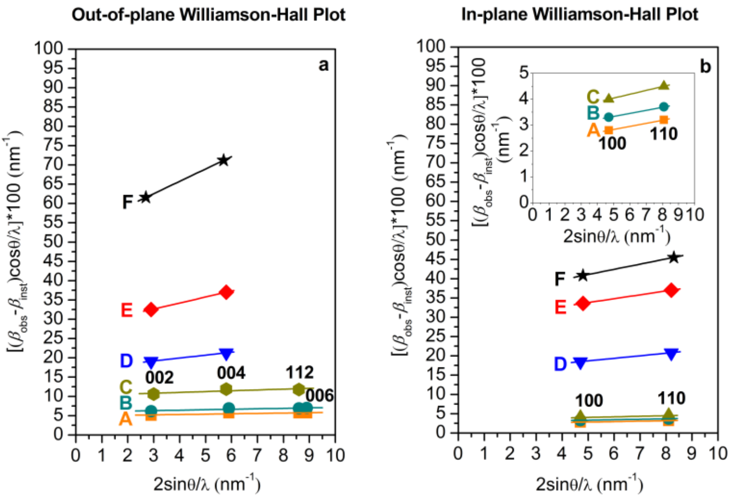

Fig. 2.9. Out-of-plane (a) and in-plane (b) Williamson–Hall plots for the graphitic samples from A to F, whose X-ray diffraction patterns are reported in Fig. 2.8.

Table 2.1. Structural parameters derived from Bragg's law and Williamson-Hall plots of Fig. 2.9.

Sample	d_{002} (nm)	$D_\perp$ (nm)	$D_\parallel$ (nm)	$D_\parallel / D_\perp$	$\varepsilon_\perp$ (%)	$\varepsilon_\parallel$ (%)	$\varepsilon_\perp / \varepsilon_\parallel$
A	0.339	20.3	44.5	2.2	0.047	0.059	0.8
B	0.339	16.8	36.4	2.2	0.060	0.059	1.0
C	0.339	9.8	30.2	3.1	0.107	0.073	1.5
D	0.34_7	5.9	6.5	1.1	0.38	0.33	1.1
E	0.34_8	3.5	3.6	1.0	0.78	0.50	1.5
F	0.36_5	1.9	2.9	1.5	1.6	0.67	2.4

All samples of **Fig. 2.8** present broad 00ℓ reflections and out-of-plane correlation lengths (3rd column of **Table 2.1**) from 20 nm down to 2 nm. Moreover, all samples of **Fig. 2.8**, due to their structural disorder, present distances between the structural layers (d_{002} in the 2nd column of **Table 2.1**) slightly larger than those of ordered graphite samples ($d_{002} = 0.335$ nm).[18]

In particular, for samples A-C, the in-plane correlation lengths (4th column of **Table 2.1**) are larger than the out-of-plane correlation lengths (3rd column of **Table 2.1**) and the out-of-plane correlation length is significantly reduced for sample C. Moreover, going from A to C there is also a progressive reduction of the intensities of the 101 and 112 reflections with respect to the hk0 reflections. This clearly indicates a progressive increase of disorder in the relative position of parallel graphitic layers and hence a tendency toward the so-called turbostratic graphite.[6] An almost perfect turbostratic structure is present in samples D-F, whose 101 and 112 reflections are negligible.

Samples D-F exhibit low out-of-plane correlation lengths (corresponding to few graphitic layers). However, their in-plane correlation lengths are also low, thus leading to poor shape anisotropy of the crystallites (5th column of **Table 2.1**).

The whole structural information from **Figs 2.8–2.9** (and **Table 2.1**) clearly indicates that the ball-milled graphite (sample C in **Fig. 2.8**, renamed G in the following), which presents the highest shape anisotropy ($D_{\parallel} / D_{\perp} = 3.1$, see **Scheme 2.3**), associated with a large in-plane correlation length and a reduced order in the relative position of parallel graphitic layers, appears to be the most suitable starting material for the preparation of anisotropic carbon nanofillers (see the next paragraphs) to be used in rubber nanocomposites.

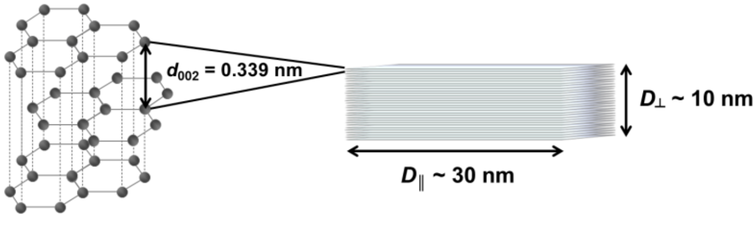

Scheme 2.3. Schematic representation of G with a basal spacing of $d_{002} = 0.339$ nm and a high shape anisotropy of $D_{\parallel} / D_{\perp} \approx 3$.

2.4 Graphite Oxide

Graphite oxide (GO) is a layered material, which can be obtained by chemical oxidation of graphite. Graphite oxide can be prepared by the treatment of graphite with strong mineral acids and oxidizing agents, typically via treatment with a mixture of sulfuric and nitric acid, using potassium chlorate, as in the Brodie's [19] or Staudenmaier's [20] methods, or with a mixture of sodium nitrate and concentrated sulfuric acid, using potassium permanganate, as in the Hummers' method.[21]

The precise structure of GO remains a matter of debate,[22] and, according to the Lerf-Klinowski model,[23] GO consists of oxidized sheets having oxygen containing functional groups, that confer polar surface properties and a strong hydrophilic character. Hydroxyl and epoxide groups are at the surface of the basal planes and carbonyl and carboxyl groups are at the edges. Therefore, GO forms colloidal dispersion in water, which are stabilized by negative charges from the carboxyl groups, without the need for any surfactant.[24]

2.4.1 Preparation, Composition and Surface Areas of Graphite Oxide Samples

Two sets of GO samples, containing higher (H-GO) and lower (L-GO) oxygen content, were prepared by using Staudenmaier's method [20] and Hummers' method,[21] respectively (for experimental details see paragraphs 8.6 and 8.7 in Section IV), starting from the highly anisotropic graphite G. The oxidation methods of G are represented in **Scheme 2.4**.

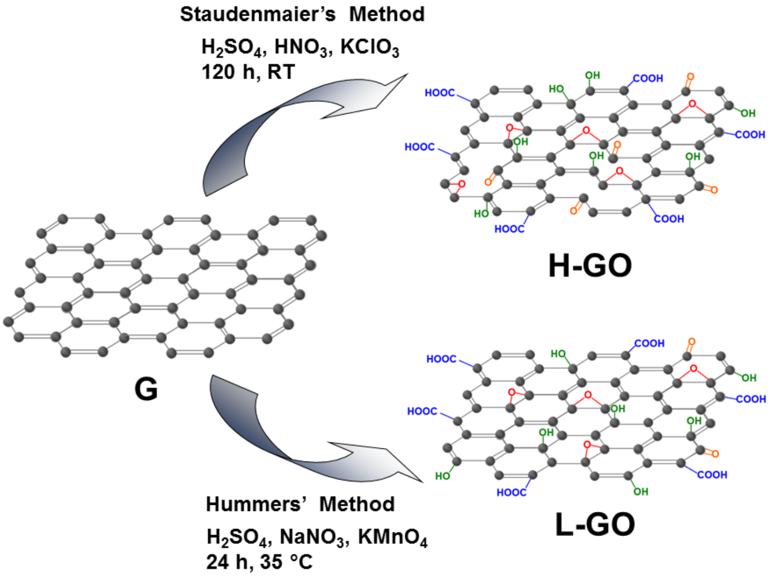

Scheme 2.4. Schematic representation of the oxidation reactions of the graphite (G) with Staudenmaier's and Hummers' methods.

Measurements of the water loss up to 150 °C by TGA (roughly 20 %wt. for H-GO and 5 %wt. for L-GO), reported in **Fig. 2.10**, and elemental analysis of the GO powders, reported in **Table 2.2**, indicate that the carbon to oxygen weight ratio (see C/O ratios in **Table 2.2**) in H-GO is about 1.6 and 1.9 in L-GO. Hence, the compositions of GO samples are $CO_{0.47}H_{0.2}\cdot 0.28H_2O$ for H-GO and $CO_{0.39}H_{0.12}\cdot 0.05H_2O$ for L-GO.

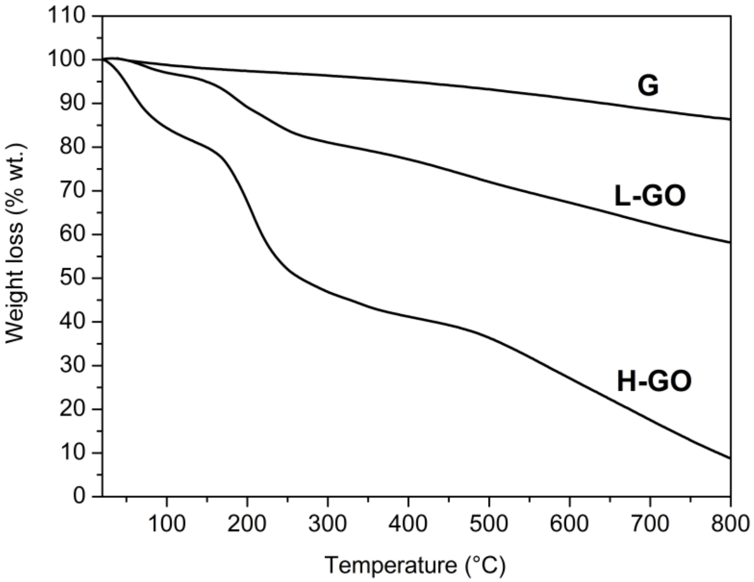

Fig. 2.10. TGA curves in N_2 of the starting high surface area graphite (G) and of the derived L-GO and H-GO.

Table 2.2. Results of elemental analysis and BET measurements on the starting high surface area graphite G and of the derived L-GO and H-GO.[a]

Sample	Surface area (m^2/g)	Elemental composition (%wt.)					
		C	H	N	O	S	C/O
G	308	99.8	0.1	0.1	0.0	0.0	/
L-GO	0.8	63.7	0.6	0.1	33.7	1.9	1.9
H-GO	1.1	59.1	1.4	0.1	35	4.4	1.6

[a] Elemental composition of the anhydrous GO samples: water contents of nearly 20 %wt. and 5 %wt. are evaluated by TGA for H-GO and L-GO, respectively.

Results of the BET measurements, reported in **Table 2.2**, show that G exhibits a high surface area, S_{BET} = 308 m^2/g, associated to its highly porous morphology, as shown in the SEM images in **Fig. 2.11**.

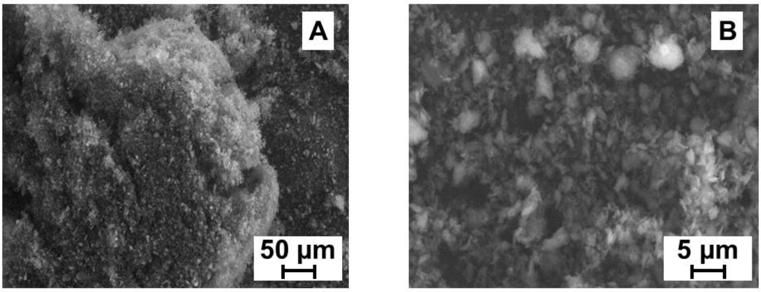

Fig. 2.11. SEM images of G at different magnifications: (A) 50 µm and (B) 5 µm.

The oxidation of G definitely decreases its surface area from 308 m^2/g to 0.8 m^2/g for L-GO and 1.1 m^2/g for H-GO. These surface area values agree well with those reported in the literature for GO samples.[25–27]

2.4.2 Characterization of Graphite Oxide Samples

FTIR spectra in **Fig. 2.12** show the presence of oxygenated functional groups on the layers of both H-GO and L-GO, whose concentration is negligible in the starting graphite sample (G). Absorption bands of carboxyl groups (1730 cm^{-1}), hydroxyl groups (stretching at 3420 cm^{-1} and bending at 1385 cm^{-1}) and epoxide groups (1145-1065 cm^{-1}) are observed.[28]

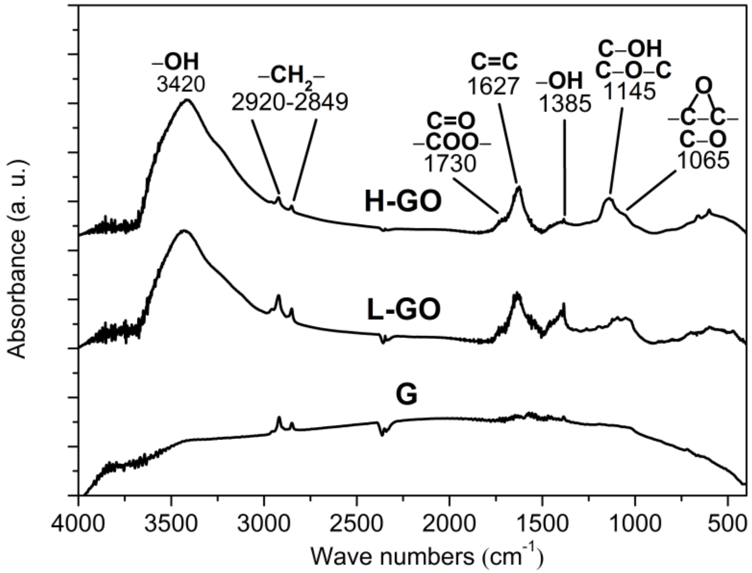

Fig. 2.12. FTIR spectra in the range 4000–400 cm^{-1} of the starting high surface area graphite (G) and of the derived L-GO and H-GO.

The TGA curves in **Fig. 2.10** also confirm the presence of oxygenated functional groups, infact, both GO samples exhibit a weight loss from 150 °C to 300 °C, caused by the decarboxylation reactions and a weight loss above 300 °C, associated to the removal of hydroxyl and epoxide groups.[29]

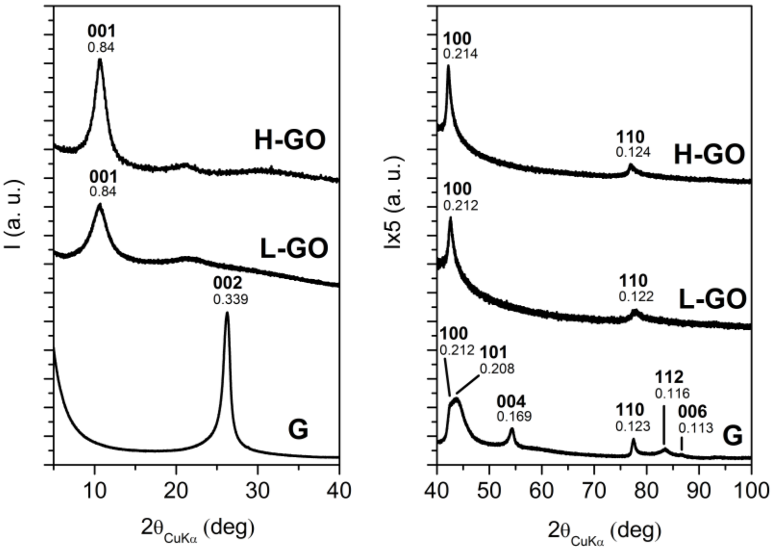

Fig. 2.13. X-ray diffraction patterns (Cu Kα) of the starting high surface area graphite (G) and of the derived L-GO and H-GO.

The X-ray diffraction patterns of GO samples in **Fig. 2.13** reveal a broad 001 reflection, corresponding to an interlayer distance of 0.84 nm, as already reported by some literature studies.[**30–35**] This value is higher than the interlayer distance observed in the starting graphite, about 0.339 nm. Hence, the oxidation of G produces an oxidized layered material with increased interlayer distance, from 0.339 nm to 0.84 nm, as represented in **Scheme 2.5**.

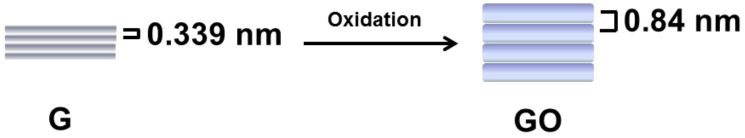

Scheme 2.5. Schematic representation of the increasing of the interlayer distance in GO after oxidation of graphite G.

The out-of-plane correlation lengths, determined by the Scherrer equation (see paragraph 9.1 and in Section IV) were 5.4

nm for H-GO and 4.5 nm for L-GO. Correspondingly, the in-plane periodicities (d_{100} and d_{110}) and correlation lengths ($D_{\parallel}$ = 30 nm) of both GO samples remain nearly unaltered with respect to the values observed in the starting graphite. Hence, GO layers present a long-range in-plane order as well as a high shape anisotropy of the crystallites ($D_{\parallel}$ / $D_{\perp}$ = 5.6 for H-GO and 6.7 for L-GO).

The pH back titration curves of GO samples dissolved in 0.05 M NaOH aqueous solution toward H^+ ion are given in **Fig. 2.14** (for experimental details see paragraph 9.9 and in Section IV). Different inflection points, corresponding to distinctive acidic groups, such as carboxylic and phenolic groups, that form sodium salts in the presence of sodium hydroxide, are observed. The CEC values were evaluated as 7.3 mmol/g for H-GO and as 5.7 mmol/g for L-GO, when 17.8 mmol of H^+ and 19.3 mmol of H^+ were added to the well dispersed colloidal solutions of H-GO and L-GO, respectively.

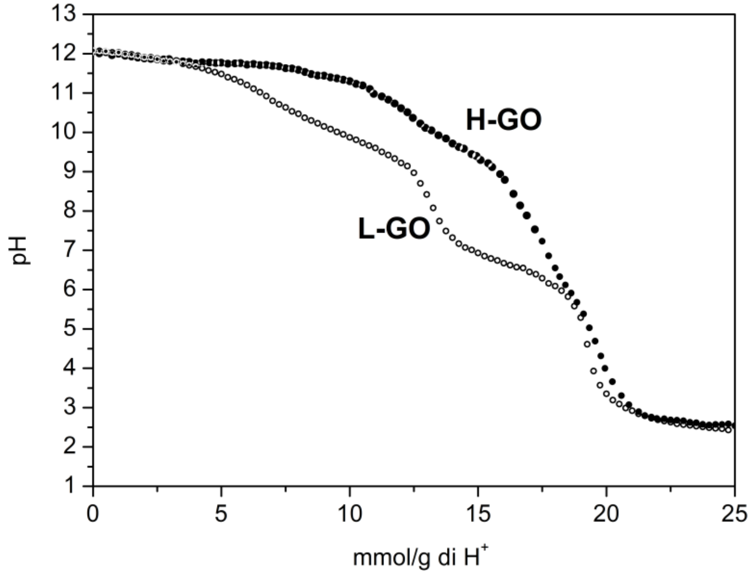

Fig. 2.14. The pH back titration curve of L-GO (empty circles) and H-GO (filled circles) dissolved in 0.05 M NaOH aqueous solution toward H^+ ion.

In analogy with the previously discussed OCs (see paragraph 1.2 in Section I), aiming to obtain graphitic fillers with improved compatibility with the rubber matrix, the intercalation chemistry of GO with organic ions was investigated. The method promotes a non-covalent functionalization of highly anisotropic GO layers and the results are discussed in the next paragraph.

2.5 Graphite and Graphite Oxide Intercalation Compounds

Graphite is a unique layered host, which is electro-active and can be either oxidized or reduced to form intercalation compounds (GICs). GICs are formed by the insertion of atomic or molecular layers of different chemical species between the layers of the graphite host lattice.[**36,37**] In GICs, the graphene layers either accept electrons from or donate electrons to the intercalated species. Graphite intercalated by electron donors like alkali metals (e.g. litium, potassium, sodium, etc.) are known as donor-type GICs,[**38–41**] whereas compounds formed by the intercalation of molecular species acting as electron acceptors like halogens, halide ions and acids are known as acceptor-type GICs.[**42–46**] The structural model of potassium graphite C_8K, according to Rüdorff and Schulze,[**37,47**] is shown in **Fig. 2.15.**

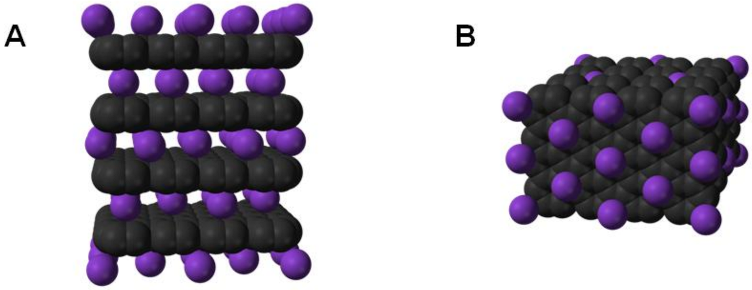

Fig. 2.15. Structural model of potassium graphite C_8K: (A) side view and (B) top view, after ref. 47.

The number of graphene layers between the intercalate layers is known as the stage and the most important and characteristic ordering property of GICs is the staging phenomenon depicted in **Scheme 2.6**. The stage number *n* designates the number of graphene layers that separate adjacent intercalate layers.

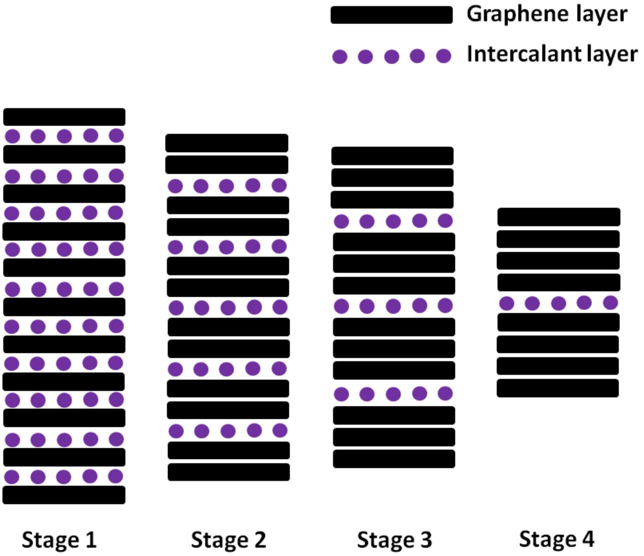

Scheme 2.6. Schematic diagram illustrating the staging phenomenon in GICs for stages $1 \leq n \leq 4$, after ref. 37.

When small ions, mainly inorganic, are intercalated, the observed crystalline structures generally exhibit a 3D long-range order as well order in the organization of the guest species in the interlayer space.[**38–43**] Their complete 3D order is comparable with those observed for many intercalate co-crystals, like those obtained for instance for organometallic [**48–50**] and polymeric co-crystals.[**51–57**]

GO layers also exhibit a rich intercalation chemistry, both with organic ions [**58–65**] and with polar polymers.[**66–69**] All known graphite oxide intercalation compounds (GOICs) present poor crystalline order, being generally limited to the distance between the graphite oxide layers, which can largely increase (also up to 5 nm).[**62**]

2.5.1 Preparation and Composition of Graphite Oxide Intercalation Compounds

GOICs, exhibiting a long-range order in the organization of the guest species in the interlayer space as well as a large distance between graphite oxide sheets, were prepared, according to the procedure reported in paragraph 8.8 in Section IV, by first dispersing GO powders in a aqueous solution of NaOH and by a further treatment with an aqueous solution of dimethyl ditallow ammonium chloride (2HTCl), in absence or in presence of polar molecules with long hydrocarbon chains, like stearic acid (SA), 2-stearamidoethyl stearate (SAES) (see the molecular structures in **Fig. 1.5**) and glyceryl tristearate (GTS) (see the molecular structure in **Fig. 2.16**). When the intercalation occurred in absence of a second polar guest, two GO/2HT intercalates with higher (GO/2HT-H) and lower (GO/2HT-L) contents of 2HT were obtained (see experimental details in paragraph 8.8 in Section IV). The GOIC samples, presented here have been prepared starting from H-GO and the results of the characterization are presented in the following discussion. Other intercalation experiments have been also carried out starting from L-GO, without any significant structural change of the obtained GOICs.

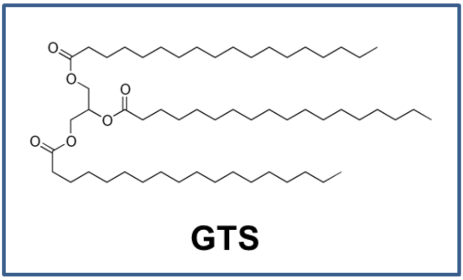

Fig. 2.16. Molecular structure of glyceryl tristearate (GTS).

On the basis of the guest weight uptake and measurements of the water loss by TGA, the composition of GO/2HT-L, GO/2HT-H, GO/2HT/SAES and GO/2HT/GTS intercalates has been evaluated as $CO_{0.47}H_{0.2}\cdot(C_{36}H_{76}N)_{0.059}\cdot 0.15H_2O$, $CO_{0.47}H_{0.2}\cdot(C_{36}H_{76}N)_{0.074}\cdot 0.15H_2O$, $CO_{0.47}H_{0.2}\cdot(C_{36}H_{76}N)_{0.059}\cdot(C_{38}H_{75}O_3N)_{0.057}\cdot 0.15H_2O$ and $CO_{0.47}H_{0.2}\cdot(C_{36}H_{76}N)_{0.059}\cdot(C_{57}H_{110}O_6)_{0.059}\cdot 0.15H_2O$, respectively. The content of 2HT guest ions was 3.0 mmol/g GO in GO/2HT-L and 3.8 mmol/g GO in GO/2HT-H. The content of the second polar guest, SAES in GO/2HT/SAES and GTS in GO/2HT/GTS, was roughly 3.0 mmol/g GO, with 2HT/SAES and 2HT/GTS molar ratios not far from 1/1.

The above reported compositions correspond to a molar ratio between carbon in the graphite oxide layers and alkyl chains of the intercalated guest species (C_{GO}/chains) of roughly 8/1 in GO/2HT-L, 6/1 in GO/2HT-H and 4/1 in GO/2HT/SAES and GO/2HT/GTS.

2.5.2 Characterization of Graphite Oxide Intercalation Compounds

The X-ray diffraction patterns of GOICs with lower and higher content of di(hydrogenated tallow)-dimethylammonium (2HT) are shown in **Fig. 2.17** (GO/2HT-L and GO/2HT-H, respectively).

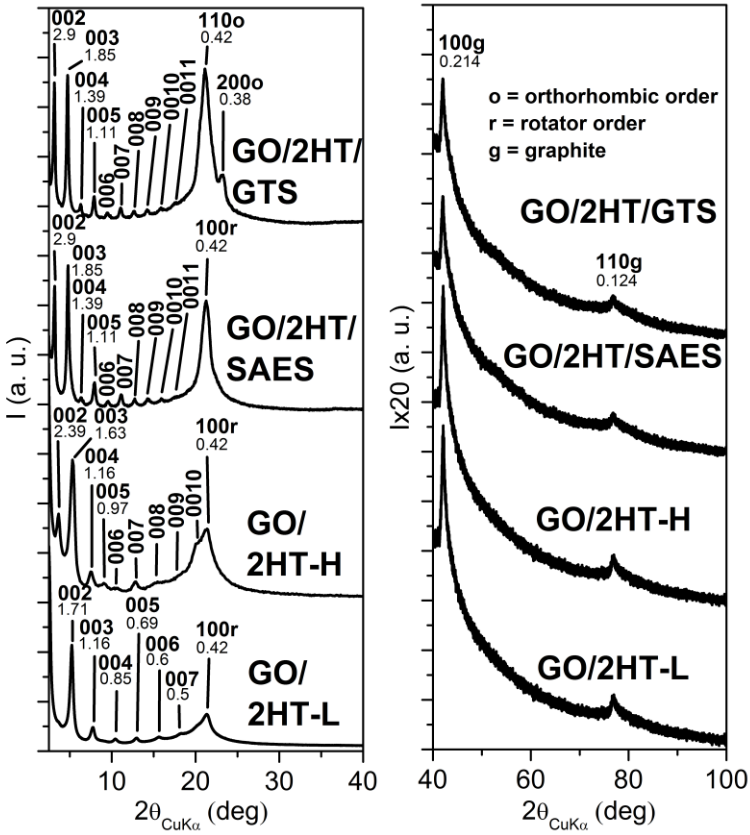

Fig. 2.17. X-ray diffraction patterns (Cu Kα) of the GOICs, which include the 2HT cation with two long hydrocarbon chains (GO/2HT-L and GO/2HT-H), 2HT and SAES (GO/2HT/SAES) or 2HT and GTS (GO/2HT/GTS). The symbols **g**, **r** and **o** indicate reflections relative to the graphite oxide planes, to the hexagonal rotator order and to the orthorhombic order, respectively.

The pattern of GO/2HT-L shows essentially unaltered 100 and 110 reflections, clearly indicating the maintenance of the in-plane graphite oxide order. Moreover, many narrow 00ℓ reflections (with ℓ up to 7) appear, which correspond to a spacing between graphite oxide layers of 3.4 nm with a correlation length increased up to 14 nm.

The pattern of GO/2HT-L in **Fig. 2.17** also presents a reflection at *d* = 0.42 nm, which suggests the occurrence of a hexagonal rotator order [70–75] of the long hydrocarbon chains of the intercalated ammonium salt. The broadness of this reflection indicates a correlation length of this hexagonal rotator order in the interlayer space, in directions parallel to the graphite oxide layers, close to 7 nm.

Surprisingly, the crystalline order of the GOICs can be largely increased by adding or an excess of 2HT (typically an amount of 2HT equal to 200% CEC of GO, see experimental details in paragraph 8.8 in Section IV) or 2HT in presence of a second guest species, including long hydrocarbon chains, like e.g. stearic acid (SA), 2-stearamidoethyl stearate (SAES) or glyceryl tristearate (GTS). In both cases the in-plane graphite oxide order is maintained, while all the other kinds of order above described are improved.

For instance, the patterns of GO/2HT-H and GO/2HT/SAES in **Fig. 2.17** show at least ten 00ℓ reflections with increased correlation lengths (*D* = 16 nm and 42 nm, respectively) and with largely increased spacings (*d* = 4.8 nm and 5.8, respectively).

The intense and narrow diffraction peak at *d* = 0.42 nm, typical of hexagonal arrangements of long n-alkanes,[70–75] indicates an increase of the correlation length for the hexagonal rotator order (in the direction parallel to the graphite oxide layers) up to 10 nm for GO/2HT/SAES. The occurrence of a hexagonal rotator order was also observed particularly for OCs with long-chain polar guests (see paragraph 1.2).

The pattern of GO/2HT/GTS shows a further ordered structure with the same periodicity of GO/2HT/SAES (*d* = 5.8

nm) and a larger correlation length in the direction perpendicular to the structural layers (*D* = 50 nm). However, the most interesting feature of GO/2HT/GTS intercalates is the orthorhombic order [70–75] of the long hydrocarbon chains of the intercalated guests in the direction parallel to the graphite oxide layers, as indicated by the reflections at *d* = 0.42 nm and *d* = 0.38 nm. In particular, it is worth adding that the reflection at *d* = 0.42 nm is the most intense reflection of the entire GO/2HT/GTS pattern, therefore the amount of the intercalated chains producing diffraction is largely increased with respect to GO/2HT/SAES.

The GOICs with rotator order in the intercalated layers, lead to polycrystalline films exhibiting macroscopic orientational order, by simple casting procedures. For instance, X-ray diffraction patterns of films having a thickness of nearly 30 μm, as obtained by casting from aqueous suspensions of GO and of the derived GO/2HT/SAES intercalate, are shown in **Figs 2.18A** and **2.18B**, respectively.

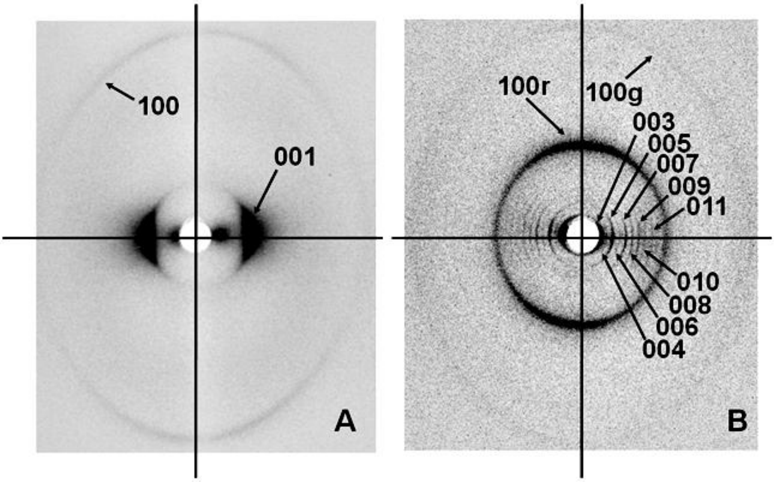

Fig. 2.18. Photographic X-ray diffraction patterns (Cu Kα) of films cast from aqueous suspensions of graphite oxide (A) and of the derived GOIC with 2HT and SAES (B), as collected with the X-ray beam parallel to the film (EDGE patterns). The hkℓ Miller indexes

of the main reflections are indicated and the symbols **g** and **r** discriminate 100 reflections relative to the graphite oxide planes and to the rotator order, respectively.

In particular, the EDGE patterns, i.e. photographic patterns taken with X-ray beam parallel to the film surface, present intense (00ℓ) reflections on the equatorial line (corresponding to the already described interlayer distances of 0.84 nm and 5.8 nm for GO and GO/2HT/SAES in **Fig. 2.17**). As already described for GO,[76] these diffraction data can be rationalized by the orientation of the graphite oxide layers preferentially parallel to the film plane. By using the procedure described in paragraph 9.1 in Section IV, a degree of parallelism of this plane with respect to the film surface has been evaluated as $f_{00\ell} \approx 0.85$. As for the reflection at $d = 0.42$ nm in **Fig. 2.18B**, its polarization along the meridian of the EDGE pattern is in agreement with the assignment as 100 reflection of a hydrocarbon rotator order, nearly perpendicular to the graphite oxide layers. Analogous results have been obtained for the GO/2HT intercalates.

2.5.3 Structural Reversibility of Graphite Oxide Intercalation Compounds with Temperature

The presence of order for the packing of long hydrocarbon chains within the interlayer space of GOICs is clearly confirmed by Differential Scanning Calorimetry (DSC) and X-ray diffraction measurements. For all GOICs, the DSC scans in **Fig. 2.19** show an irreversible first heating followed by reversible cooling and heating scans. For instance, for GO/2HT-L, the first heating scan shows an intense endothermic peak located at 42 °C, while the subsequent cooling and heating scans present exothermic and endothermic peaks at 25 °C and at 35 °C, respectively (**Fig. 2.19A**). An analogous behavior was observed for the GO/2HT/SAES intercalate, with main crystallization and melting peaks of the rotator phase being located at 86 °C and 92 °C, respectively (**Fig. 2.19C**).

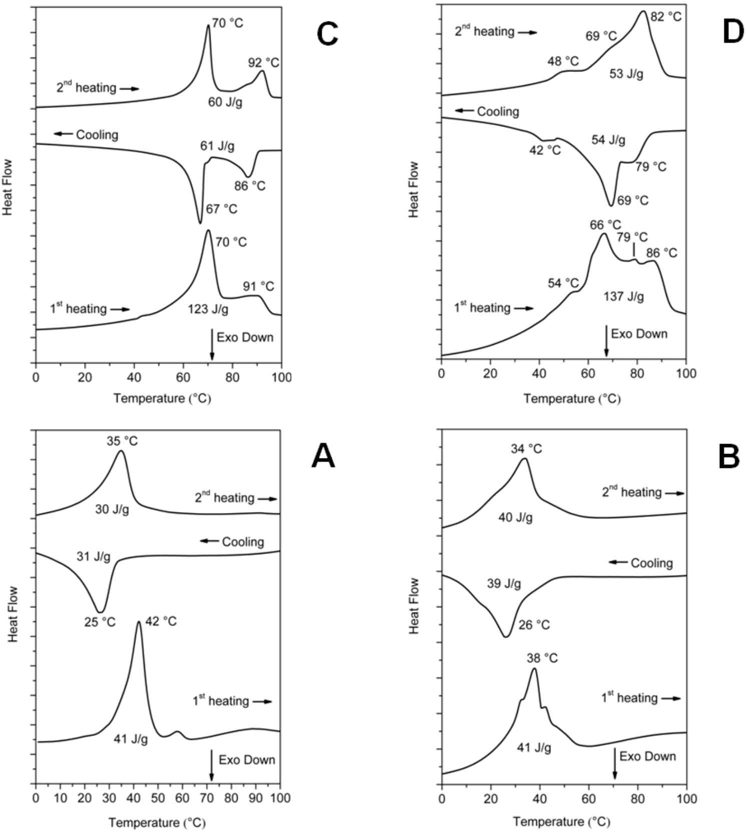

Fig. 2.19. (A) DSC scans of GOICs: (A) GO/2HT-L, (B) GO/2HT-H, (C) GO/2HT/SAES and (D) GO/2HT/GTS.

The X-ray diffraction patterns of the GO/2HT-L powder at room temperature, at 50 °C and at room temperature after treatment at 50 °C, have been reported in **Fig. 2.20**. The pattern at 50 °C shows that the endothermic phenomena of **Fig. 2.19A** lead to the disappearance of the diffraction peak at *d* = 0.42 nm and hence to the loss of the rotator order. Moreover, the pattern at 50 °C shows shifts of the 00ℓ reflections, indicating an increase of the interlayer spacing from 3.4 nm to 4.0 nm. The pattern at room temperature of GO/2HT-L, after annealing at 50 °C, shows a renewed reflection at *d* = 0.42 nm as well as 00ℓ peaks corresponding to the former narrower periodicity (3.4 nm). This demonstrates, as already observed for OCs in chapter I in Section I and for other layered materials intercalated with long hydrocarbon chain molecules,[77] that both loss of hexagonal rotator order and increase of the interlayer spacing are thermally reversible.

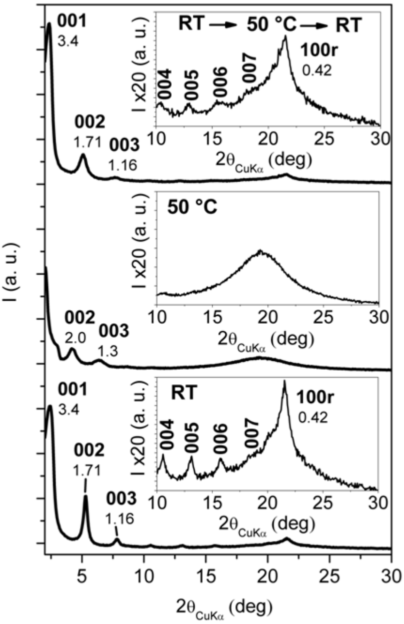

Fig. 2.20. X-ray diffraction patterns (Cu Kα) of GO/2HT-L at RT, 50 °C and at RT after thermal treatments up to 100 °C.

2.5.4 Structures of Graphite Oxide Intercalation Compounds

The X-ray diffraction patterns of the GO/2HT intercalates present a high similarity with those of ordered intercalate structures obtained by self-assembling of stearate ions in layered double hydrotalcite clay (LDH), in which C18 chains form bilayer structure in the vertical direction and a distorted hexagonal structure in the lateral direction, within the LDH interlayer space.[**78**] For the GO/2HT intercalates, analogous structures with inclined bilayers are here suggested (**Figs 2.21A-D**).

The tilt angle of the inclined bilayers of the GO/2HT-L intercalate can be evaluated as φ = 60°, on the basis of the basal spacing (d_{001} = 3.4 nm), by assuming that the thickness of the graphite oxide layer is close to 0.8 nm,[**58**] and that the length of two fully extended 2HT cations is 5.0 nm.[**79**]

For φ = 60°, the surface occupied by 8 graphite oxide unit cells (four are indicated as dashed red lines in **Fig. 2.21B**) is nearly equal to the surface occupied by a pseudo-cell of the rotator order, being parallel to the GO planes (indicated as thick black lines in **Fig. 2.21B**). Hence, the intercalate GO/2HT-L exhibits a C_{GO}/chains molar ratio of nearly 8/1, in good agreement with the molar ratio as independently evaluated by gravimetric measurements.

In the case of the GO/2HT-H intercalate, the tilt angle of the inclined bilayers can be evaluated as φ = 37°, on the basis of the basal spacing (d_{001} = 4.8 nm). In fact, the observed basal spacing is equal to the sum of the periodicity of GO (~ 0.8 nm) [**58**] and of the length of two fully extended 2HT cations (~ 5.0 nm).[**79**] The C_{GO}/chains molar ratio of the GO/2HT-H intercalate is nearly 6/1, in fact the surface occupied by 6 graphite oxide unit cells (four are indicated as dashed red lines in **Fig. 2.21D**) is nearly equal to the surface occupied by a pseudo-cell of the rotator order, being parallel to the GO planes (indicated as thick black lines in **Fig. 2.21D**). The results obtained by X-ray diffraction are in good agreement with the molar ratio as independently evaluated by gravimetric measurements.

For the more ordered GOICs, including both 2HT and SAES or GTS guests, on the basis of the large interlayer spacing (5.8 nm), analogous to those observed for cationic clays intercalated with ammonium salts with C18 tails (~ 6 nm),[**80**] a structure with perpendicular bilayers can be suggested (**Figs 2.21E-H**).

It is also worth adding that the patterns of GO/2HT/SAES and GO/2HT/GTS, both in **Fig. 2.17** and in **Fig. 2.18**, present a clear odd-even effect for the 00ℓ reflections, with definitely more intense odd reflections. This phenomenon can be easily rationalized on the basis of the model with perpendicular alkyl chains (**Figs 2.21E,G**). In fact, this model presents a minimum of atomic density in the middle of the graphitic interlayer space, due to non-bonded interactions between the tails of the long hydrocarbon chains, being clearly consistent with the reduced intensity of the 00ℓ reflections for ℓ even. A modest odd-even effect for the 00ℓ reflections is also exhibited by GO/2HT-H.

In the case of GO/2HT/SAES intercalates, the basal planes of the hexagonal cells of the rotator order (a_r = 0.42 nm, thick black lines), and of GO (a_g = 0.214 nm, dashed red lines) are compared in **Fig. 2.21F**. A good fit between the two hexagonal cells, with $a_r \approx 2a_g$ corresponding to four hexagonal cells of GO per one hexagonal cell of the rotator order, is apparent and clearly indicates a molar ratio of C_{GO}/chains =4/1. Again, the intercalate composition as derived by structural considerations well agrees with the composition as derived by gravimetric guest uptake. It is worth adding that the observed long range hexagonal rotator order of GO/2HT/SAES ($D_{100r} \approx$ 10 nm) is possibly associated with this good fit between the hexagonal cell bases of GO and of the hydrocarbon rotator order.

The GO/2HT/GTS intercalates exhibit layers of hydrocarbon chains in the interlayer space, for which the planes of the zig-zag backbones are parallel (see α and β layers in **Fig. 2.21H**). The planes of the zig-zag backbones of chains of adjacent layers along a_o = 0.76 nm are perpendicular (see **Figs 2.21G,H**). The surface occupied by 8 graphite oxide unit cells (four are indicated as dashed red lines in **Fig. 2.21H**) is nearly equal to the surface occupied by a orthorhombic cell of the hydrocarbon chains, indicated as thick black lines in **Fig. 2.21H**. The C_{GO}/chains molar ratio of the GO/2HT/GTS intercalates is nearly 4/1, as independently evaluated by gravimetric measurements.

The four structures of **Fig. 2.21** are also validated by density considerations. In fact, an evaluation of the density in the interlayer space, based on the compositions, provides a similar density for both intercalates (0.98 g/cm^3) not far from the value observed for crystalline polyethylene.

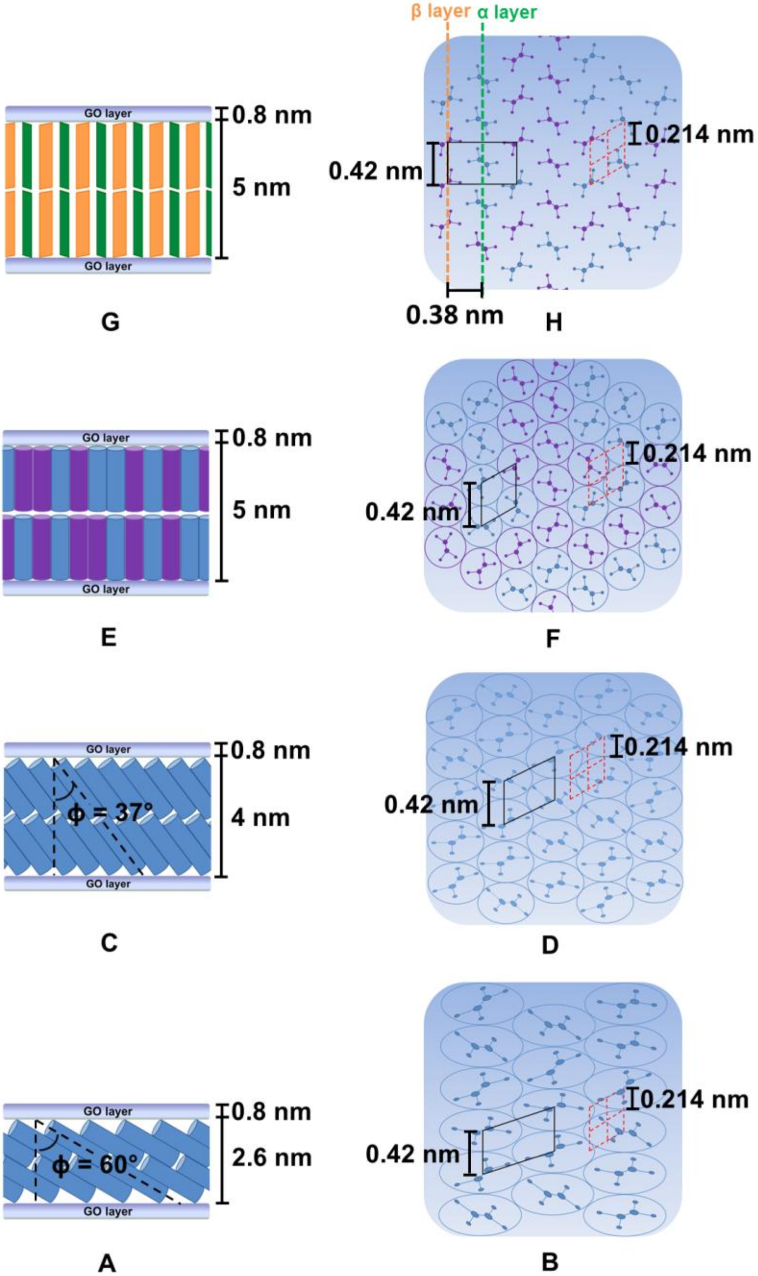

Fig. 2.21. Schematic presentation of the crystalline structures of the GO/2HT-L (A, B), GO/2HT-H (C, D), GO/2HT/SAES (E, F)

and GO/2HT/GTS (G, H). The cylinders of the lateral views (A, C, E) indicate hydrocarbon tails of the ammonium cation (blue) or of the additional polar guest (purple) in the hexagonal rotator order. For the top views (B, D, F), ellipses and circles indicate hydrocarbon chains inclined and perpendicular to the graphite oxide layers, respectively. The planes in G indicate zig-zag backbones of chains of adjacent α (green) and β (orange) layers. Moreover, dashed red lines show four adjacent hexagonal cells of GO, while thick black lines show the pseudo-cell on a section parallel to the GO layers in B and D, the hexagonal rotator cell in F and the orthorhombic cell in H. The definition of the alkyl chains tilt angle φ is shown in A and C.

In summary, GOIC with bulky guest molecules and with large interlayer spacings, also exhibiting a high crystalline order in the interlayer space, were obtained. In particular, intercalation in the interlayer space of ionic guest molecules with two long hydrocarbon tails leads to an increase of the interlayer spacing up to 4.8 nm, associated with a hexagonal rotator order of the intercalated hydrocarbon chains. The inclusion in the interlayer space of an additional guest molecule, being polar and also including one, two or three long hydrocarbon chains, leads to additional increase of the interlayer spacing (up to 5.8 nm) and of the crystalline order. In particular, in presence of a polar guest with two long hydrocarbon chains, the increase of crystalline order perpendicular to the graphite oxide layers is testified by at least eleven 00ℓ reflections with a correlation length increased up to $D = 42$ nm, while the increase of hexagonal rotator order of the hydrocarbon guest tails is shown by an increase of the correlation length (in the direction parallel to the graphite oxide layers) up to 10 nm. When the polar guest has three long hydrocarbon chains, an orthorhombic order of the intercalated hydrocarbon chains occurs.

The intercalate structures with d_{001} = 3.4 nm and 4.8 nm present bilayers of hydrocarbon chains being inclined ($\varphi = 60°$ and 37°), with C_{GO}/chains molar ratios of 8/1 and 6/1, respectively. The intercalate structures with $d_{001} = 5.8$ nm are characterized by bilayers of hydrocarbon chains being perpendicular to the GO layers, with a C_{GO}/chains molar ratio of 4/1. The molar ratios well agree with those obtained by gravimetric measurements.

The intercalation procedure adopted in this work leads thus to GOICs that seems to be suitable for having highly anisotropic GO layers in the rubber matrix, provided that the crystalline order of the GOICs can be overcome, for example by the mixing energy during the melt blending of GOICs with the rubber. Rubber/GOIC nanocomposites are discussed in chapter 4 in Section II.

2.6 Disordered Structures from Graphite Oxide: Chemically Modified Graphenes

Graphene, a one-atom-thick single layer of sp^2-bonded carbon atoms packed in a two dimensional honeycomb crystal lattice,[81] has attracted great interest, both in the scientific and industrial communities, due to its excellent mechanical, thermal and electrical properties.[82–84]

The first method for isolating graphene, based on micromechanical exfoliation of graphite using a scotch tape, was reported by Geim and Novoselov in 2004.[85]

In bottom-up processes, graphene is prepared by a variety of methods such as chemical vapor deposition,[86,87] arc discharge [88] and epitaxial growth on SiC.[89]

Nowadays, it is widely acknowledged that large scale production of single or few layers of chemically modified graphenes can be achieved by top-down processes of exfoliation and reduction of GO, through chemical or thermal treatments.[90,91] The term "chemically modified" is chosen because complete reduction of graphene oxide to graphene has not yet been observed.[92]

Hence, it is worth adding that GO is a versatile intermediate material that allows to prepare not only ordered intercalate structures, as just discussed in the paragraph above, but also disordered structures. In particular, starting from GO, chemically reduced graphite oxide (CRGO), exfoliated graphite oxide (eGO, also called graphene oxide) and reduced graphite oxide (rGO)/syndiotactic polystyrene (sPS) aerogels have been obtained by chemical reduction of GO aqueous dispersions, by mechanical treatments on GO powders and by solvo-thermal reduction of GO followed by supercritical CO_2 drying of rGO/sPS gels, respectively. These important results, discussed in the next paragraphs, have allowed us to obtain a complete control over the degree of order of the layered carbon structures we are able to prepare. Such disordered carbon materials, because of their high degree of exfoliation, could be suitable for applications as nanofillers in rubber nanocomposites.

2.6.1 Chemical Exfoliation of Graphite Oxide

Different methods currently exist for the reduction of GO to produce chemically reduced graphite oxide (CRGO). Chemical methods involve the treatment of colloidal GO dispersions with reducing chemicals such as hydrazine monohydrate,[93,94] dimethylhydrazine,[95,96] sodium borohydride,[97,98] hydroquinone,[99] ascorbic acid,[100–102] strongly alkaline solutions,[103] reducing sugars, such as glucose,[104] and sodium hydrosulfite.[105] All these methods allow obtaining only a partial reduction of the graphene oxide layers. In fact, after the reaction, each layer still contains few oxygen groups,[29] as represented in **Scheme 2.7**.

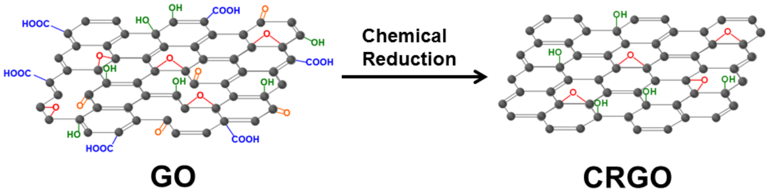

Scheme 2.7. Schematic representation of the partial reduction of the graphene oxide layers in CRGO, after chemical reduction of GO.

CRGO samples were prepared both from H-GO and L-GO, in presence of hydrazine monohydrate of ascorbic acid as reducing species, achieving the same results, without any significant structural change of the obtained CRGOs. Here, the results of the reduction of H-GO with hydrazine monohydrate are discussed.

The X-ray diffraction pattern of CRGO, reported in **Fig. 2.22**, shows broad 00ℓ peaks with interlayer distance $d_{002} = 0.362$ nm and well-defined 100 and 110 peaks. By comparing CRGO and the starting H-GO in **Fig. 2.22**, a large decrease of the out-of-plane correlation length ($D_\perp$ decreases from 5.4 nm down to 2.1 nm) and a large increase of the shape anisotropy ($D_\parallel$ / $D_\perp$ increases from 5.6 to 12.3) are clearly apparent. It is worth adding that after the oxidation procedure (H-GO in **Fig. 2.13**) as well as after the oxidation–reduction procedure (CRGO in **Fig. 2.22**) the 101 and 112 peaks are no longer observed, clearly indicating a complete loss of translational order between adiacent parallel layers and hence the occurrence of a turbostratic structure. Hence, **Figs 2.13** and **2.22** show that the overall oxidation–reduction procedure, when applied to anisotropic graphites, leads to aggregates of few piled graphene layers with long-range structural order only in the graphene planes. The oxidation–reduction procedure preserves the in-plane order of graphite, while dramatically increases the out-of-plane disorder, which becomes similar to that one of carbon black.

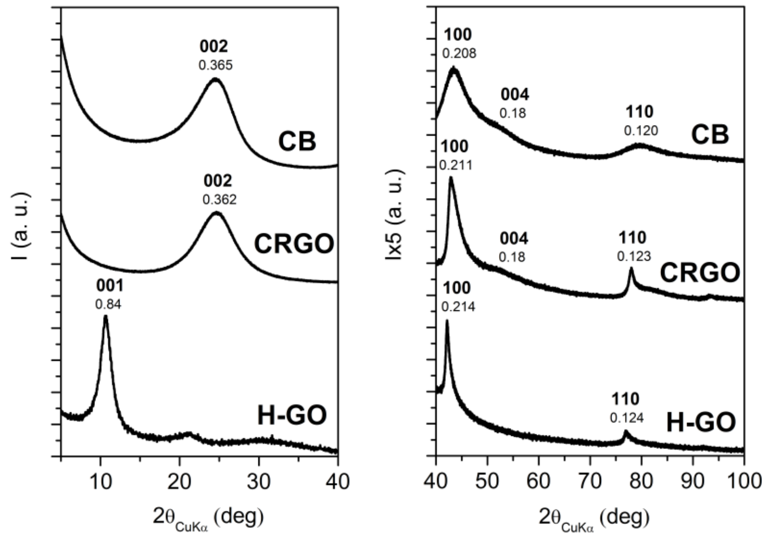

Fig. 2.22. X-ray diffraction patterns (Cu Kα) of the starting graphite oxide (H-GO) and of the derived CRGO, compared with the pattern of CB, also reported in Fig. 2.8 as F.

The FTIR spectrum of CRGO in **Fig. 2.23**, confirms the presence of oxygenated functional groups, mainly phenolic and epoxide, on the surface of the reduced layers.

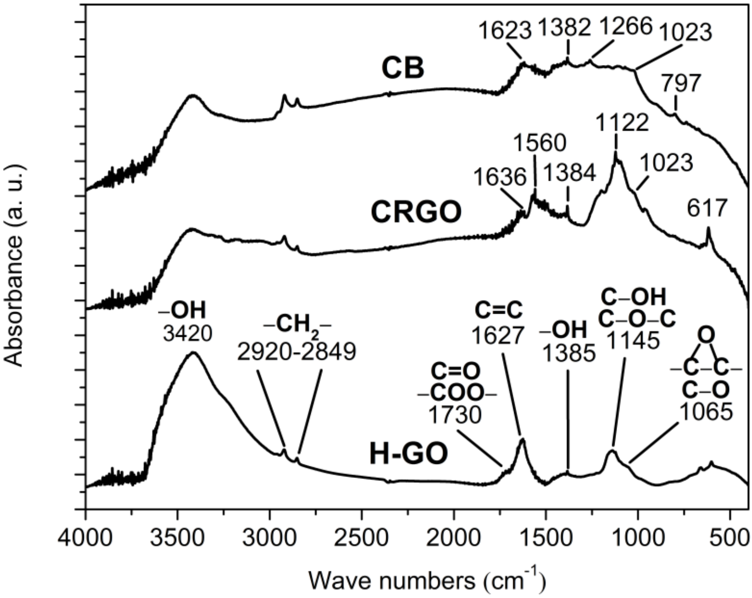

Fig. 2.23. FTIR spectra of the starting graphite oxide (H-GO) and of the derived CRGO, compared with the spectrum of CB.

The TGA and elemental analysis of the samples of **Fig. 2.22**, reported in **Fig. 2.24** and **Table 2.3**, indicate for CRGO the presence of large amount of oxygen (C/O = 4.4), which is more than five times higher than for standard carbon black (CB).

The surface area of CRGO (S_{BET} = 46.8 m^2/g), evaluated from the BET measurements reported in **Table 2.3**, strongly increases during the chemical reduction of H-GO (S_{BET} = 1.1 m^2/g) and becomes similar to that one of CB (S_{BET} = 57.2 m^2/g), confirming the high degree of exfoliation of CRGO particles.

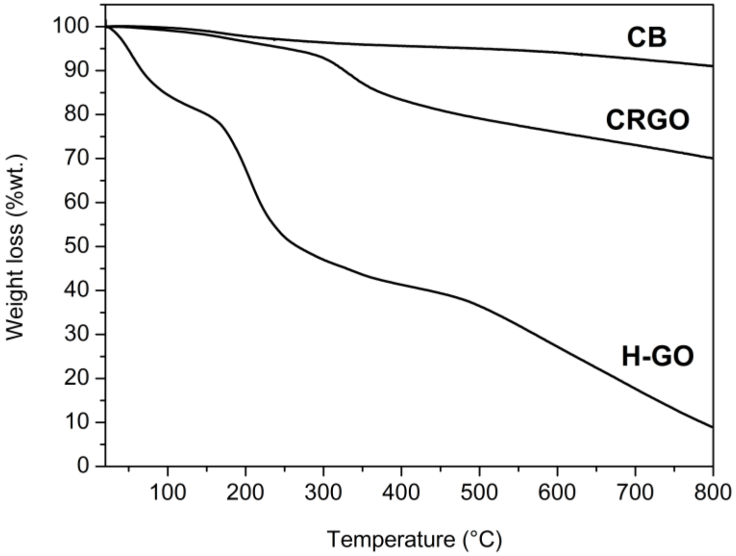

Fig. 2.24. TGA curves in N_2 of the starting graphite oxide (H-GO) and of the derived CRGO, compared with the curve of CB.

Table 2.3. Results of elemental analysis on the starting graphite oxide (H-GO) and of the derived CRGO, compared with CB.[a]

Sample	Surface area (m^2/g)	Elemental composition (%wt.)					
		C	H	N	O	S	C/O
H-GO	1.1	59.1	1.4	0.1	35	4.4	1.6
CRGO	46.8	79.9	0.2	2.7	17.2	0.0	4.6
CB	57.2	96.2	0.5	0.1	3.2	0.0	30.1

[a] Elemental composition of the anhydrous samples: water contents of nearly 20 %wt., 2 %wt. and 1 %wt. are evaluated by TGA for H-GO, CRGO and CB, respectively.

Additional informations about the structural changes during the whole oxidation-reduction process from G to CRGO are provided by the raman characterization of G, H-GO, CRGO and CB reported in **Fig. 2.25**. The Raman characterization was performed by the group of Dr. Pellegrino Musto at the CNR, Institute of Chemistry and Technology of Polymers (ICTP) Pozzuoli.

The main features of the Raman spectrum of a perfect graphite are the G-band at ~ 1580 cm^{-1} and the 2D-band at ~ 2700 cm^{-1}.[**106**] The Raman spectrum of G also present a pronounced D-band at 1325 cm^{-1} , a shoulder of the G-band at 1592 cm^{-1}, called the D'-band and a combination (D+G) band at 2909 cm^{-1}, which indicate the presence of structural disorder.[**107**] In the Raman spectrum of GO, D-band becomes more intense and both D and G-bands are broader ($FWHM_D$ increases from 55.5 cm^{-1} to 97.7 cm^{-1}) because of reduction in size of the in-plane sp^2-carbon domains, caused by chemical oxygen functions in the graphitic layers.[**108**] It is worth adding that the (D+G) band becomes more intense than the close 2D band and that in this region the spectrum becomes strictly similar to that one of carbon black (**Fig. 2.25**, upper curve). The CRGO Raman spectrum presents D and G-bands being narrower than for the GO samples and (e.g., $FWHM_D$ decreases from 97.7 cm^{-1} to 60.2 cm^{-1}) and close to those of the starting G sample (see **Table 2.4**). The D'-band reappears at 1597 cm^{-1}, as a shoulder of the G-band while the (D + G) band is more intense than in the case of graphite G.

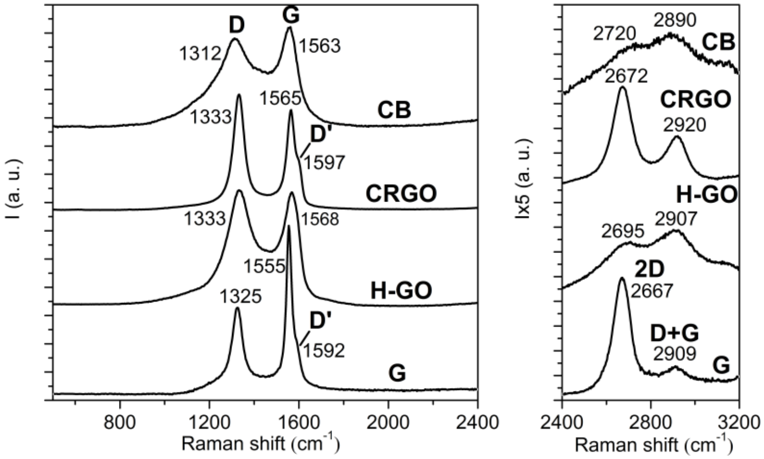

Fig. 2.25. Raman spectra of the starting high surface area graphite (G), the derived graphite oxide (H-GO), the chemically reduced graphite oxide (CRGO) and the carbon black (CB) samples.

Table 2.4. Full width at half maximum of the D-band of the Raman spectra of Fig. 2.24.

Sample	FWHM_D (cm^{-1})
G	55.5
H-GO	97.7
CRGO	60.2
CB	118.8

2.6.2 Mechanical Exfoliation of Graphite Oxide

The mechanical exfoliation of GO by ball-milling is a simple but effective technique to produce exfoliated graphite oxide (eGO, also called graphene oxide) in the bulk state (see **Scheme 2.8**).

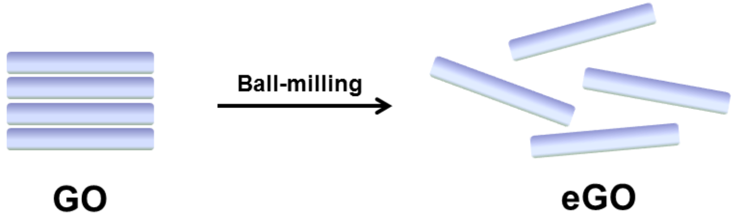

Scheme 2.8. Schematic representation of the exfoliation of GO by ball-milling.

The large increase of the interlayer spacing, from 0.34 nm up to nearly 0.8 nm, during the oxidation process of graphite and the disordered arrangement of the functional oxidized groups on the layer surfaces of GO lead to weak interlayer attractive forces, making easy the GO exfoliation by simple mechanical processes.

Exfoliated GO samples were prepared according the procedure in paragraph 8.11 in Section IV, starting from L-GO, and the related X-ray diffraction patterns are shown in **Fig. 2.26**.

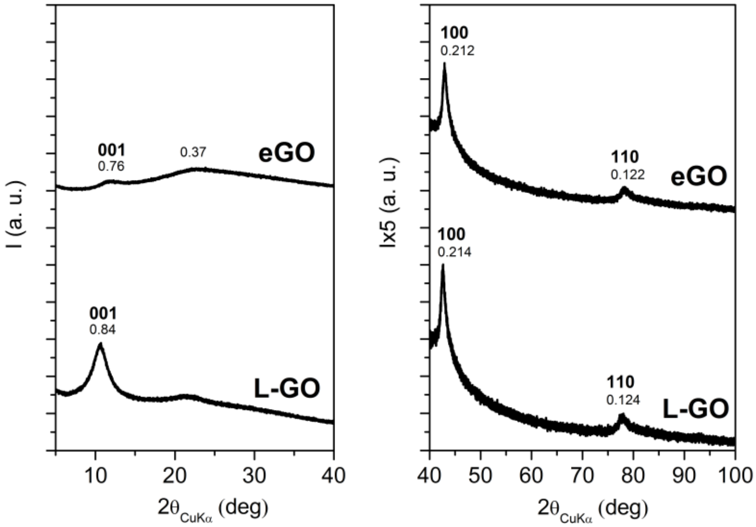

Fig. 2.26. X-ray diffraction patterns (Cu Kα) of the starting graphite oxide (L-GO) and of the derived eGO after ball-milling.

The pattern of eGO shows, beside the maintenance of the 100 and 110 reflections, a very broad intense halo, centered at $d =$ 0.37 nm with a correlation length of about 1 nm, indicating the presence of a large fraction of essentially exfoliated GO.[**109**] The weak reflection with d = 0.76 nm and $D_{\perp}$ ≈ 2.5 nm can be interpreted as the 001 reflection of unexfoliated GO, occurring in an amount lower than 10 %wt.

The bands of carboxyl, phenolic and epoxide groups in the FTIR spectrum of eGO appear enhanced in intensity with respect to the same bands in the L-GO FTIR spectrum in **Fig. 2.27**. This result could be attributed to the greater exposure of the oxygenated functional groups on the exfoliated layers of eGO.

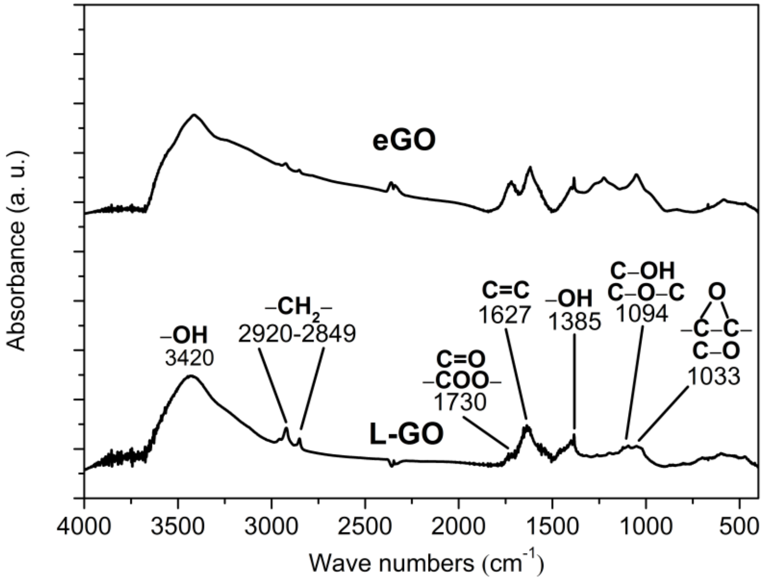

Fig. 2.27. FTIR spectra of the starting graphite oxide (L-GO) and of the derived eGO after ball-milling.

Similar considerations can be made by comparing the TGA of L-GO and eGO in **Fig. 2.28**. In fact, above 150 °C, the oxygenated functional groups of eGO decompose earlier with respect to the same groups of L-GO, and, again, this phenomenon could be attributed to a greater exposure of the groups on the exfoliated layers of eGO.

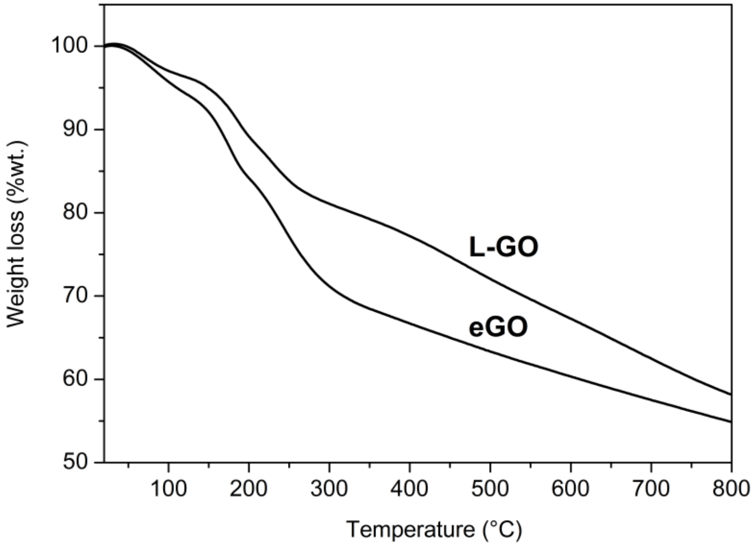

Fig. 2.28. TGA curves in N_2 of the starting graphite oxide (L-GO) and of the derived eGO after ball-milling.

The results of the elemental analysis and the BET measurements, reported in **Table 2.5**, show that L-GO and eGO samples have similar C/O ratios and largely different surface areas, 0.8 m^2/g and 4.6 m^2/g, respectively, definitely lower than the value for G (308 m^2/g).

Table 2.5. Results of elemental analysis on the starting graphite oxide (L-GO) and of the derived eGO after ball-milling.[a]

Sample	Surface area (m^2/g)	Elemental composition (%wt.)					
		C	H	N	O	S	C/O
L-GO	0.8	63.7	0.6	0.1	33.7	1.9	1.9
eGO	4.2	66.1	0.5	0.1	31.4	1.9	2.1

[a] Elemental composition of the anhydrous samples: water contents of nearly 5 %wt. and 6 %wt. are evaluated by TGA for L-GO and eGO, respectively.

The SEM images of L-GO in **Figs 2.29A-B** indicate that the oxidation of G leads to dense aggregates of graphene oxide sheets (surface area largely decreases from 308 m^2/g to 0.8 m^2/g). The mechanical exfoliation of L-GO by ball-milling strongly reduced the dimension of the particles, providing sub-micrometric aggregates of thin crumpled graphene oxide sheets, stacked in a disordered manner (**Figs 2.29C-D**).

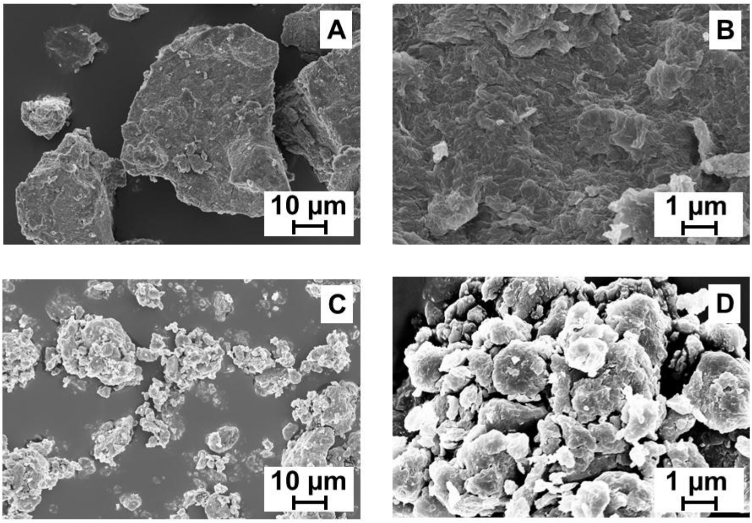

Fig. 2.29. SEM images of: (A,B) L-GO and (C,D) eGO at different magnifications.

The high degree of exfoliation of eGO is also confirmed by the TEM images in **Fig. 2.30**. Particularly, in **Fig. 2.30B** single graphene oxide layers are clearly visible.

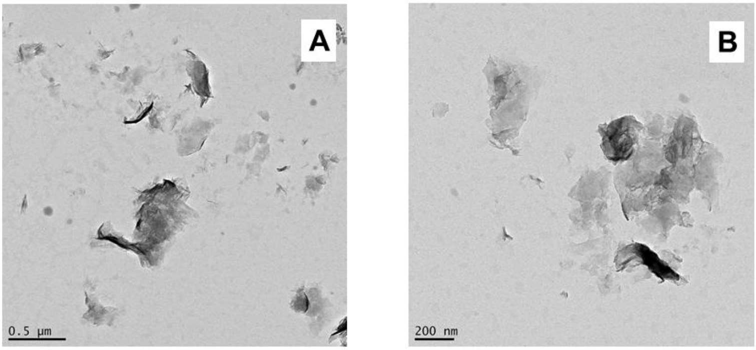

Fig. 2.30. TEM images of eGO at different magnifications: (A) 0.5 μm and (B) 200 nm.

2.6.3 Syndiotactic Polystyrene Aerogels with Reduced Graphite Oxide

Monolithic sPS/reduced GO (rGO) aerogels were prepared for a very broad polymer/rGO composition range, according to the procedure reported in paragraph 8.13 in Section IV. The preparation and the characterization of polymer/rGO aerogels were performed in collaboration with Dr. Simona Longo of the Department of Chemistry and Biology of the University of Salerno.

These interesting materials, not only could be helpful to an easier handling of exfoliated rGO, removing the risks connected with inhalable nanoparticles, but also, due to their thermoplastic nature, could be used as graphene "masterbatches" for composite processing,[**110–112**] as already mentioned for monolithic sPS/exfoliated clay aerogels (see paragraph 1.3).

Homogenous rGO dispersions in an organic solvent (dichlorobenzene, DCB) were prepared by a solvo-thermal reduction procedure,[**113**] described in paragraph 8.12 in Section IV i.e. by sonication at 100 °C of L-GO, as shown in **Fig. 2.31**.

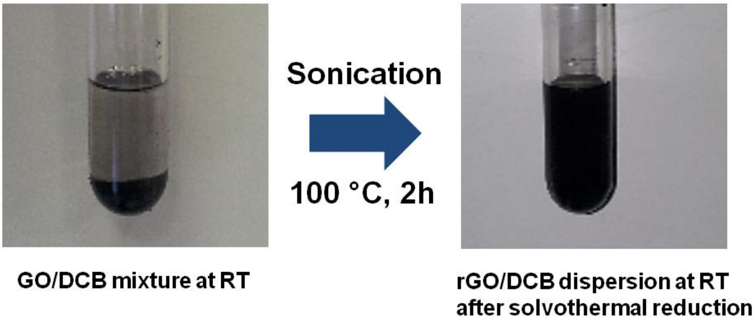

GO/DCB mixture at RT

rGO/DCB dispersion at RT after solvothermal reduction

Fig. 2.31. Solvothermal reduction route of L-GO for preparation of rGO dispersions in DCB.

The X-ray diffraction pattern of rGO powder, after extraction of rGO/DCB dispersion with supercritical carbon dioxide, is shown in **Fig. 2.32** and exhibits a 002 reflection at 0.35 nm, with a correlation length of roughly 3.5 nm.

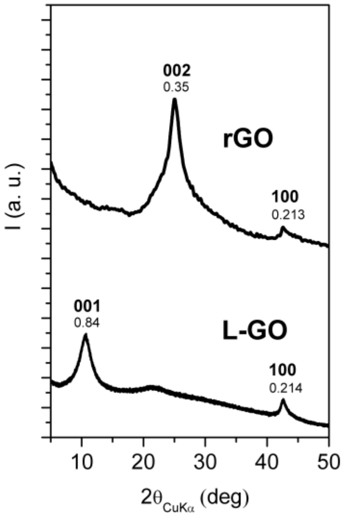

Fig. 2.32. X-ray diffraction (Cu Kα) patterns in the 2θ range 5-50° of L-GO and reduced graphite oxide (rGO), as obtained by solvothermal reduction of graphite oxide dispersions in DCB and supercritical-CO_2 removal of DCB.

sPS/rGO gels were prepared by dissolution of sPS in rGO dispersions, followed by cooling to room temperature of the hot solution. The overall amount of polymer and rGO in the gels was generally fixed to 10 %wt. Monolithic aerogels, which essentially present the same size and shape of the precursor gels and hence a porosity close to 90%, are obtained by extracting with supercritical carbon dioxide all the prepared sPS/rGO gels (**Fig. 2.33**). A macroscopic phase separation of the black rGO aggregates is only obtained for sPS/rGO weight ratios higher than 70/30.

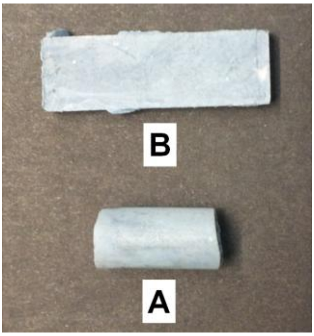

Fig. 2.33. Photographs of homogenous monolithic sPS/rGO 80/20 aerogels, with porosity *P*= 90%, as prepared with cylindrical (diameter of 7 mm) (A) and plate (length 15 mm, width 10 mm and thickness 2 mm) (B) molds. The shown aerogels essentially present the same size and shape of the precursor gels.

A peculiar feature of the sPS/rGO aerogels is their uniform light blue color, even with high rGO content. All known composites containing carbonaceous fillers are black in color and the unique color of sPS/rGO aerogels could be attributed to the highly porous morphology of the sPS aerogels (see **Fig. 1.14**).

The X-ray diffraction (Cu Kα) patterns of the sPS/rGO aerogels, with porosity of 90% and presenting different polymer/rGO weight ratios are shown in **Fig. 2.34**. The patterns show the maintenance of the diffraction peaks of the nanoporous-crystalline δ form of sPS, for the entire composition range. In this respect, it is worth adding that the degree of crystallinity of the polymer increases going from the pure sPS aerogel to the 95/5 aerogel (from nearly 45% up to 55%), suggesting a nucleating effect of graphitic layers on the crystalline δ form. The in-plane 100 peak of rGO clearly appears for the 50/50 aerogel (**Fig. 2.34E**), while only appears as a shoulder for lower rGO contents.

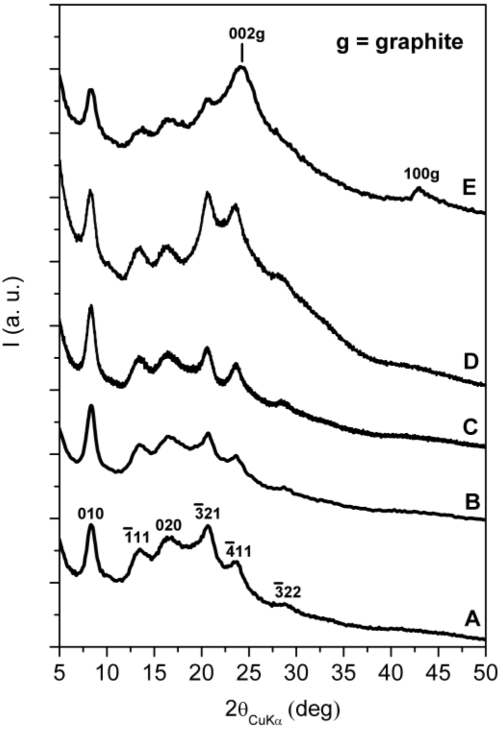

Fig. 2.34. X-ray diffraction (Cu Kα) patterns in the 2θ range 5-50° of sPS aerogels with rGO, as obtained from gels with a solvent content of 90 %wt. and presenting different polymer/rGO weight ratios: (A) 100/0; (B) 95/5; (C) 80/20; (D) 70/30; (E) 50/50. The Miller indexes of the main reflections of the nanoporous-crystalline δ form of sPS are indicated in A. The symbol **g** indicates reflections relative to the graphite oxide planes.

SEM images of the sPS/rGO aerogels of different weight ratios of **Fig. 2.34** are shown in **Fig. 2.35**. For the polymer rich aerogels (**Figs 2.35A–C**, rGO content up to 30 %wt.) the images are dominated by the typical fibrillar morphology (with diameters of roughly 50–100 nm) of the δ form sPS aerogels. The rGO component is clearly apparent, mainly as hexagonal platelets, only for the 50/50 sPS/rGO aerogels (**Fig. 2.35D**). The exfoliation state of rGO is preserved by preparing polymer/rGO aerogels up to 30 %wt. of rGO content.

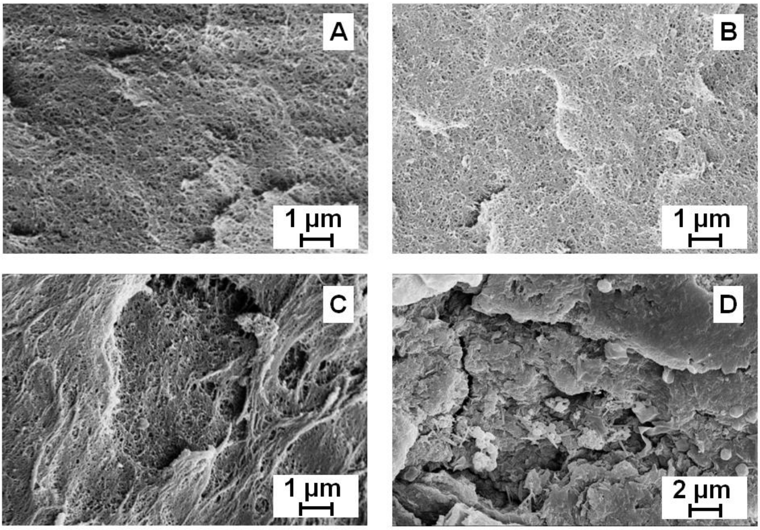

Fig. 2.35. SEM images of sPS/rGO aerogels with weight ratios 95/5 (A), 80/20 (B), 70/30 (C), 50/50 (D).

The Raman imaging analysis on a sample of sPS/rGO aerogel 80/20 was performed by the group of Dr. Pellegrino Musto at the CNR, Institute of Chemistry and Technology of Polymers (ICTP) Pozzuoli and is reported in **Fig. 2.36**.

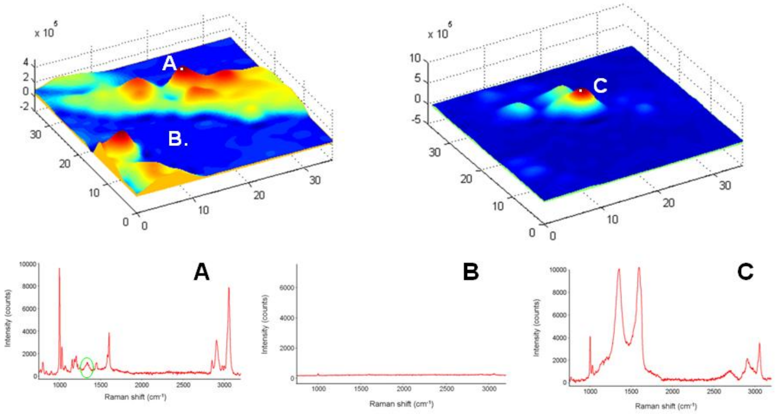

Fig. 2.36. Raman imaging analysis of different zones of a sample of sPS/rGO aerogel 80/20.

The Raman spectrum A was obtained by considering the area under the peak of the polymer at 3060 cm^{-1} and shows the prevalence of the polymer phase with a low concentration of rGO (peak at 1345 cm^{-1}) dispersed in the polymeric matrix. The Raman spectrum B shows the presence of an empty pore, while the Raman spectrum C, obtained by considering the area under the peak of rGO at 1345 cm^{-1}, shows the prevalence of the rGO phase and the peaks of the polymer are negligible. The same results were obtained also by considering different zones of the sample. So, at the microscopic level, rGO particles aggregate in small domains, but the polymer phase always contains dispersed rGO particles. This is an interesting result, taking in account the high content of rGO with respect to the polymer.

Relevant information relative to the sPS/rGO aerogels also comes from surface area evaluations, as conducted by the BET method, in **Table 2.6**.

Table 2.6. Total surface area (S_{BET}) of the starting graphite, graphite oxide, reduced graphite oxide and of aerogels with porosity P = 90%, exhibiting 80/20, 70/30 and 50/50 polymer/rGO weight ratio.[a]

Sample	S_{BET}[a] ($m^2\ g^{-1}$)
Graphite	308
Graphite oxide	0.8
Reduced graphite oxide (scrCO_2 treated)	2.1
sPS/rGO 80/20 aerogel	289
Aerogel δ sPS	312

[a]Total area evaluated following the BET model in the standard $0.05<P/P_0<0.3$ pressure range.

The sPS/rGO 80/20 aerogels present values of S_{BET} (289 $m^2\ g^{-1}$) not far from those observed for pure sPS aerogels (312 $m^2\ g^{-1}$). As already commented for sPS/exfoliated-OC aerogels, rGO not only does not disturb the formation of the nanoporous crystalline phase but also does not alter the amorphous aerogel porosity.

References

[1] B. Kwiecińska, H. I. Petersen. *Int. J. Coal Geol.* **2004**, *57,* 99–116.

[2] A. W. Hull. *Phys. Rev.* **1917**, *10,* 661–696.

[3] J. D. Bernal. *Proc. R. Soc. A* **1924**, *106,* 749–773.

[4] M. Inagaki and F. Kang, *Carbon Materials Science and Engineering: from Fundamentals to Applications,* Chapter 2, *36,* **2006**.

[5] B. E. Warren. *Phys. Rev.* **1941**, *59,* 693–698.

[6] Z. Q. Li, C. J. Lu, Z. P. Xia, Y. Zhou, Z. Luo. *Carbon* **2007**, *45,* 1686–1695.

[7] A. Milev, M. Wilson, G. S. Kamali Kannangara, N. Tran. *Mater. Chem. Phys.* **2008**, *111,* 346–350.

[8] J. Zhao, L. Yang, F. Li, R. Yu, C. Jin. *Carbon* **2009**, *47,* 744–751.

[9] O. J. Guentert. *J. Chem. Phys.* **1962**, *37,* 884–891.

[10] R. E. Franklin. *Acta Crystallogr.* **1950**, *3,* 107–121.

[11] P. J. F. Harris. *Interisciplinary Science Reviews* **2001**, *26,* 204–210.

[12] M. J. Wang, C. A. Gray, S. A. Reznek, K. Mahmud, Y. Kutsovsky, *Kirk-Othmer Encyclopedia of Chemical Technology,* **2003**.

[13] S. Babu, M. S. Seehr. *Carbon* **1996**, *34,* 1259–1265.

[14] O. J. Guentert, C. A. Klein. *Appl. Phys. Lett.* **1963**, *2,* 125–127.

[15] C. N. Hooker, A. R. Ubbelohde, D. A. Young. *Proc. R. Soc. London A* **1965**, *284,* 17–31.

[16] A. Celzard, J. F. Marêché, G. Furdin, S. Puricelli. *J. Phys. D: Appl. Phys.* **2000**, *33,* 3094–3101.

[17] M. Cardinali, L. Valentini, J. M. Kenny. *J. Phys. Chem. C* **2011**, *115,* 16652–16656.

[18] H. Fujimoto. *Carbon* **2003**, *41,* 1585–1592.

[19] B. C. Brodie. *Philos. Trans. R. Soc. London* **1859**, *149,* 249–259.

[20] L. Staudenmaier. *Ber. Dtsch. Chem. Ges.* **1898**, *31,* 1481–1487.

[21] W. S. Hummers, R. E. Offeman. *J. Am. Chem. Soc.* **1958**, *80,* 1339.

[22] D. R. Dreyer, R. S. Ruoff, C. W. Bielawski. *Angew. Chem. Int. Ed.* **2010**, *49,* 9336–9344.

[23] H. He, J. Klinowski, M. Forster, A. Lerf. *Chem. Phys. Lett.* **1998**, *287,* 53–56.

[24] J. Luo, L. J. Cote, V. C. Tung, A. T. Tan, P. E. Goins, J. Wu, J. Huang. *J. Am. Chem. Soc.* **2010**, *132,* 17667–17669.

[25] D. R. Dreyer, C. W. Bielawski. *Adv. Funct. Mater.* **2012**, *12,* 3247–3253;

[26] A. D. Todd, C. W. Bielawski. *Catal. Sci. Technol.* **2013**, *3,*135–139;

[27] D. R. Dreyer, S. Murali, Y. Zhu, R. S. Ruoff, C. W. Bielawski. *J. Mater. Chem.* **2011**, *21,* 3443–3447.

[28] Y. Si, E. T. Samulski. *Nano Lett.* **2008**, *8,* 1679–1682.

[29] K. Haubner, J. Morawski, P. Olk, L. M. Eng, C. Ziegler, B. Adolphi, E. Jaehne. *ChemPhysChem* **2010**, *10,* 2131–2139.

[30] D. Chen, H. Zhu, T. Liu. *Appl. Mater. Interface* **2010**, *2,* 3702−3708.

[31] Z. J. Fan, W. Kai, J. Yan, T. Wie, L. J. Zhi, J. Feng, Y. M. Ren, L. P. Song, F. Wei. *ACS Nano* **2011**, *5,* 191−198.

[32] S. Zhang, Y. Shao, H. Liao, M. H. Engelhard, G. Yin, Y. Lin. *ACS Nano* **2011**, *5,* 1785−1791.

[33] J. Wang, X. Wang, C. Xu, M. Zhang, X. Shang. *Polym. Int.***2011**, *60,* 816−822.

[34] H. Kim, S. Kobayashi, M. A. AbdurRahim, M. J. Zhang, A. Khusainova, M. A. Hillmyer. *Polymer* **2011**, *52,* 1837−1846.

[35] S. Ansari, E. P. Giannelis. *J. Polym. Sci.: Part B* **2009**, *47,* 888−889.

[36] H. P. Boehm, R. Setton, E. Stumpp. *Pure Appl. Chem.* **1994**, *66,* 1893–1901.

[37] S. Dresselhaus, G. Dresselhaus. *Adv. Phys.* **2002**, *51,* 1–186.

[38] J. O. Besenhard**.** *Carbon* **1976**, *14,* 111–115.

[39] C. Herold, A. Herold, P. Lagrange P. *Solid State Sci.* **2004**, *6,* 125–138.

[40] W. Q. Deng, X. Xu, W. A. Goddard. *Phys. Rev. Lett.* **2004**, *92,* 166103.

[41] T. Quang, P. Pokharel, G. S. Song, D. S. Lee. *J. Nanosci. Nanotech.* **2012**, *12,* 4305–4308.

[42] J. Li, L. Vaisman, G. Marom, J. K. Kim. *Carbon* **2007**, *45,* 744–750.

[43] S. Tongay, J. Hwang, D. B. Tanner, H. K. Pal, D. Maslov, A. F.

Hebard. *Phys. Rev. B* **2010**, *81*, 115428.

[44] W. Yan, M. M. Lerner. *Carbon* **2004**, *42*, 2981–2987.

[45] W. Katinonkul, M. M. Lerner. *Carbon* **2007**, *45*, 2672–2677.

[46] T. Maluangnont, G. T. Bui, B. A. Huntington, M. M. Lerner. *Chem. Mater.* **2011**, *23*, 1091–1095.

[47] W. Rüdorff, E. Schulze. Z. *Anorg. Allg. Chem.* **1954**, *277*,156–171.

[48] G. Cao, V. M. Lynch, L. N. Yacullo. *Chem. Mater.* **1993**, *5*, 1000–1006.

[49] J. Lu, T. Paliwala, S. C. Lim, C. Yu, T. Y. Niu, A. J. Jacobson. *Inorg. Chem.* **1997**, *36*, 923–929.

[50] G. J. McManus, J. J. Perry, M. Perry, B. D. Wagner, M. J. Zaworotko. *J. Am. Chem. Soc.* **2007**, *129*, 9094–9101.

[51] P. Iannelli, P. Damman, M. Dosière, J. F. Moulin. *Macromolecules* **1999**, *32*, 2293–2300.

[52] A. Matsumoto, S. Oshita, D. Fujioka. *J. Am. Chem. Soc.* **2002**, *124*, 13749–13756.

[53] V. Petraccone, O. Tarallo, V. Venditto, G. Guerra. *Macromolecules* **2005**, *38*, 6965–6971.

[54] O. Tarallo, V. Petraccone, V. Venditto, G. Guerra. *Polymer* **2006**, *47*, 2402–2410.

[55] A. R. Albunia, C. D' Aniello, G. Guerra. *CrystEngComm* **2010**, *12*, 3942–3949.

[56] T. Shimogaki, S. Oshita, A. Matsumoto. *Macromol. Chem. Phys.* **2011**, *212*, 1767–1777.

[57] A. R. Albunia, P. Rizzo, M. Coppola, M. De Pascale, G. Guerra. *Polymer* **2012**, 53, 2727–2735.

[58] Y. Matsuo, T. Niwa, Y. Sugie. *Carbon* **1999**, *37*, 897–901.

[59] I. Dékány, R. Krüger-Grasser, A. Weiss. *Colloid Polym. Sci.* **1998**, *276*, 570–576.

[60] Y. Matsuo, K. Hatase, Y. Sugie. *Chem. Lett.* **1999**, 1109–1110.

[61] Z. Liu, Z. M. Wang, X. Yang, K. Ooi. *Langmuir* **2002**, *18*,

4926–4932.

[62] Y. Matsuo, T. Miyabe, T. Fukutsuka, Y. Sugie. *Carbon* **2007**, *45*, 1005–1012.

[63] S. Stankovich, D. A. Dikin, O. C. Compton, G. H. B. Dommet, R. S. Ruoff, S. B. T. Nguyen. *Chem. Mater.* **2010**, *22*, 4153–4157.

[64] K. Zhang, L. Mao, L. L. Zhang, H. S. O. Chan, X. S. Zhao, J. Wu. *J. Mater. Chem.* **2011**, *21*, 7302–7307.

[65] M. Acik, D. R. Dreyer, C. W. Bielawski, Y. J. Chabal. *J. Phys. Chem. C* **2012**, *116*, 7867−7873.

[66] T. Cassagneau, F. Guérin, J. H. Fendler. *Langmuir* **2000**, *16*, 7318−7324.

[67] R. Bissessur, S. F. Scully. *Solid State Ionics* **2007**, *178*, 877–882.

[68] H. Bai, C. Li, X. Wang, G. Shi. *J. Phys. Chem. C* **2011**, *115*, 5545–5551.

[69] T. N. Blanton, D. Majumda. *Powder Diffr.* **2012**, 27, 104–107.

[70] S. Y. Chazhengina, E. N. Kotelnikova, I. V. Filippova, S. K. Filatov. *J. Mol. Struct.* **2003**, *647*, 243–257.

[71] M. Dirand, Z. Achour-Boudjema. *J. Mol. Struct.* **1996**, *375*, 243–248.

[72] V. Chevallier, D. Petitjean, M. Bouroukba, M. Dirand. *Polymer* **1999**, *40*, 2129–2137.

[73] D. Fu, Y. Liu, Y. Su, G. Liu, D. Wang. *J. Phys. Chem. B* **2011**, *115*, 4632–4638.

[74] D. Fu, Y. Liu, G. Liu, Y. Su, D. Wang. *Phys. Chem. Chem. Phys.* **2011**, *13*, 15031–15036.

[75] G. Ungar, N. Mašić. J. Phys. Chem. **1985**, *89*, 1036–1042.

[76] C. J. Kim, W. Khan, S. Y. Park. *Chem. Phys. Lett.* **2011**, *511*, 110–115.

[77] Y. Ide, M. Ogawa. *J. Colloid Interface Sci.* **2006**, *296*, 141–149.

[78] T. Itoh, N. Ohta, T. Shichi, T. Yui, K. Takagi. *Langmuir*

2003, *19,* 9120–9126.

[79] M. A. Osman, M. Ernst, B. H. Meier, U. W. Suter. *J. Phys. Chem. B* **2002**, *106,* 653–662.

[80] M. Galimberti, S. Giudice, V. Cipolletti, G. Guerra. *Polym. Adv. Tech.* **2010**, *21,* 679–684.

[81] A. K. Geim, K. S. Novoselov. *Nat. Mater.* **2007**, *6,* 183–191.

[82] C. Lee, X. Wei, J. W. Kysar, J. Hone. *Science* **2008**, *321,* 385–388.

[83] A. A. Balandin, S. Ghosh, W. Bao, I. Calizo, D. Teweldebrhan, F. Miao, C. N. Lau. *Nano Lett.* **2008**, *8,* 902–907.

[84] X. Du, I. Skachko, A. Barker, E. Y. Andrei. *Nature Nanotechnol.* **2008**, *3,* 491–495.

[85] K. S. Novoselov, A. K. Geim, S. V. Morozov, D. Jiang, Y. Zhang, S. V. Dubonos, I. V. Grigorieva, A. A. Firsov. *Science* **2004**, *306,* 666–669.

[86] S. J. Chae, F. Günes, K. K. Kim, E. S. Kim, G. H. Han, S. M. Kim, H. J. Shin, S. M. Yoon, J. Y. Choi, M. H. Park, C. W. Yang, D. Pribat, Y. H. Lee. *Adv. Mater.* **2009**, *21,* 2328–2333.

[87] X. Wang, H. You, F. Liu, M. Li, L. Wan, S. Li, Q. Li, Y. Xu, R. Tian, Z. Yu, D. Xiang, J. Cheng. *Chem. Vapor Deposition* **2009**, *15,* 53–56.

[88] N. Li, Z. Wang, K. Zhao, Z. Shi, Z. Gu, S. Xu. *Carbon* **2009**, *48,* 255–259.

[89] C. Berger, Z. Song, X. Li, X. Wu, N. Brown, C. Naud, D. Mayou, T. Li, J. Hass, A. N. Marchenkov, E. H. Conrad, P. N. First, W. A. de Heer. *Science* **2006**, *312,* 1191–1196.

[90] S. Park, R. S. Ruoff. *Nat. Nanotech.* **2009**, *5,* 217–224.

[91] R. Sengupta, M. Bhattacharya, S. Bandyopadhyay, A. K. Bhowmick. *Prog. Polym. Sci.* **2011**, *36,* 638–670.

[92] H. Kim, A. A. Abdala, C. W. Macosko. *Macromol.* **2010**, *43,* 6515–6530.

[93] S. Stankovich, D. A. Dikin, R. D. Piner, K. A. Kohlhaas, A. Kleinhammes, Y. Jia, Y. Wu, S. T. Nguyen, R. S. Ruoff. *Carbon*

2007, *45,* 1558–1565.

[94] S. Park, J. An, J. R. Potts, A. Velamakanni, S. Murali, R. S. Ruoff. *Carbon* **2011**, *49,* 3019–3023.

[95] S. Stankovich, D. A. Dikin, G. H. B. Dommett, K. M. Kohlhaas, E. J. Zimney, E. A. Stach, R. D. Piner, S. T. Nguyen, R. S. Ruoff. *Nature* **2006**, *442,* 282–286.

[96] G. Eda, G. Fanchini, M. Chhowalla. *Nat. Nanotech.* **2008**, *3,* 270–274.

[97] H. J. Shin, K. K. Kim, A. Benayad, S. M. Yoon, H. K. Park, I. S. Jung, M. H. Jin, H. K. Jeong, J. M. Kim, J. Y. Choi, Y. H. Lee. *Adv. Funct. Mater.* **2009**, *19,* 1987–1992.

[98] A. B. Bourlinos, D. Gournis, D. Petridis, T. Szabò, A. Szeri, I. Décány. *Langmuir* **2003**, *19,* 6050–6055.

[99] G. Wang, J. Yang, J. Park, X. Gou, B. Wang, H. Liu, J. Yao. *J. Phys. Chem. C* **2008**, *112,* 8192–8195.

[100] R. Wissert, P. Steurer, S. Schopp, R. Thomann, R. Mülhaupt. *Macromol. Mater. Eng.* **2010**, *295,* 1107–1115.

[101] Z. Sui, X. Zhang, Y. Lei, Y. Luo. *Carbon* **2011**, *49,* 4314–4321.

[102] M. J. Fernández-Merino, L. Guardia, J. I. Paredes, S. Villar-Rodil, P. Solís-Fernández, A. Martínez-Alonso, J. M. D. Tascón. *J. Phys. Chem. C* **2010**, *114,* 6426–6432.

[103] X. Fan, W. Peng, Y. Li, X. Li, S. Wang, G. Zhang, F. Zhang. *Adv. Mater.* **2008**, *20,* 4490–4493.

[104] W. Yuan, B. Li, L. Li. *Appl. Surf. Sci.* **2011**, *257,* 10183–10187.

[105] T. Zhou, F. Chen, K. Liu, H. Deng, Q. Zhang, J. Feng, Q. Fu. *Nanotechnology* **2011**, *22,* 45704–45709.

[106] C. Ferrari, J. C. Meyer, V. Scardaci, C. Casiraghi, M. Lazzeri, F. Mauri, S. Piscanec, D. Jiang, K. S. Novoselov, S. Roth, A. K. Geim. *Phys. Rev. Lett.* **2006**, *97,* 187401.

[107] V. Y. Osipov, A. V. Baranov, V. A. Ermakov, T. L. Makarova, L. F. Chungong, A. I. Shames, K. Takai, T. Enoki, Y.

Kaburagi, M. Endo, A. Y. Vul'. *Diam. Relat. Mater.* **2011**, *20,* 205–209.

[108] Y. Guo, C. Bao, L. Song, B. Yuan, Y. Hu. *Ind. Eng. Chem. Res.* **2011**, *50,* 7772–7783.

[109] I. Y. Jeon, Y. R. Shin, G. J. Sohn, H. J. Choi, S. Y. Bae, J. Mahmood, S. M. Jung, J. M. Seo, M. J. Kim, D. W. Chang, L. Dai, J. B. Baek. *PNAS* **2012**, *109,* 5588–5593.

[110] R. Verdejo, F. Barroso-Bujans, M. A. Rodriguez-Perez, J. A. de Saja, M. A. Lopez-Manchado. *J. Mater. Chem.* **2008**, *18,* 2221–2226.

[111] L. J. Cote, R. Cruz-Silva, J. Huang. *J. Am. Chem. Soc.* **2009**, *131,* 11027–11032.

[112] T. Kuilla, S. Bhadra, D. Yao, N. H. Kim, S. Bose, J. H. Lee. *Progr. Polym. Sci.* **2010**, *35,* 1350–1375.

[113] C. Nethravathi, M. Rajamathi. *Carbon* **2008**, *46,* 1994–1998.

Section II

Rubber Nanocomposites

The text in this section is reproduced in part with permission from the following published works:

- V. Cipolletti, M. Galimberti, M. Mauro, G. Guerra. *Appl. Clay Sci.* **2014**, *87*, 179–188.
- M. Galimberti, V. Cipolletti, M. Mauro, L. Conzatti. *Macromol. Chem. Phys.* **2013**, *214*, 1931–1939.
- M. Galimberti, V. Cipolletti, S. Musto, S. Cioppa, G. Peli, M. Mauro, G. Guerra, S. Agnelli, T. Riccò, V. Kumar. *Proceedings at the Fall 184th Technical Meeting, Rubber Division of American Chemical Society, Cleveland, OH (USA), October* 8–10, **2013**.
- M. Galimberti, M. Coombs, V. Cipolletti, V. Kumar, M. Mauro, G. Guerra, L. Giannini. *Proceedings at the Fall 182nd Technical Meeting, Rubber Division of American Chemical Society, Cincinnati, OH (USA), October* 9–11, **2012**.

Chapter 3

Rubber/Organoclay Nanocomposites

3.1 Structure and Morphology of Organoclays in Rubber Nanocomposites

The world of rubber compounds was characterized, over the last years, by the appearance of a new family of reinforcing fillers, the so called nanofillers.[1] Basic features characterize their identity: they are made by primary particles, that can be individually dispersed in a polymer matrix, and have at least one dimension of one or few nanometers.

Conversely, it is well known that fillers such as carbon black (CB) and silica are nanostructured, being formed by aggregates of nano-sized primary particles that can not be separated via thermomechanical mixing.[2,3]

The nanometric size of nanofillers is at the origin of the impressive research activity developed on rubber compounds based on them, both in the academic and industrial worlds, as it is correlated with features that are of great importance for the reinforcement of rubber compounds: a huge specific surface area, a very low concentration for establishing a network in a polymer matrix (what is known as the percolation threshold) and, often, a high length-to-width ratio, that is a high aspect ratio.

Organically modified clays (OCs) have been prevailingly investigated [4–7] and it is nowadays well known that organophilic cations, preferentially with long alkyl chains, are used to compatibilize the hydrophilic pristine clays with the hydrophobic polymer matrix. In the world of polymer nanocomposites, the organization within a clay aggregate, in the polymer matrix, is particularly investigated, because it strongly affects the final properties of the composite material.

In the literature the following types of composites, arising from the interaction of layered silicates and polymers, are proposed (see **Fig. 3.1**), and they are called respectively microcomposite, exfoliated nanocomposite and intercalated nanocomposite.[4–7]

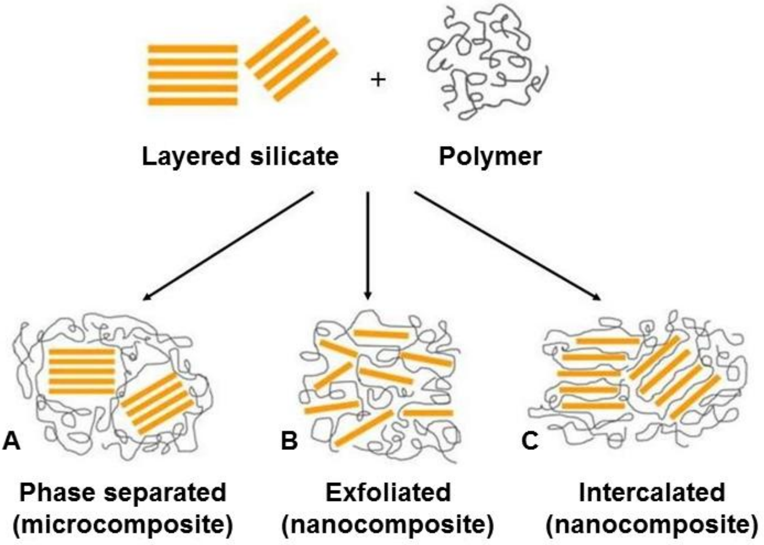

Fig. 3.1. Scheme of different types of composites arising from the interaction of layered silicates and polymers: (A) phase separated microcomposite, (B) exfoliated nanocomposite and (C) intercalated nanocomposite, after ref. 7.

Phase separated composite are reported to be formed when the polymer is unable to intercalate between the silicate layers (**Fig. 3.1A**) and properties stay in the same range as traditional microcomposites. Exfoliated or intercalated structures (Figs **3.1B,C**) are reported to be obtained when silicate layers are completely and uniformly dispersed in a continuous polymer matrix or when extended polymer chains are intercalated between the silicate layers resulting in a well ordered multilayer morphology built up with alternating polymeric and inorganic layers.[7]

The clay exfoliation is usually reported to occur through the following mechanism: intercalation of polymer chains, energetically favoured by the interaction between polymer and alkylammonium chains, expansion of interlayer distance and, finally, exfoliation.[4–6]

An alternative mechanism for explaining the formation of polymer/OC nanocomposites is available in the scientific literature. It is hypothesized that only low molecular mass substances, that means compensating cations and, optionally, further polar molecules, are intercalated in the clay interlayer space, being the intercalation of hydrophobic polymer chains highly unlikely to occur.[8–10]

Upon examining polymer/OC nanocomposites by means of X-ray Diffraction, reflections due to OC crystalline planes were observed at almost the same 2θ values in patterns of pristine OC and of polymer/OC nanocomposites and the small variations were attributed to the reorganization of molecules in the interlayer space. The relevant difference was the reduction of OC crystallites dimension in the direction orthogonal to the structural layers, interpreted with a different OC exfoliation degree. The reduction of number of stacked layers was explained with the so called "delamination mechanism",[8] a progressive peeling off of clay aggregates, excluding the intercalation of polymer chains.

In this paragraph the interaction of the rubber matrix with OCs was investigated in order to elucidate the structure and the morphology of the obtained OCs in rubber. OCs were first prepared by using the rubber matrix as reaction medium. Rubber nanocomposites were also prepared by melt blending OCs previously prepared in the solid state. The structure of OCs in rubber nanocomposites were finally compared with the ones obtained in the solid state (see chapter I in Section I). The preparation of rubber/OC nanocomposites and the characterization of their mechanical properties (see next paragraph) were performed by the group of Prof. Maurizio Galimberti at the Polytechnic of Milan. TEM analysis on rubber nanocomposites was performed by Dr. Lucia Conzatti at the CNR, Institute for Macomolecular Studies (ISMAC)-UOS Genova.

The reaction between pristine MMT and the ammonium salt 2HTCl was performed in poly(1,4-*cis* isoprene) (PIR) as the reaction medium, by melt blending the ingredients, as described in paragraph 8.14 in Section IV. The reaction was as well performed by blending either SA or SAES together with MMT and 2HTCl. The obtained nanocomposites had the same MMT content (about 5 phr), whereas the amounts of 2HT, SA and SAES were equal to the CEC of MMT.

Results from X-ray diffraction analysis are shown in **Fig. 3.2**. By comparing the patterns in **Fig. 3.2** with those reported in **Fig 1.7**, it is evident that the position of (00ℓ) reflections and the corresponding interlayer distances are essentially the same for OCs prepared from pristine MMT, 2HTCl and either SA or SAES either through the *neat* synthesis at the solid state or in the PIR as the reaction medium.

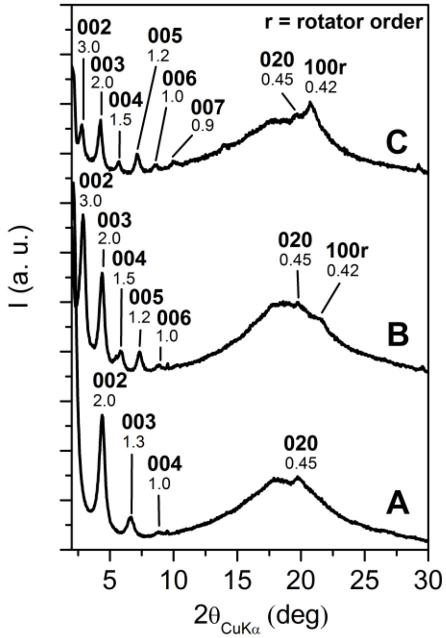

Fig. 3.2. X-ray diffraction patterns (Cu Kα) of of OC samples prepared in PIR as the reaction medium: (A) MMT/2HT, (B) MMT/2HT/SA, (C) MMT/2HT/SAES. The symbol **r** indicates the reflection relative to the rotator order.

Moreover, the inspection of **Fig. 3.2** reveals the presence of the reflection at $2\theta \approx 21°$, that indicates the occurrence of the hexagonal rotator order in the packing of long hydrocarbon tails of the compensating cation. These findings appear a clear indication that the same OCs are prepared at the solid state, in the absence of any other chemical substance, and in the polymer medium. The crystalline structure of OCs is dictated by the low molecular mass chemicals that are in the interlayer space, as suggested by the mechanism proposed by Galimberti *et al.* for the formation of polymer/OC nanocomposites.[8–10] One could add that reflections due to long sequences (the methylene sequences), usually attributed to polymeric chains, are present in the X-ray diffraction pattern, but they are due to the compensating cation and not to polymer chains of PIR that, evidently, do not take part in the crystalline structure.

Rubber nanocomposites were also obtained by melt blending 1,4-*cis*-polyisoprene (PIR) and OCs, previously prepared at the solid state (see chapter 1 in Section I). The nanocomposites were then crosslinked with a peroxide (see paragraph 8.15 in Section IV). Three types of OCs with different d_{001} interlayer distances, 2.5 nm, 4 nm and 6 nm were selected (extracted OC, MMT/2HT and MMT/2HT/SA in **Fig. 1.7**, renamed as OC 2.5nm, OC 4nm and OC 6nm in the following). They were then crosslinked with a peroxide. Formulations of the nanocomposites are shown in **Table 3.1**. The same amount of inorganic lamella was used in all the nanocomposites.

Table 3.1. Formulations of PIR-based nanocomposites with OCs previously prepared at the solid state.[a]

Ingredient	PIR/OC 4nm	PIR/OC 6nm	PIR/OC 2.5nm
PIR (phr)	100	100	100
OC (phr)	12	14.5	11.0
MMT in OC (phr)	6.96	6.96	6.96

[a]Other ingredients (expressed in phr): DCUP 1.4.

Results from X-ray diffraction and TEM analyses are shown in **Figs 3.3** and **3.4**. In the case of patterns of PIR/OC 4nm and PIR/OC 6nm in **Fig. 3.3B,C**, the same d_{001} interlayer distance detected in pristine OCs (see **Fig. 1.7**) was found in the nanocomposites. **Fig. 3.3C** also shows the occurrence of the hexagonal rotator order, clearly visible from the reflection at d = 0.42 nm. These results well agree with the same results obtained for previously described OCs prepared in rubber medium and, again, confirm the reliability of the mechanism proposed by Galimberti *et al.* for the formation of polymer/OC nanocomposites.[8–10]

Furthermore, TEM images of PIR/OC 4nm and PIR/OC 6nm in **Fig. 3.4B,C** show evenly distributed and well dispersed tactoids within the PIR matrix. In the pattern of PIR/OC 2.5nm in **Fig. 3.3A**, a d_{001} = 3.6 nm higher than the interlayer distance of the pristine OC 2.5nm is observed. However, TEM image in **Fig. 3.4A** shows a very bad dispersion of the clay particles within the PIR matrix, and it could be assumed that the expansion of the interlayer distance (from 2.5 nm to 3.6 nm) is due to the intercalation low molecular mass substances in the interlayer space of the clay aggregates. The intercalation of the polymer chains is completely excluded.

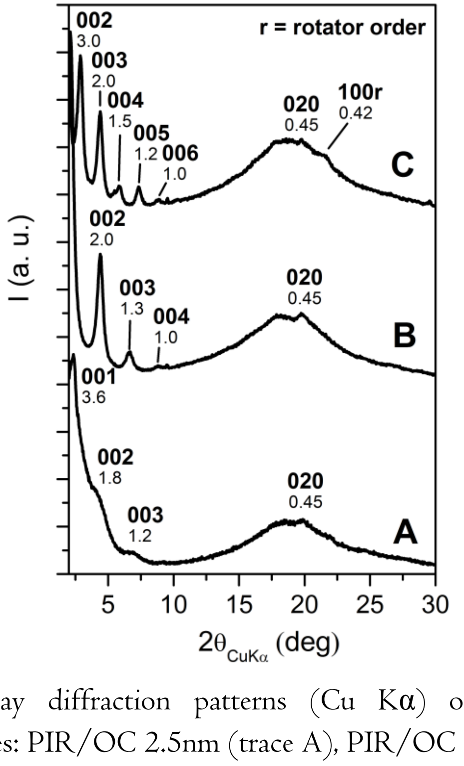

Fig. 3.3. X-ray diffraction patterns (Cu Kα) of crosslinked nanocomposites: PIR/OC 2.5nm (trace A), PIR/OC 4nm (trace B) and PIR/OC 6nm (trace C). The symbol **r** indicates the reflection relative to the rotator order.

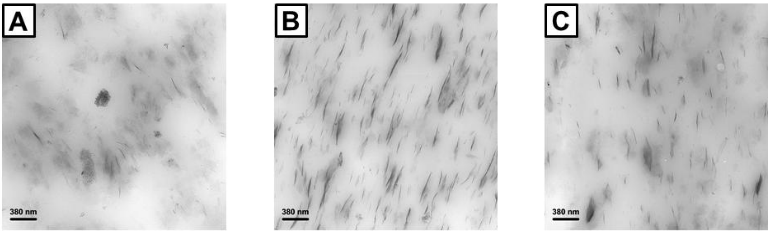

Fig. 3.4. TEM micrographs of crosslinked rubber nanocomposites: (A) PIR/OC 2.5nm, (B) PIR/OC 4nm and (C) PIR/OC 6nm.

Hence, experimental findings from the preparation of OCs: a) in the solid state (see chapter I in Section I), b) *in situ* in the rubber matrix and c) for melt blending of PIR and OCs, previously prepared at the solid state gave a strong support to the mechanism proposed by Galimberti *et al.* for polymer/OC nanocomposites formation.[8–10]

On the basis of this mechanism, the interlayer distance of two successive layers in a OC depends on the tilting angle of the substituents of the nitrogen atom of the compensating cation. The degree of order of OCs depends on the density of compatible hydrocarbon chains in the interlayer space: the higher is the density of such chains, as in the case of 2HT and SA or SAES, the higher is the degree of order.

3.2 Properties of Rubber/Organoclay Nanocomposites

OCs are characterized by reversible exothermic and endothermic phenomena, corresponding to the recovery and the loss of the rotator order, also in PIR-based nanocomposites. As already observed for OCs in the solid state (see paragraph I.2 in Section I), the DSC analysis of PIR/OC 6nm in **Fig. 3.5**, besides the glass transition of PIR at -65 °C, shows an irreversible first heating scan followed by reversible cooling and heating scans with peaks at 66 °C and at 74 °C, respectively.

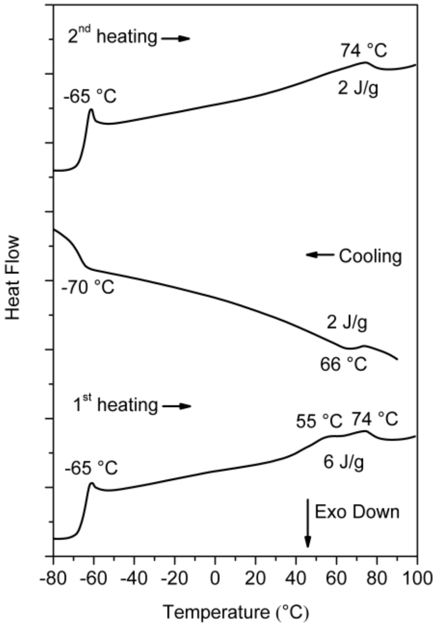

Fig. 3.5. DSC scans of rubber nanocomposite containing OC 6nm.

Tensile and dynamic-mechanical properties of rubber nanocomposites were found to be affected by the OC structure, namely by the interlayer distance. Nominal stress–nominal strain curves obtained from tensile tests are shown in **Fig. 3.6**, ultimate properties from tensile measurements are reported in **Table 3.2**, while curves of the dynamic storage modulus, determined in the shear mode, as a function of the strain amplitude are presented in **Fig. 3.7**.

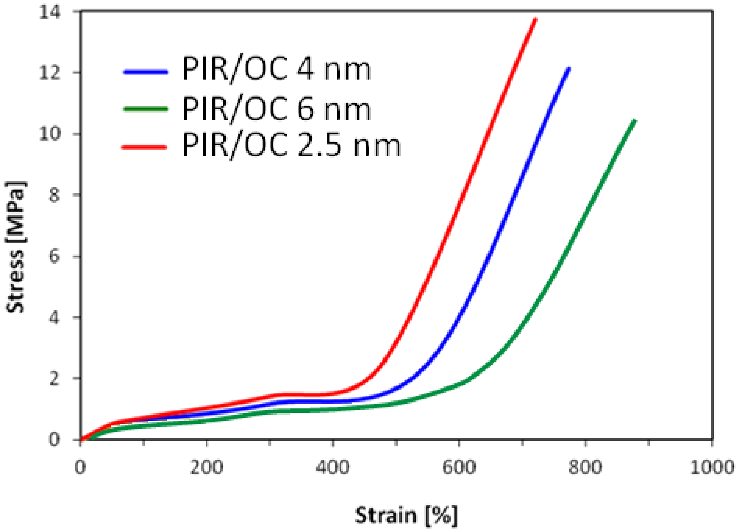

Fig. 3.6. Nominal stress–nominal strain curves obtained from tensile tests for rubber nanocomposites containing OC 2.5nm (red curve), OC 4nm (blue curve) and OC 6nm (green curve).

Table 3.2. Ultimate properties of PIR/OC 4nm, PIR/OC 6nm and PIR/OC 2.5nm composites.

	PIR/OC 4nm	**PIR/OC 6nm**	**PIR/OC 2.5nm**
ε_B (%)	762.0	878.0	720.2
σ_B (MPa)	11.4	10.4	13.9
Energy (J/cm^3)	18.4	19.2	21.2

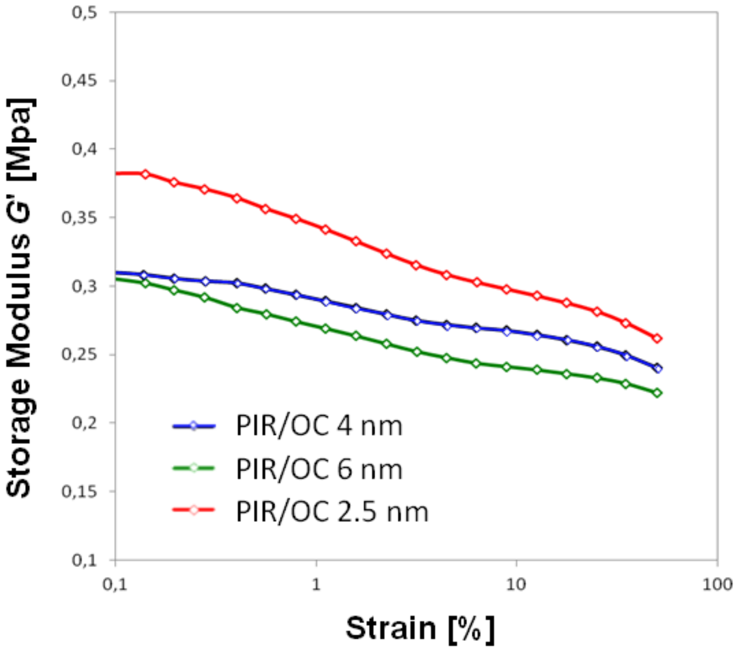

Fig. 3.7. G' values (MPa) versus strain amplitude for rubber nanocomposites containing OC 2.5nm (red curve), OC 4nm (blue curve) and OC 6nm (green curve).

The higher values for stresses at given elongations and for dynamic-mechanical moduli were obtained with OC having 2.5 nm as the d_{001} interlayer distance. These findings could be attributed to the large amount of the amphiphile in OC 4nm and OC 6nm that acts as plasticizer and leads to lower mechanical properties.

References

[1] M. Maiti, M. Bhattacharya, A. K. Bhowmick. *Rubber Chem. Technol.* **2008**, *81*, 384–469.

[2] A. I. Medalia, G. Kraus, in *The Science and Technology of Rubber* Second Ed.; J. E. Mark, B. Erman, F. R. Eirich, Eds. Elsevier Academic Press **1994**, Chapter 8, p. 387.

[3] J. B. Donnet, E. Custodero, in *The Science and Technology of Rubber Third Ed.*; J. E. Mark, B. Erman, F. R. Eirich, Eds. Elsevier Academic Press **2005**, Chapter 8, p. 367.

[4] S. S. Ray, M. Okamoto. *Progr. Polym. Sci.* **2003**, *28,* 1539–1641.

[5] R. Sengupta, S. Chakraborty, S. Bandyopadhyay, S. Dasgupta, R. Mukhopadhyay, K. Auddy, A. S. Deuri. *Polym. Eng. Sci.* **2007**, 1956–1974.

[6] B. Chen, J. R. G. Evans, H. C. Greenwell, P. Boulet, P. V. Coveney, A. A. Bowden, A. Whiting. *Chem. Soc. Rev.* **2008**, *37,* 568–594;

[7] M. Alexandre, P. Dubois. *Mater. Sci. Eng.* **2000**, *28,* 1–63.

[8] M. Galimberti, A. Lostritto, A. Spatola, G. Guerra. *Chem. Mater.* **2007**, *19,* 2495–2499.

[9] M. Galimberti, S. Senatore, L. Conzatti, G. Costa, G. Giuliano, G. Guerra. *Polym. Adv. Technol.* **2009**, *20,* 135–142;

[10] M. Galimberti, S. Giudice, V. Cipolletti, G. Guerra. *Polym. Adv. Technol.* **2010**, *21,* 679–684.

Chapter 4

Rubber/Graphite Oxide Intercalation Compound Nanocomposites

4.1 Structure and Morphology of Graphite Oxide Intercalation Compounds in Rubber Nanocomposites

Besides carbon black, fillers made of sp^2 carbon atoms, such as carbon nanotubes (CNTs) [1–5] and graphene or graphite nanoplatelets [6–9] were extensively reported for the preparation of polymer nanocomposites.

In the case of elastomers, graphite nanoplatelets are reported to improve mechanical,[10,11] electrical,[12,13] thermal,[14,15] barrier [16] and tribological [17] properties.

The non-covalent modification of GO by intercalation of long-chain amphiphilic guest molecules is a highly new and effective approach to improve the compatibility of GO for apolar rubbers. Hence, innovative nanocomposites are obtained by melt blending PIR and GOICs with 2HT cations ionically bonded to the graphite oxide layers. GOIC samples with different contents of 2HT are prepared and homogeneously dispersed in the PIR matrix. The preparation of rubber/GOIC nanocomposites and the characterization of their mechanical properties (see next paragraph) were performed by the group of Prof. Maurizio Galimberti at the Polytechnic of Milan. TEM analysis on rubber nanocomposites was performed by Dr. Lucia Conzatti at the CNR, Institute for Macomolecular Studies (ISMAC)-UOS Genova.

Two series of PIR-based nanocomposites (**Table 4.1**), containing different amounts (up to 7 phr) of GO/2HT-H or

GO/2HT-L (simply reported as H and L in **Table 4.1**) were prepared by melt blending (see paragraph 8.16 in Section IV). The content of graphitic layers is different in nanocomposites containing the same amount (phr) of either GO/2HT-H or GO/2HT-L. For example, in the nanocomposite with 7 phr as GO/2HT, the content of graphitic layers is about 1.3 phr and about 2.3 phr for GO/2HT-H and GO2HT-L, respectively.

Table 4.1. Formulations of PIR-based nanocomposites with GOICs.[a]

Ingredient	PIR/ H-1	PIR/ H-3	PIR/ H-7	PIR/ L-3	PIR/ L-7
PIR (phr)	100	100	100	100	100
GO/2HT-H (phr)	1	3	7	0	0
GO/2HT-L (phr)	0	0	0	3	7

[a]Other ingredients (expressed in phr): ZnO 4, stearic acid 2, 6PPD 2, sulphur 4.5 , DCBS 1.8, CTP 0.5.

The morphology and the structure of the crosslinked nanocomposites were investigated through TEM and WAXD analyses. TEM observations were carried out on a large number of cryosections obtained from different zones of the sample, collecting images at different magnifications, with the aim to evaluate the dispersion state of nanofiller within the PIR matrix. Representative images are shown in **Fig. 4.1** for PIR/H-7 (7 phr of GO/2HT-H) sample.

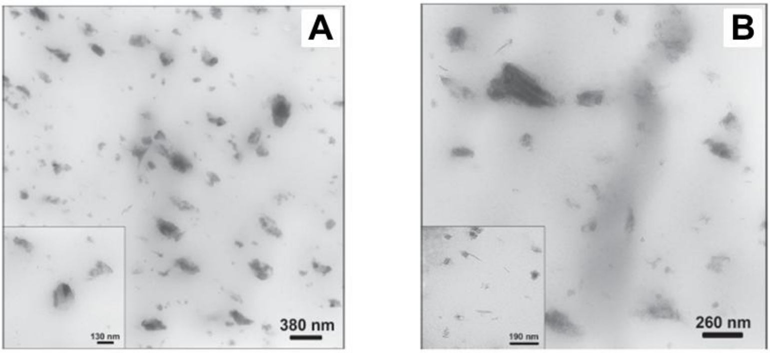

Fig. 4.1. Representative TEM micrographs of PIR/H-7 at different magnifications.

In both images, taken at low (**Fig. 4.1A**) and high magnification (**Fig. 4.1B**), groups of very small and dark particles appear. They are likely due to metal oxides coming from the preparation of GO, rather than to ZnO, added to nanocomposites for promoting the crosslinking reaction, as the typical crystals of ZnO are not visible. Nanofiller particles are frequently very close to the dark particles or are even included in them. As a consequence, the quantitative analysis of the GOIC dispersion by automated image analysis techniques could lead to unreliable results. Accurate qualitative observations, carried out on a large number of micrographs, indicate that GO/2HT-H is evenly distributed and highly dispersed within the PIR matrix. A high number of stacks with sub-micrometer dimensions are observed at low magnification, in the absence of agglomerates. Moreover, a high level of GO/2HT-H exfoliation is revealed by micrographs taken at high magnification: stacks, composed of less than six layers, are isotropically dispersed in the matrix (insert of **Fig. 4.1B**).

Fig. 4.2 shows the X-ray diffraction patterns of nanocomposites containing 7 phr of GO/2HT-H (trace A) or GO/2HT-L (trace B).

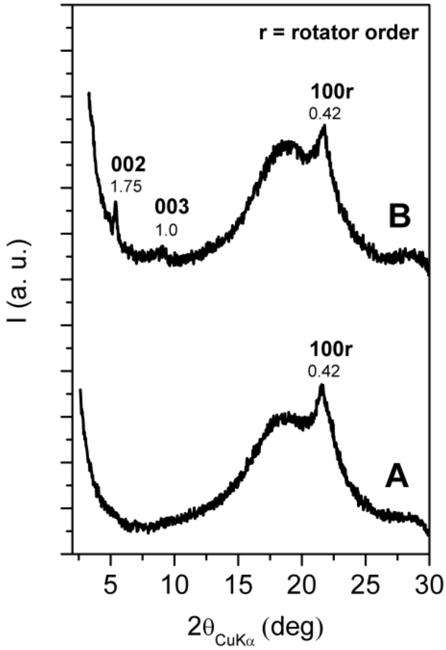

Fig. 4.2. X-ray diffraction patterns (Cu Kα) of crosslinked nanocomposites: PIR/H-7 (trace A) and PIR/L-7 (trace B). The symbol **r** indicates the reflection relative to the rotator order.

In both patterns, it is evident the 100r reflection due to the hexagonal rotator order of the methylene sequences of hydrocarbon chains (see chapter 2.5 in Section I). 00l reflections can be hardly identified in the pattern of PIR/L-7 and cannot be identified in the pattern of PIR/H-7. It could be thus hypothesized that GOICs are largely (GO/2HT-L) or prevailingly (GO/2HT-H) exfoliated in rubber matrix.

4.2 Properties of Rubber/Graphite Oxide Intercalation Compound Nanocomposites

GOICs also exhibit reversible thermal transitions both at the solid state (see paragraph 2.5 in Section I) and in the rubber matrix. From the DSC analysis of PIR/H-7 in **Fig. 4.3**, the recovery and the loss of the rotator order are clearly visible during the cooling and the second heating scans, and confirm the results obtained by X-ray diffraction analysis. Such findings are very interesting, in fact, although GOICs result prevaingly exfoliated in the rubber matrix (see **Figs 4.1** and **4.2**), their rotator order is preserved and, therefore, represents a sort of filler fingerprint.

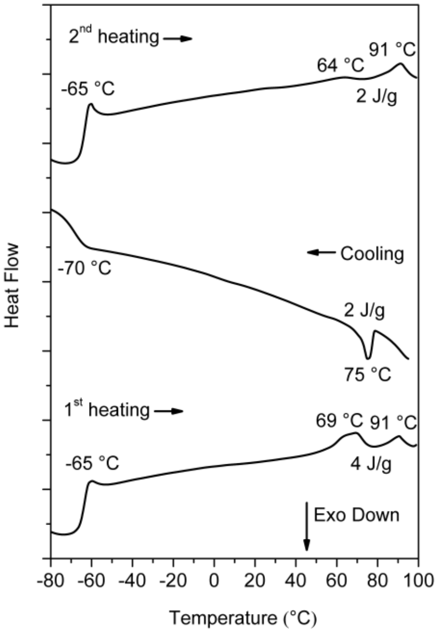

Fig. 4.3. DSC scans of rubber nanocomposite containing GO/2HT-H.

Nominal stress–nominal strain curves obtained from tensile tests are shown in **Fig. 4.4** for nanocomposites containing GO/2HT-H.

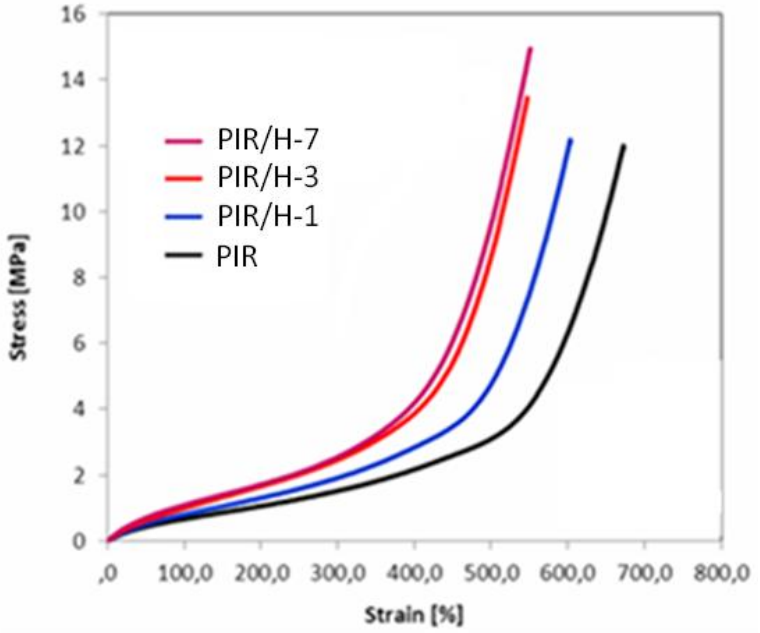

Fig. 4.4. Nominal stress–nominal strain curves obtained from tensile tests for rubber nanocomposites containing GO/2HT-H.

The stress at a given elongation increases up to 3 phr as the GOIC content. A further increase of the nanofiller amount (7 phr) does not lead to a significant improvement of stress values, at any elongation. Reinforcement under strain, with sudden increase of the stress-strain curves slope, is evident for all the composites and it could be attributed to the strain-induced crystallization (SIC) phenomenon,[18] known to occur when a polymer such as PIR is stretched. The addition of the GOIC leads to an appreciable reduction of the strain needed to have the SIC phenomenon: from about 550% for neat PIR to about 250% for nanocomposites with 3 or 7 phr of the GOIC. The nucleating effect of GOIC could be hypothesized to allow an easier crystallization under strain, as reported in the literature for nanocomposites based on NR and OC.[19]

Table 4.2 shows the composites ultimate properties. The addition of GOICs to PIR led to a reduction of the elongation at break (ε_B) and to an increase of tensile strength (σ_B) and energy at break, as a consequence of the reinforcement under strain above commented.

Table 4.2. Ultimate properties of PIR-based nanocomposites with GOICs.

	PIR	**PIR/H-1**	**PIR/H-3**	**PIR/H-7**
ε_B (%)	678.7	592.9	551.3	555.3
σ_B (MPa)	12.0	11.0	13.5	15.0
Energy (J/cm^3)	18.2	16.0	18.2	20.3

To give an explanation for the very similar stress–strain behavior of nanocomposites with 3 or 7 phr of the GOIC, one could take into account the conflicting effects of, on one side, the higher amount of graphitic layers, that lead to a higher reinforcement, and, on the other side, of the long hydrocarbon chains, that lead to lower mechanical properties. Said hydrocarbon chains could favor the slippage of the GOIC on the polymer chains, particularly as the strain increases.

The dynamic behavior of PIR nanocomposites containing either GO/2HT-H or GO/2HT-L was preliminarily investigated through strain sweep tests in torsion mode, determining dynamic shear storage, G', and loss, G'', moduli in the strain amplitude range from 0.1% to 10%.

Table 4.3. Dynamic storage modulus, G', and dynamic loss modulus, G'', obtained for PIR-based nanocomposites with GOICs of Table 4.1.

	PIR	PIR/ H-1	PIR/ H-3	PIR/ H-7	PIR/ L-3	PIR/ L-7
G'(0.1%) (MPa)	0.42	0.51	0.58	0.55	0.51	0.57
ΔG'(0.1%-10%) (MPa)	0.06	0.08	0.07	0.07	0.04	0.13
G'' (10%)	0.018	0.018	0.017	0.022	0.014	0.021

Values of G'(0.1%), ΔG' (0.1% – 10%), and G'' (10%) are reported in **Table 4.3**: they are in narrow ranges, as expected in consideration of the low amounts of the GOIC in the nanocomposites. The addition of GO/2HT to the PIR matrix led to the increase of G' (0.1%). In the case of GO/2HT-H, the G' (0.1%) value does not increase passing from 3 to 7 phr as nanofiller content. This finding could be attributed to the large amount of the amphiphile that acts as plasticizer. For both GO/2HT samples, an appreciable increase of G'' and of ΔG' (0.1% – 10%) is observed only for 7 phr as the nanofiller content.

In conclusion GOICs with different content of 2HT cations were evenly dispersed in the PIR matrix and were found to be prevailingly exfoliated. The PIR properties were appreciably affected by the GOICs. Stresses at given elongations, from tensile tests, and dynamic storage and loss moduli increased by adding a GOIC to PIR. However, in the case of GO/2HT-H, a larger amount of the GOIC did not lead to a substantial increase of mechanical reinforcement: the long hydrocarbon chains seem to act as plasticizer, compensating the reinforcing effect of the GO layers. GOICs with lipophilic ammonium cations in the interlayer space appear very interesting nanofillers for the preparation of polymer nanocomposites. They can be efficiently dispersed in the polymer matrix, achieve a high degree of exfoliation and affect, to a large extent, the polymer properties.

References

[1] L. Bokobza. *Polymer* **2007**, *48,* 4907–4920.

[2] G. Sui, W. H. Zhong, X. P. Yang, S. H. Zhao. *Macromol. Mater. Eng.* **2007**, *292,* 1020–1026.

[3] C. Nah, J. Y. Lim, R. Sengupta, B. H. Cho, A. N. Gent. *Polym. Int.* **2011**, *60,* 42–44.

[4] G. Sui, W. H. Zhong, X. P. Yang, Y. H. Yu, S. H. Zhao. *Polym. Adv. Technol.* **2008**, *19,* 1543–1549.

[5] A. Das, K. W. Stöckelhuber, R. Jurk, M. Grenzer, J. Fritzsche, H. Lorenz, M. Klüppel, G. Heinrich. *Polymer* **2008**, *49,* 5276–5283.

[6] H. Kim, A. A. Abdala, C. W. Macosko. *Macromolecules* **2010**, *43,* 6515–6530.

[7] T. Kuilla, S. Bhadra, D. Yao, N. H. Kim, S. Bose, J. H. Lee. *Progr. Polym. Sci.* **2010**, *35,* 1350–1375.

[8] R. Sengupta, M. Bhattacharya, S. Bandyopadhyay, A. K. Bhowmick. *Progr. Polym. Sci.* **2011**, *36,* 638–670.

[9] J. R. Potts, D. R. Dreyer, C. W. Bielawski, R. S. Ruoff. *Polymer* **2011**, *52,* 5–25.

[10] N. Yan, H. Xia, J. Wu, Y. Zhan, G. Fei, C. Chen. *J. Appl. Polym. Sci.* **2013**, *127,* 933–941.

[11] J. Yang, M. Tian, Q. X. Jia, L. Q. Zhang, X. L. Li. *J. Appl. Polym. Sci.* **2006**, *102,* 4007–4015.

[12] A. Malas, C. K. Das, A. Das, G. Heinrich. *Mater. Design* **2012**, *39,* 410–417.

[13] M. M. de Hernández, M. Bernal, R. Verdejo, T. A. Ezquerra, M. A. López-Manchado. *Comp. Sci. Technol.* **2012**, *73,* 40–46.

[14] S. H. Song, H. K. Jeong, Y. G. Kang. *J. Ind. Eng. Chem.* **2010**, *16,* 1059–1065.

[15] Q. H. Mu, S. Y. Feng. *Thermochim. Acta* **2007**, *462,* 70–75.

[16] J. Yang, M. Tian, Q. X. Jia, J. H. Shi, L. Q. Zhang, S. H. Lim, Z. Z. Yu, Y. W. Mai. *Acta Mater.* **2007**, *55,* 6372–6382.
[17] L. Wang, L. Zhang, M. Tian. *Wear* **2012**, *276,* 85–93.
[18] C. M. Roland, in *The Science and Technology of Rubber,* 3rd ed., Eds: J. E. Mark, B. Erman, F. R. Eirich, Elsevier Academic Press, London, UK, **2005**, p. 105.
[19] J. Carretero-Gonzalez, R. Verdejo, S. Toki, B. S. Hsiao, E. P. Giannelis, M. A. Lopez-Manchado. *Macromolecules* **2008**, *41,* 2295–2298.

Section III

Metathesis Reactions in Rubber Chemistry

Chapter 5

Olefin Metathesis

5.1 Introduction

In recent years, the olefin metathesis reaction has attracted widespread attention as a versatile carbon-carbon bond-forming method. The name metathesis was given for the first time to this reaction by Calderon in 1967 [1] and the etymology of the word metathesis derives from the Greek *meta* (change) and *thesis* (position). In chemistry, olefin metathesis is a unique transition metal–mediated transformation that rearranges the carbon atoms of carbon-carbon double bonds (**Scheme 5.1**).[2]

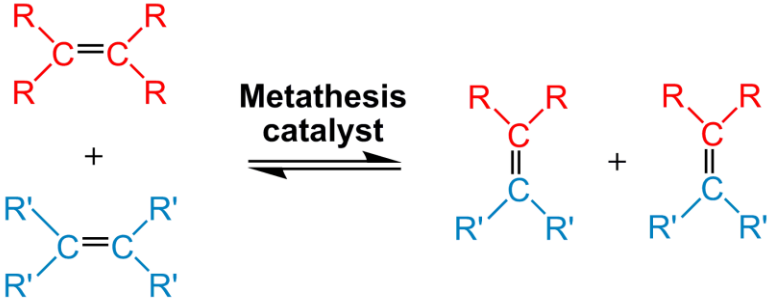

Scheme 5.1. Principle of olefin metathesis.

The accepted mechanism, reported in **Scheme 5.2**, was originally proposed by Chauvin [3] and supported by Grubbs.[4] It involves olefin coordination to a transition metal–alkylidene complex, followed by a [2+2]-cycloaddition reaction that generates a new carbon-carbon bond and affords a metallacyclobutane intermediate, and finally a [2+2]-cycloreversion reaction, which regenerates a metal-alkylidene and a coordinated olefin product.

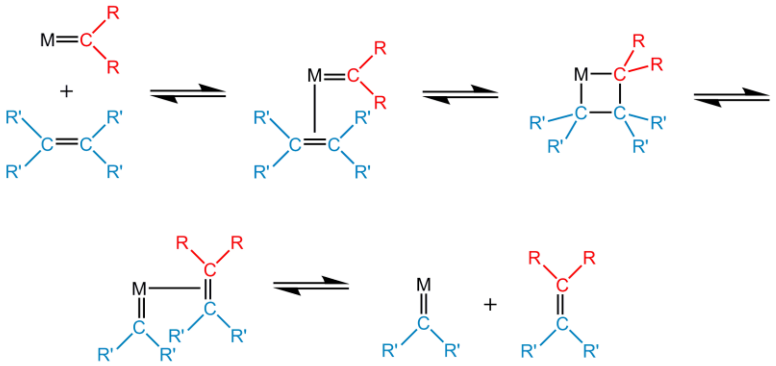
Scheme 5.2. General mechanism for olefin metathesis.

The individual steps in the catalytic cycle of the olefin metathesis reaction are reversible and the substrate-product equilibrium is governed by thermodynamic control. Therefore, most protocols rely on a driving force, such as the formation of ethylene or the release of ring strain, to favor the formation of a single product.[5]

The classifications of olefin metathesis reactions are summarized in **Scheme 5.3**, including cross metathesis (CM), ring-closing metathesis (RCM), ring-opening metathesis (ROM), ring opening metathesis polymerization (ROMP), and acyclic diene metathesis polymerization (ADMET). Through the application of these methodologies and others, olefin metathesis has become an increasingly important and powerful reaction that is widely used in both organic synthesis and polymer science.[6–8]

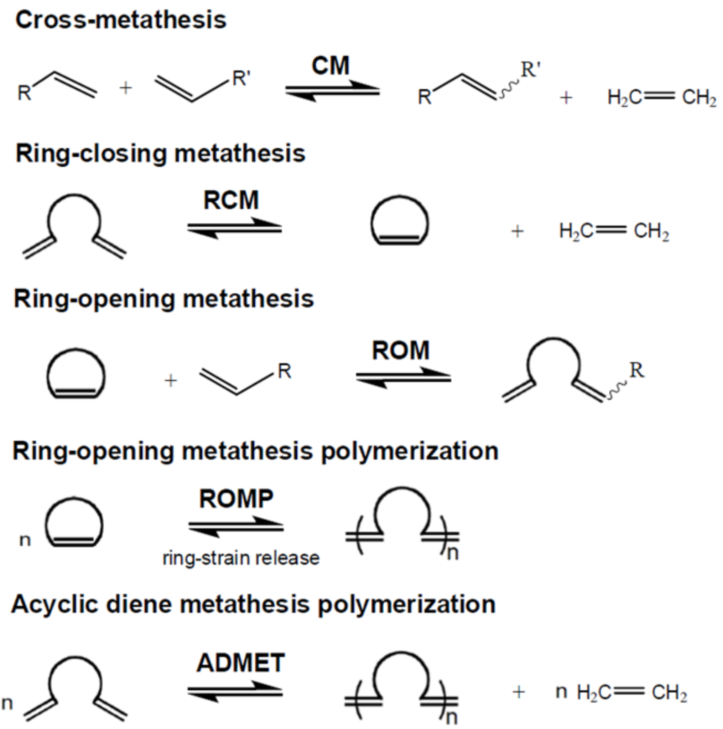

Scheme 5.3. Different types of olefin metathesis reactions commonly employed.

Catalytic metathesis was discovered in the 1950s by Karl Ziegler, following the observations concerning the polymerization of ethylene.[9] The most important applications of olefin metathesis in the field of petrochemicals were developed in the 1960s with the Phillips Triolefin Process and in the 1970s with the Shell Higher Olefins Process.[10] The discovery that metal alkylidene complexes could act as single-component catalysts for olefin metathesis was the first step towards the development of this reaction in organic synthesis. With the advent of efficient catalysts, such as Schrock's and Grubbs' catalysts and their derivatives, this reaction has emerged as a powerful tool for the formation of C-C bonds in chemistry.[11,12]

There are an extensive number of catalyst systems that can initiate an olefin metathesis reaction and most of the early work was based on the use of ill-defined multicomponent homogeneous and heterogeneous catalyst complexes.[13] Some of the most commonly used systems included WCl_6/Bu_4Sn, $WOCl_4/EtAlCl_2$, MoO_3/SiO_2, and Re_2O_7/Al_2O_3, which consist of transition metal salts combined with main group alkylating agents, or solid supports.[2] The utility of these catalysts was limited, since the harsh conditions and strong Lewis acids required are incompatible with most functional groups. The isolation of the first well-defined metal alkylidene complexes in the 1970s spurred great advances in catalyst design, leading to titanium [14] and molybdenum complexes,[15] that are active in olefin metathesis reactions (**Fig. 5.1**). The different metals impart different reactivities to the alkylidenes, and small adjustments in the ligand environment can cause large changes in catalyst behavior.

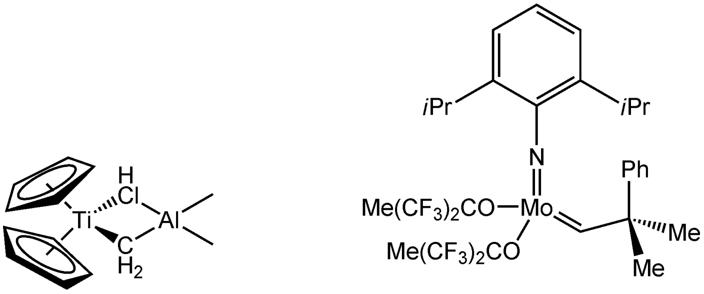

Tebbe Reagent **Schrock Catalyst**

Fig. 5.1. Titanium and molybdenum olefin metathesis catalysts.

5.2 Grubbs Catalysts

In the late 1980s it was found that ruthenium chlorides, $RuCl_3(H_2O)_n$, were able to catalyze ring-opening metathesis polymerization by the metal-alkylidene mechanism.[16] During the 1990s, Grubbs and co-workers synthesized and isolated ruthenium vinylalkylidene complex of **Fig. 5.2**, which allowed the development of well defined, low oxidation, late transition state metal complexes, that catalyze olefin metathesis.[17]

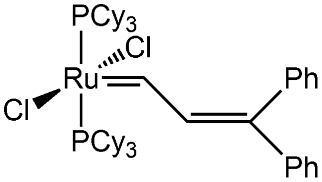

Fig. 5.2. The first stable and active ruthenium alkylidene metathesis catalysts.

The remarkable functional group tolerance and stability towards air, acids and even water, made this class of catalyst particularly attractive for practical applications. Further development led to the so-called first generation Grubbs catalyst (G1),[18] which contains two phosphine ligands, two chlorides and an alkylidene ligand. Although this catalytic system showed high levels of reactivity, the Grubbs second generation catalyst (G2),[19] where one of the phosphine ligands is replaced by a *N*-heterocyclic alkylidene (NHC) ligand, displayed increased reactivity and stability (**Fig. 5.3**).

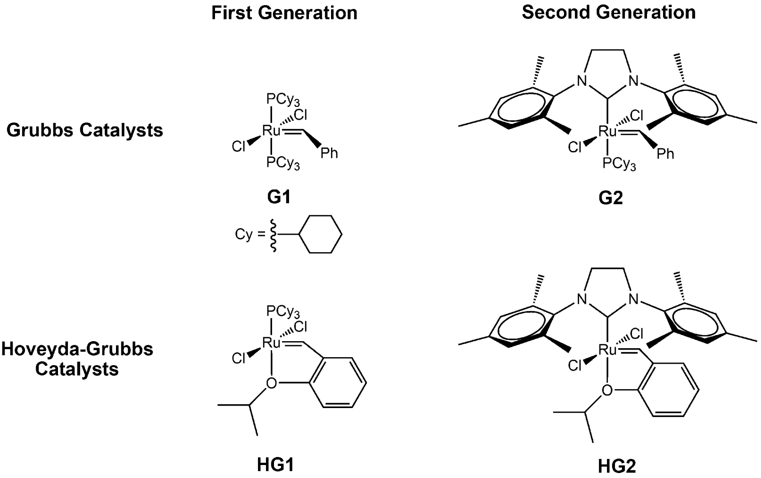

Fig. 5.3. First and second generation Ru-based olefin metathesis catalysts.

The Grubbs catalysts are based on a $X_2L_2Ru{=}CHR$ platform comprised of a ruthenium alkylidene, two anionic, and two neutral ligands. The other widely used and commercially available ruthenium complexes were reported by Hoveyda (HGI and HG2),**[20]** where the isopropoxystyrene ligand on the alkylidene unit replaces a phosphine ligand and stabilizes the complexes in their resting state, but readily opens to provide a coordination site in the presence of the substrate. The four ruthenium catalysts presented in **Fig. 5.3** are all pre-catalysts, meaning that the active species are generated under the reaction conditions. The proposed mechanism for Grubbs catalysts, reported in **Scheme 5.4**, involves the dissociation of the phosphine ligand from 16-electrons metal complex to form a 14-electrons complex, that is able to coordinate an olefin. For the first generation Grubbs catalysts the loss of a phosphine ligand is relatively facile, but the re-coordination of the phosphine ligand competes with the coorination of the olefin and is much faster than that of the olefin. Therefore the active species is formed more readily but carries out fewer turnovers. For the second generation Grubbs catalysts, both the dissociation and re-association of the phosphine are slow processes, therefore the active species can undergo a larger number of turnovers.**[21]**

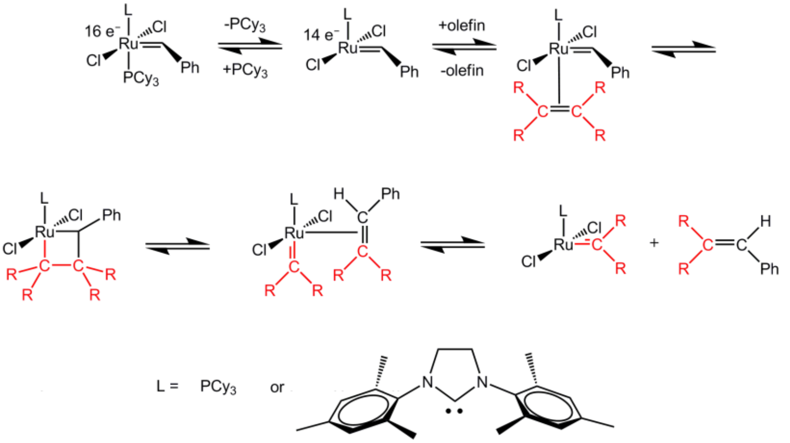

Scheme 5.4. Proposed mechanism for Grubbs catalysts.

References

[1] N. Calderon. *Tetrahedron Lett.* **1967**, *34,* 3327–3329.

[2] R. H. Grubbs. *Handbook of Metathesis*; Wiley-VCH:Weinheim, Germany, **2003**.

[3] P. Jean-Louis Hérisson, Y. Chauvin. *Die Makromolekulare Chemie* **1971**, *141,* 161–176.

[4] M. Scholl, S. Ding, C. W. Lee, R. H. Grubbs. *Org. Lett.* **1999**, *1,* 953–956.

[5] K. B. Wiberg. *Angew. Chem. Int. Ed.* **1986**, *25,* 312–322.

[6] A. H. Hoveyda, A. R. Zhugralin. *Nature* **2007**, *450,* 243–251.

[7] K. J. Ivin, J. C. Mol. *Olefin Metathesis and Metathesis Polymerization*; Academic Press: San Diego, CA, **1997**.

[8] K. C. Nicolaou, P. G. Bulger, D. Sarlah. *Angew. Chem., Int. Ed.* **2005**, *44,* 4490–4527.

[9] K. Ziegler, *Angew. Chem.* **1964**, *76,* 545–553.

[10] J. C. Mol. *J. Mol. Cat. A* **2004**, *213,* 39–45.

[11] R. H. Grubbs. *Tetrahedron* **2004**, *60,* 7117–7140.

[12] A. Fürstner. *Angew. Chem. Int. Ed.* **2000**, *39,* 3012–3043.

[13] R. H. Grubbs, S. Chang. *Tetrahedron* **1998**, *54,* 4413–4450.

[14] F. N. Tebbe, G. W. Parshall, D. W. Ovenall. *J. Am. Chem. Soc.* **1979**, *101,* 5074–5075.

[15] R. R. Schrock, J. S. Murdzek, G. C. Bazan, J. Robbins, M. DiMare, M. O'Regan. *J. Am. Chem. Soc.* **1990**, *112,* 3875–3886.

[16] B. M. Novak, R. H. Grubbs. *J. Am. Chem. Soc.* **1988**, *110,* 960–961.

[17] S. T. Nguyen, L. K. Johnson, R. H. Grubbs, J. W. Ziller. *J. Am. Chem. Soc.* **1992**, *114,* 3974–3975.

[18] P. Schwab, M. B. France, J. W. Ziller, R. H. Grubbs. *Angew. Chem. Int. Ed.* **1995**, *34,* 2039–2041.

[19] M. Scholl, S. Ding, C. W. Lee, R. H. Grubbs. *Org. Lett.* **1999**, *1,* 953–956.

[20] S. B. Garber, J. S. Kingsbury, B. L. Gray, A. H. Hoveyda. *J. Am.*

Chem. Soc. **2000**, *122,* 8168–8179.

[21] M. S. Sanford, J. A. Love, R. H. Grubbs. *J. Am. Chem. Soc.* **2001**, *123,* 6543–6554.

Chapter 6

Rubber-Scrambling Metathesis Reactions

6.1 Macromolecular Cross-Metathesis

The macromolecular cross-metathesis (MCM) reactions are an interesting class of cross-metathesis reactions, that provide a powerful synthetic methodology for chain interchange (polymer scrambling) between olefin-containing polymers, mediated by metathesis catalysts.

As illustrated in **Scheme 6.1**, when two different types of olefin-containing polymers are treated with a suitable metathesis catalyst, the various chains will interchange and, at equilibrium, result in a material with a random distribution of segments coming from both base polymers.[1]

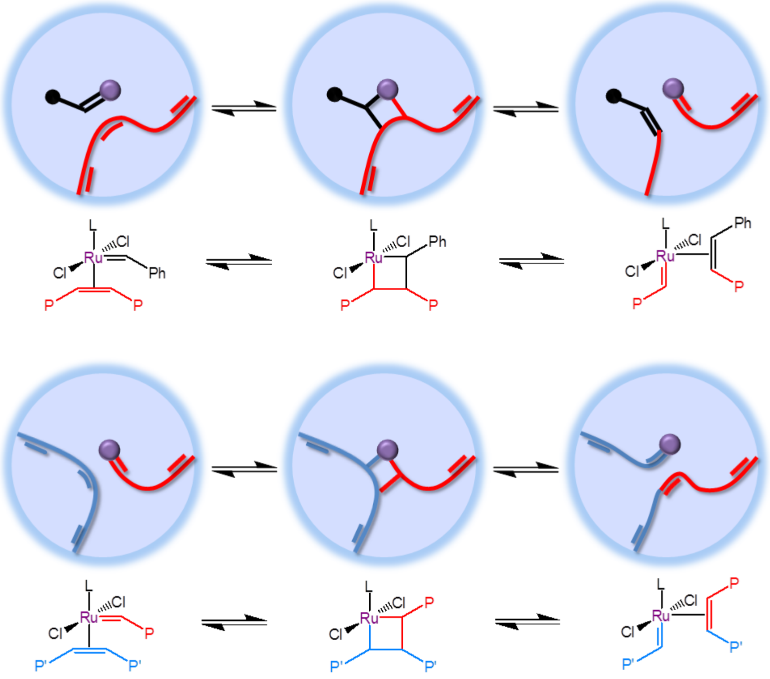

Scheme 6.1. Principle of macromolecular cross-metathesis. Each productive Ru-catalyzed metathesis reaction promotes a chain interchange between the base polymers.

Hence, the MCM of olefin-containing polymers, prepared by different polymerization methods, such as step-growth polymerization, chain-growth polymerization or others, allows to prepare random multiblock copolymers (see **Scheme 6.2**), hardly obtainable with conventional polymerization methodologies.[2]

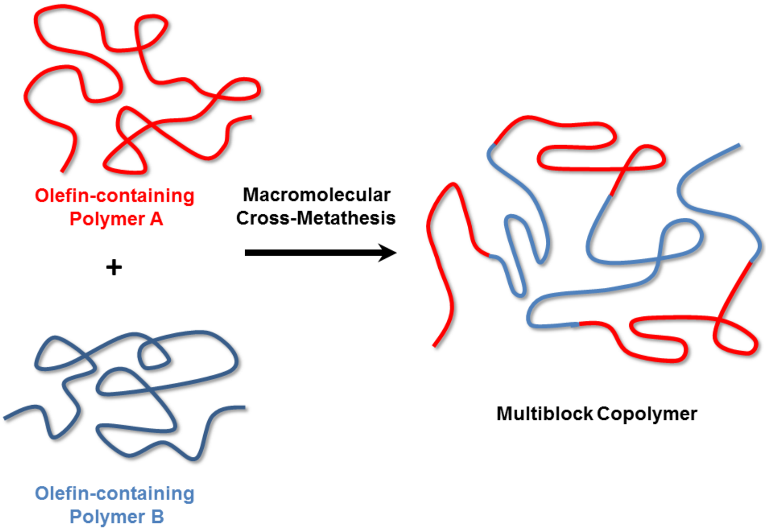

Scheme 6.2. Production of random multiblock copolymers by macromolecular cross-metathesis, starting from different olefin-containing polymers.

A plausible MCM mechanism is here proposed, according to the Chauvin mechanism of a common cross-metathesis reaction. In the case of MCM, chain interchange occurs between olefin-containing polymers (see **Scheme 6.3**).

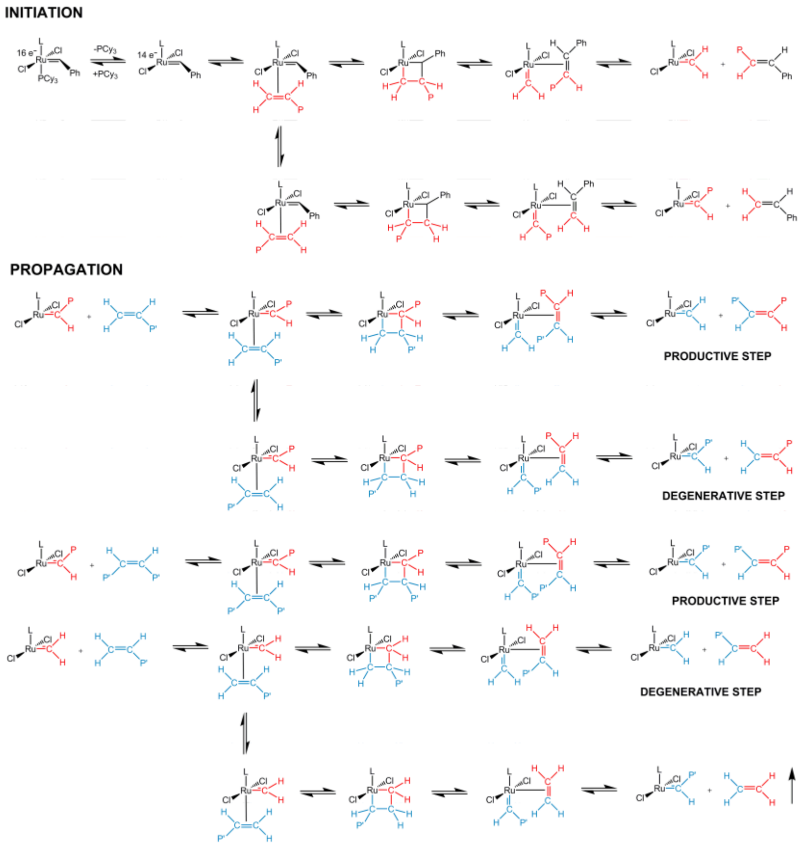

Scheme 6.3. Plausible MCM mechanism.

The initiation step involves a metal-alkylidene species (or more precisely metal-alkylidene), the coordination of the olefin onto the metal atom of this species, followed by the shift of the coordinated olefin to form the metallacyclobutane intermediate, and finally the topologically identical shift of the new coordinated olefin in the metallocyclobutane in a direction perpendicular to the initial olefin shift. This forms a metal-alkylidene to which the new olefin is coordinated, then liberated.

The new metal-alkylidene contains one of the two alkylidenes of the starting olefin and it can re-enter into catalytic cycles of the same type as the first one, during the propagation steps.

In fact, depending on the orientation of the coordinated olefin, the new catalytic cycle can give different metallacyclobutanes, some of which leading to productive metathesis steps and the other one leading to degenerative metathesis steps, because the coordination of internal double bonds to the metal-alkylidene species always provides a productive step, while the coordination of a terminal olefin to a $Cl_2LRu=CH_2$ species always provides a degenerative step.

Very few examples of MCM are reported in the literature, in particular Wagner *et al.* prepared polycarbonate/polyethylene random block copolymers by MCM, starting from polycarbonate and polyethylene both with random backbone unsaturation.[3] Otsuka *et al.* reported the MCM of 1,4-polybutadiene with an olefin-containing polyester,[2] while Guan *et al.* demonstrated the efficiency of MCM in making cross-linked and malleable polybutadiene.[1] The great interest for MCM reactions is also testified by recent patents.[4,5]

In this contest rubber-scrambling metathesis reactions by MCM of high-*cis* polydienes, such as 1,4-*cis*-polybutadiene (PBR) and 1,4-*cis*-polyisoprene (PIR) were deeply investigated and discussed in the next paragraphs. High *cis*-1,4 PBR and PIR are immiscible and miscibility is observed only when PBR has a high vinyl-1,2 content.[6] The prepared random multiblock PBR-PIR copolymers could have a potential application as compatibilizers for PBR-PIR blends.

6.2 Multiblock Copolymers of High-*cis* Polybutadiene and Polyisoprene by Macromolecular Cross-metathesis

The stereoselective polymerization of conjugated dienes, namely 1,3-butadiene and isoprene, is a subject of both scientific and industrial interest.[7–9]

High *trans*-1,4 copolymers of butadiene and isoprene are obtained by vanadium,[10] anion,[11] alfin,[12] or supported titanium [13] catalyst systems.

High *cis*-1,4 polydienes are important materials used, mostly, for tires manufacturing and catalytic systems based on lanthanides, especially neodymium, have attracted a great deal of attention for the homo- and copolymerization of conjugated dienes, due to their high catalytic activity and high *cis* -1,4 selectivity.[14–18]

Due to the high oxophilicity of their metal centers, the main drawback of the above mentioned catalyst systems is their high sensitivity to oxygen and water or to the presence of polar functional groups on the reacting substrates.

Ru-based metathesis catalysts, instead, combine excellent activity with broad functional group tolerance and thermal stability.[19] Moreover, the most interesting aspect of the MCM catalyzed by first generation Ru-based catalysts is that they allow to prepare random multiblock PBR-PIR copolymers, hardly obtainable with the conventional methods, starting directly from the high molecular weight homopolymers.[2,3]

The results presented in this paragraph deal with the preparation and the characterization of high-*cis* random multiblock PBR-PIR copolymers by MCM with GI and HGI.

6.2.1 Characterization of the Starting Homopolymers

First of all, PBR and PIR homopolymers were characterized and the results are reported below. Carbons and units, observed in ^{13}C-NMR spectra of PBR (see **Fig. 6.1A–C**) and PIR (see **Fig. 6.2A–C**), are labelled according to **Scheme 6.4**. Main peaks in ^{13}C-NMR spectra were attributed according to the work of Matsuzaki *et al.*[20]

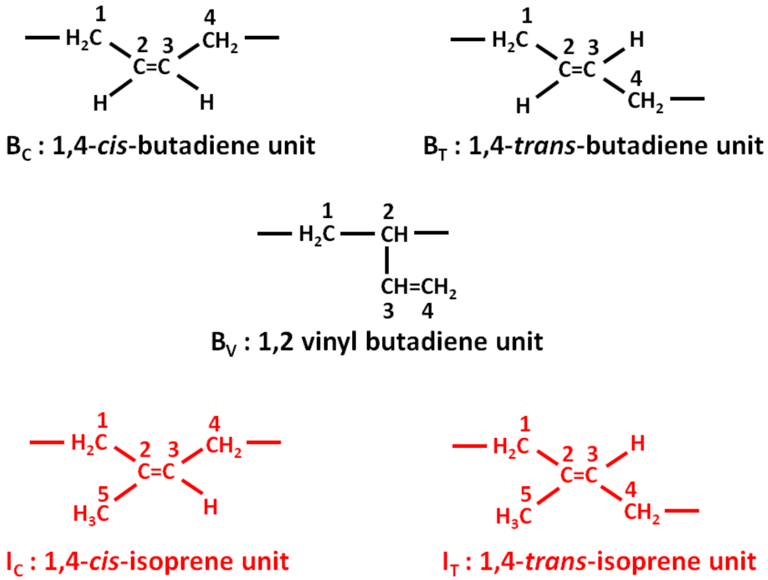

B_C : 1,4-*cis*-butadiene unit

B_T : 1,4-*trans*-butadiene unit

B_V : 1,2 vinyl butadiene unit

I_C : 1,4-*cis*-isoprene unit

I_T : 1,4-*trans*-isoprene unit

Scheme 6.4. Butadiene and isoprene units observed in ^{13}C-NMR spectra of PBR and PIR reported in **Figs 6.1A–C** and **6.2A–C**.

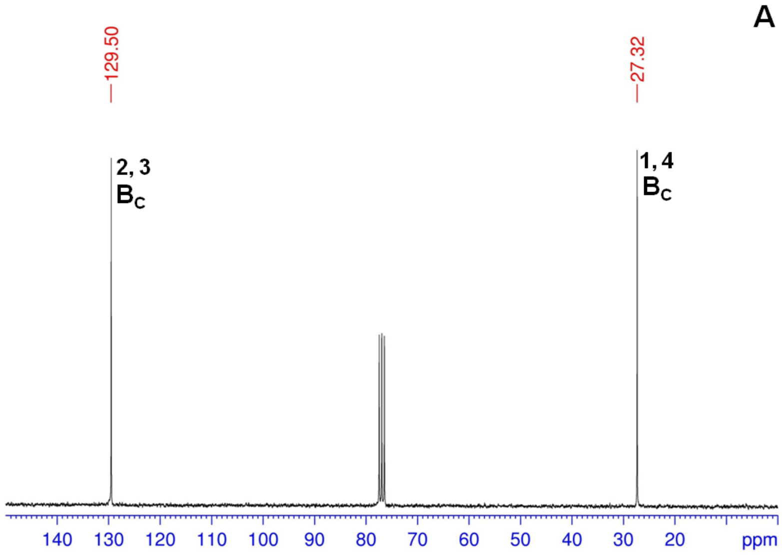

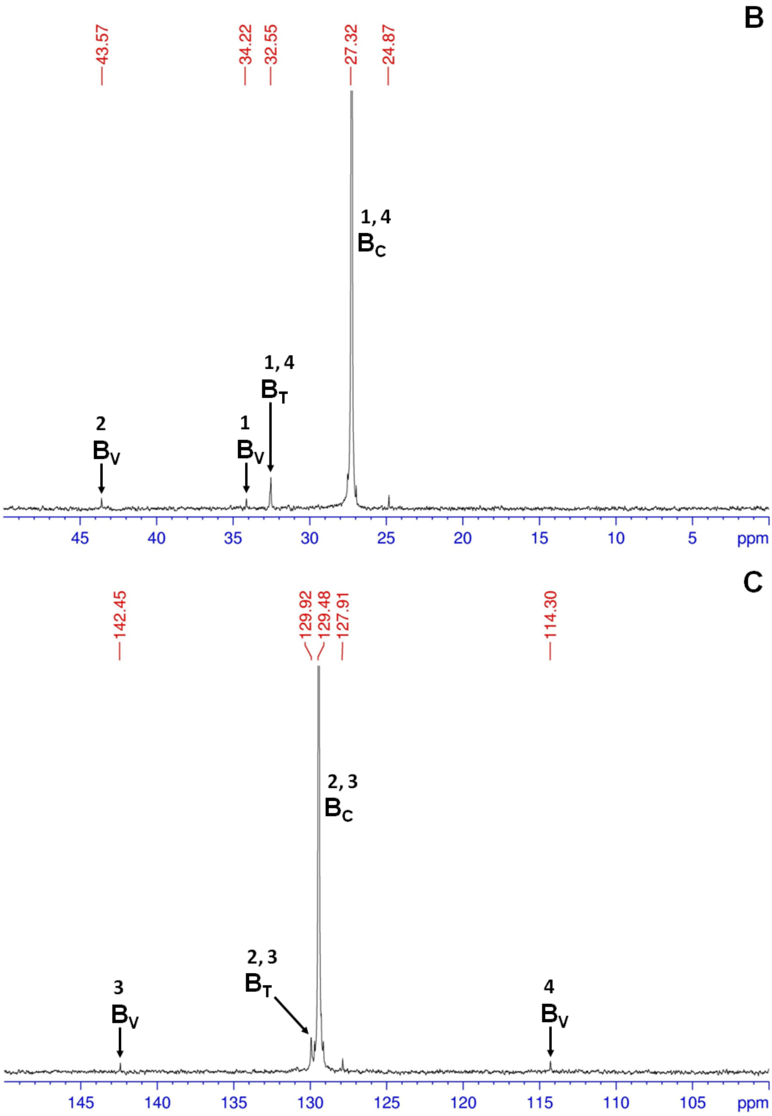

Fig. 6.1. ^{13}C-NMR spectra (100 MHz, in CDCl$_3$, TMS scale) of PBR: (A) entire spectrum, (B) saturated and (C) olefinic carbon regions.

PBR ^{13}C NMR analysis (100 MHz, CDCl$_3$, TMS scale): δ/ppm 27.3 (1,4; B_C), 32.5 (1,4; B_T), 34.2 (1; B_V), 43.6 (2; B_V), 114.3 (4; BV), 129.5 (2,3; BC), 129.9 (2,3; BT), 142.4 (3; BV).

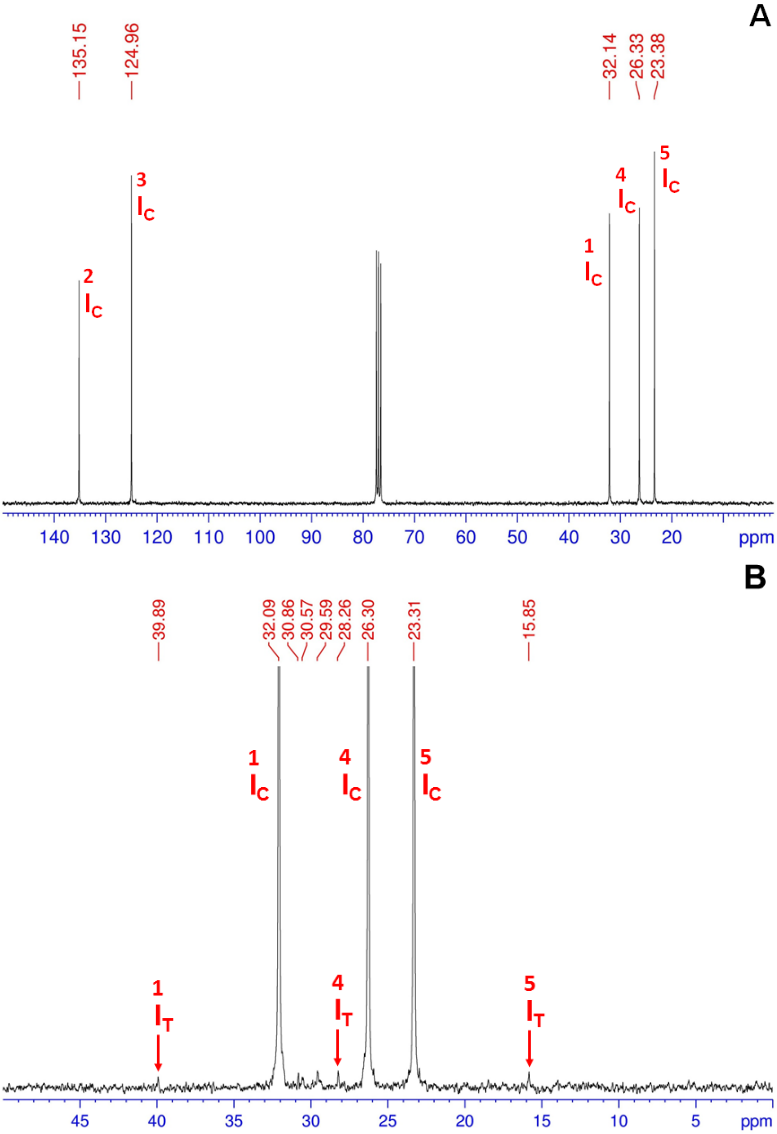

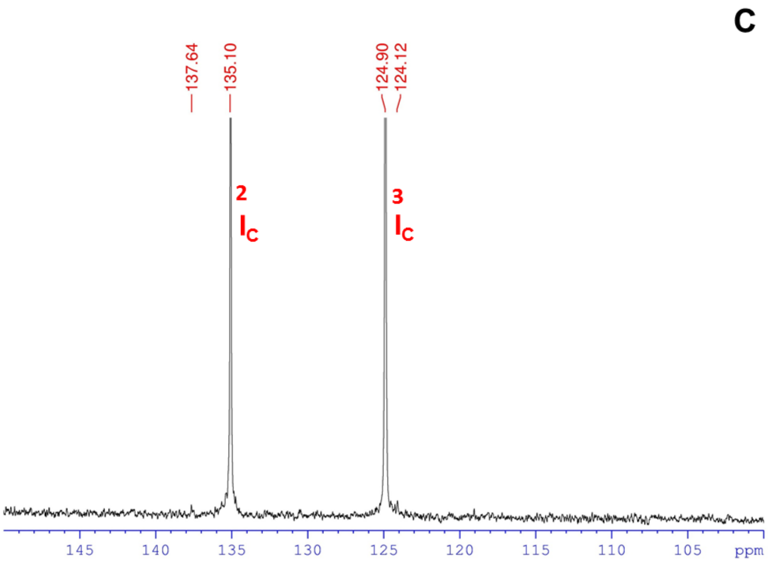

Fig. 6.2. ^{13}C-NMR spectra (100 MHz, in $CDCl_3$, TMS scale) of PIR: (A) entire spectrum, (B) saturated and (C) olefinic carbon regions.

PIR ^{13}C NMR analysis (100 MHz, CDCl3, TMS scale): δ/ppm 15.8 (5; I_T), 23.3 (5; I_C), 26.3 (4; I_C), 28.3 (4; I_T), 32.1 (1; I_C), 39.9 (1; I_T), 124.9 (3; I_C), 135.1 (2; I_C).

On the basis of the ^{13}C-NMR analysis of homopolymers, a high content of 1,4-*cis* units, B_c = 97 %mol. (B_T = 2 %mol.) and I_c = 94.5 %mol. (I_T = 5.5 %mol.), respectively and a content of 1,2 vinyl butadiene units, B_V = 1 %mol., have been evaluated.

The DSC heating scans of PBR and PIR are shown in **Fig. 6.3**. The glass transition temperatures of PBR and PIR were observed at -109 °C and -65 °C, respectively. A melting point due to the melting of the crystalline part in PBR was observed at -8 °C (melting enthalpy ΔH_m = 15 J/g).

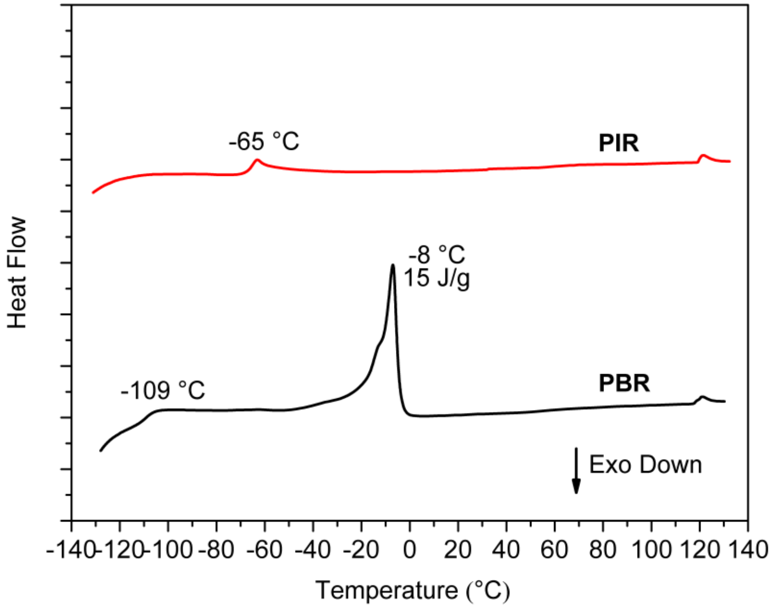

Fig. 6.3. DSC heating scans of PBR and PIR.

The GPC chromatograms of PBR and PIR solutions in THF are shown in **Fig. 6.4**. Both rubbers have a high number average molecular mass ($\overline{M}_n$ = 182 KDa for PBR and $\overline{M}_n$ = 376 KDa for PIR) and a broad molecular mass distribution ($\overline{M}_w / \overline{M}_n \approx 3$).

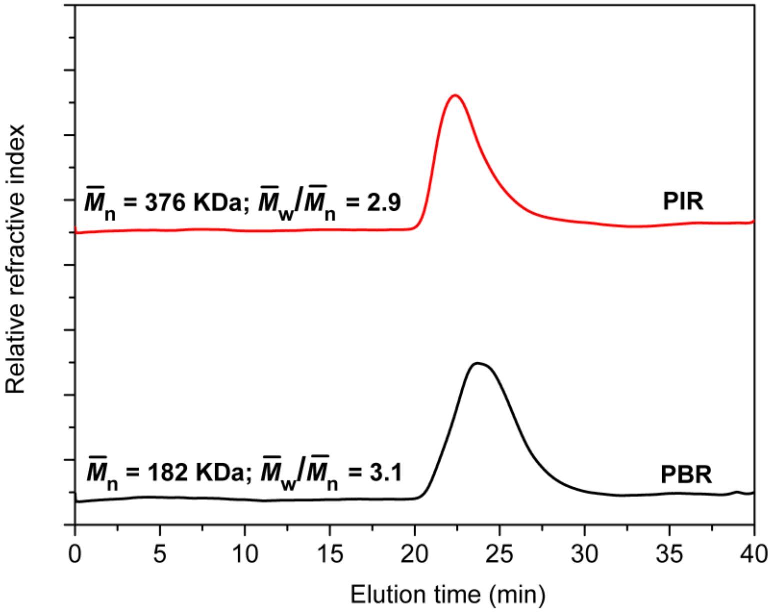

Fig. 6.4. GPC chromatograms of PBR and PIR solutions in THF.

6.2.2 Characterization of the PBR-PIR Copolymers

Grubbs and Hoveyda-Grubbs first generation catalysts, GI and HGI in **Fig. 5.3**, were found to promote the polymer-scrambling reaction by MCM of PBR and PIR, providing, preferentially, random PBR-PIR multiblock copolymers with high yields (for the experimental procedure see paragraph 8.18 in Section IV). The results of the characterization of PBR-PIR scrambled rubbers, obtained by MCM in the presence of GI, are reported in the following.

Tests were also performed on each homopolymer in presence of GI and it was verified that an appreciable degradation occurred only for PBR after 3h (from GPC measurements).

The DSC heating scans of PBR-PIR 50:50 (%wt.) blend and PBR-PIR scrambled rubbers at different times are shown in **Fig. 6.5**. In the case of PBR–PIR simple blend, the melting point of the crystalline part in PBR (-8 °C; ΔH_m = 15 J/g) and the T_gs of PBR (-109 °C) and PIR (-65 °C) were observed, indicating a biphasic mixture. After 1h, the melting endothermic peak of the PBR crystallites strongly decreased and completely disappeared after 3h, suggesting that the length of the main chain of PBR became shorter than that of PBR before the reaction, and that the crystallite size of PBR drastically decreased in the hybrid polymer. Additionally, as the reaction proceeded from 1h to 3h, the glass transition temperatures of PBR and PIR gradually approached the single T_g value of -87 °C, between the T_gs of each homopolymer. These results indicate that the polymer-scrambling reaction occurred to give a monophasic random multiblock copolymer. DSC heating scans of PBR-PIR scrambled rubbers at 8h and 24h remained substantially unaltered and similar to the result at 3h.

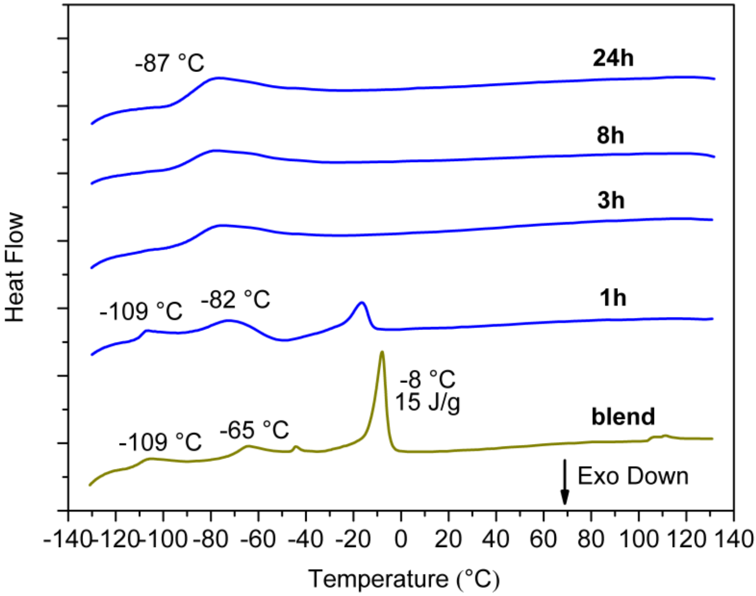

Fig. 6.5. DSC heating scans of PBR-PIR 50:50 (%wt.) blend and PBR-PIR scrambled rubbers prepared by MCM in presence of GI at different times.

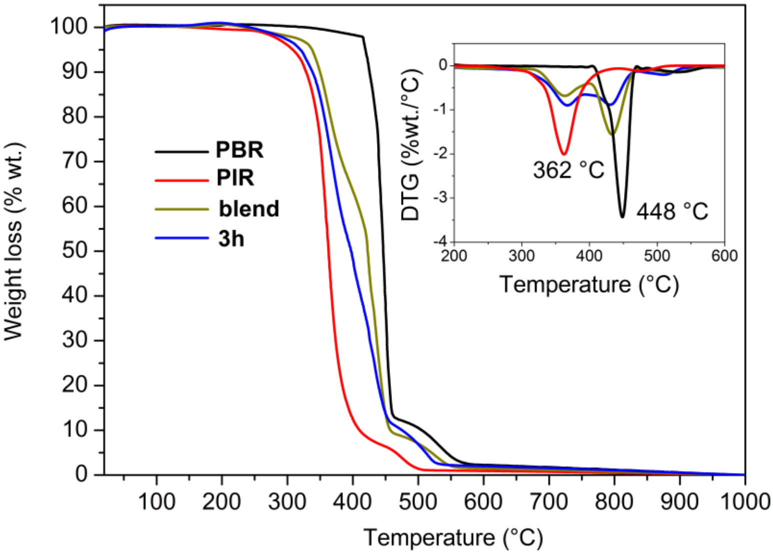

Fig. 6.6. TGA and DTG curves in air of PBR, PIR, PBR-PIR 50:50 (%wt.) blend and PBR-PIR scrambled rubber prepared by MCM in presence of GI at 3h.

TGA curves in air of PBR, PIR, PBR-PIR 50:50 (%wt.) blend and PBR-PIR scrambled rubber at 3h are shown in **Fig. 6.6**. PIR and PBR exhibit a single step weight loss, corresponding to a DTG maximum peak at 362 °C and 448 °C, respectively. TGA curve of PBR–PIR simple blend exhibit a clear double step weight loss, corresponding to the degradation of the separated PIR and PBR phases. The degradation process of the PBR-PIR scrambled rubber at 3h is definitely different with respect to the simple blend. It is composed by two steps with similar DTG peaks, attributed to the decomposition of PIR and PBR blocks within the monophasic copolymer. Furthermore, the residual mass at 1000 °C is nearly 0.3 %wt., so the ruthenium content in PBR-PIR scrambled rubber at 3h is negligible.

^{13}C-NMR measurements were carried out for PBR-PIR scrambled rubbers at 8h and are reported in **Fig. 6.7A–D**. Units are labelled according to **Scheme 6.4**.

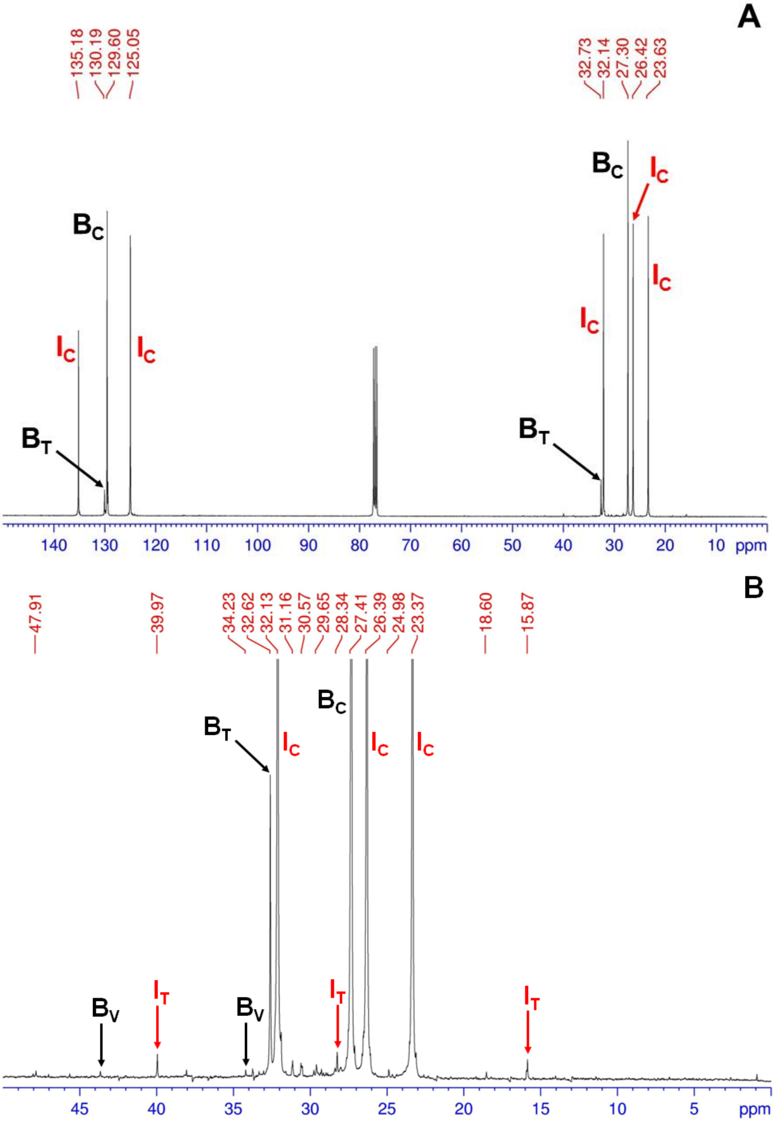

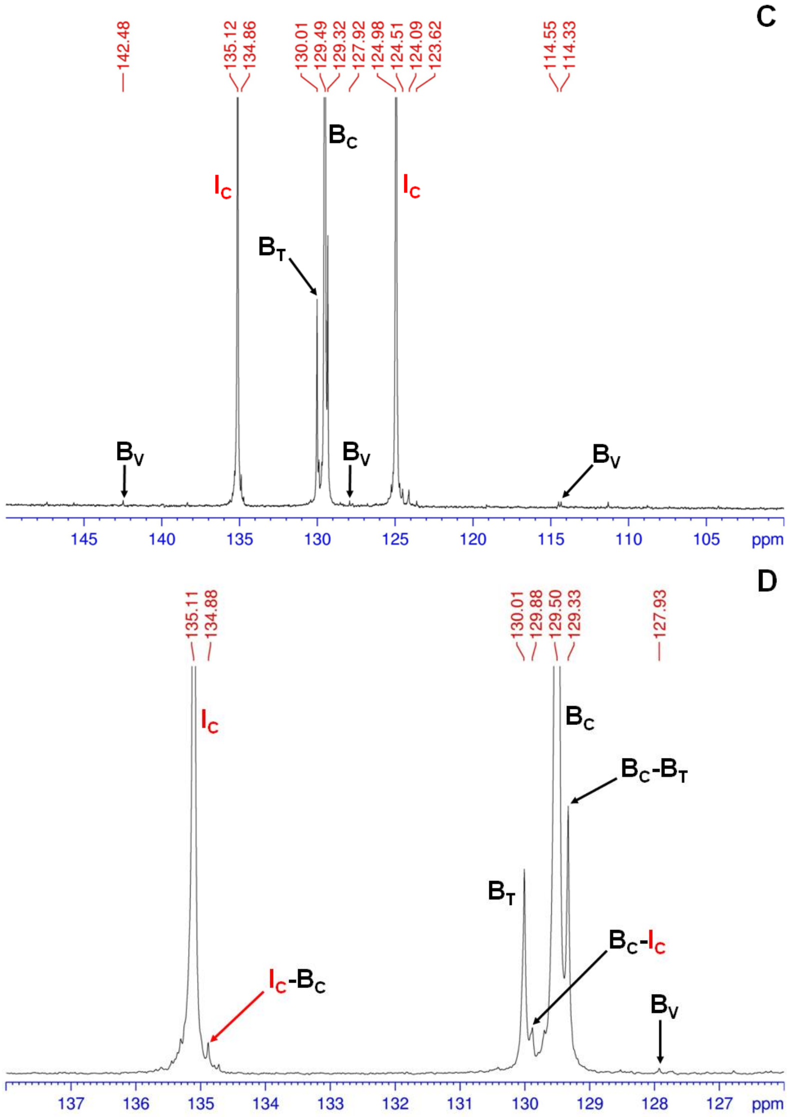

Fig. 6.7. ^{13}C-NMR spectra (100 MHz, in CDCl$_3$, TMS scale) of PBR–PIR scrambled rubber prepared by MCM in presence of G1 at 8h: (A) entire spectrum, (B) saturated and (C, D) olefinic carbon regions.

On the basis of the ^{13}C-NMR analysis of PBR-PIR scrambled rubbers at 8h, a composition I/B = 60:40 (%mol.), with a high content of 1,4-*cis* units, B_c = 35.8 %mol. (B_T = 3.7 %mol.) and I_c = 59.4 %mol. (I_T = 0.6 %mol.), respectively and a modest content of 1,2 vinyl butadiene units, B_V = 0.5 %mol., have been evaluated.

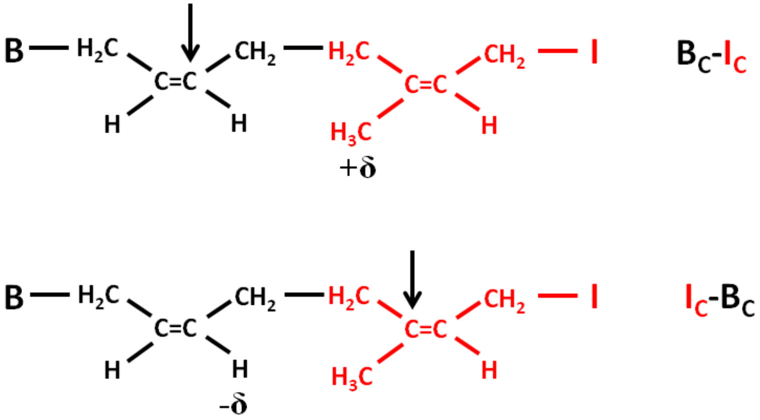

Scheme 6.5. Schematic representation of the observed 1,4-*cis* butadiene-isoprene heterosquences indicated in **Fig. 6.7D**.

The observed 1,4-*cis* butadiene-isoprene heterosquences are indicated in **Fig. 6.7D** and schematically represented in **Scheme 6.5**. The signals relative to the B_C and I_C homosequences are at 129.5 ppm and 135.1 ppm, respectively and both differ of 0.3-0.4 ppm with respect to the signals relative to the carbon in δ position at 129.9 ppm and 134.9 ppm, respectively. The signal at 129.3 ppm was attributed to B_C-B_T homosequences (see **Fig. 6.7D**).

The GPC chromatograms of solutions in THF of PBR-PIR 50:50 (%wt.) mixture and of PBR-PIR scrambled rubbers at different times are shown in **Fig. 6.8**. Bimodal profiles are obtained at each time, in particular a high molecular weight fraction at 23 min and a low molecular weight fraction at 34 min are observed. The amount of the low molecular weight fraction is enhanced after 24h, indicating that, as the metathesis reaction proceeded for long times, degenerative steps became predominant.

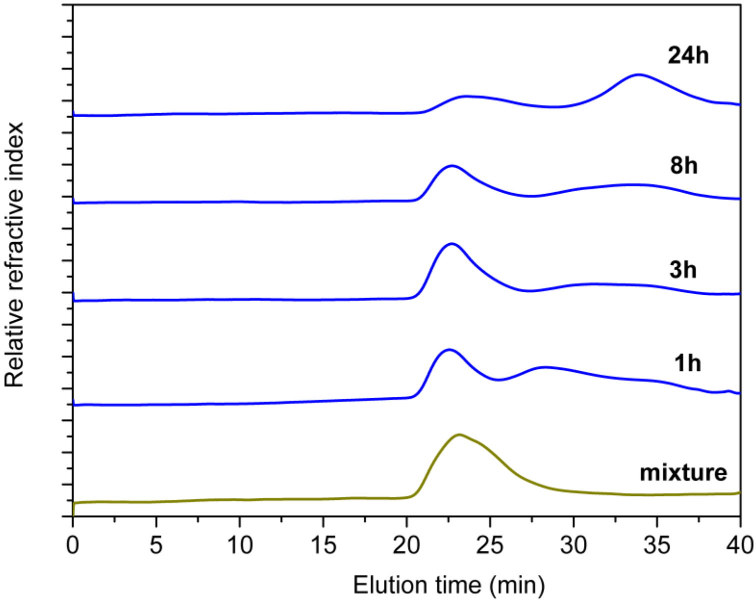

Fig. 6.8. GPC chromatograms of solutions in THF of PBR-PIR 50:50 (%wt.) mixture and PBR-PIR scrambled rubbers prepared by MCM in the presence of GI at different times.

6.2.3 Extraction of PBR-PIR Copolymers with Solvent

In order to separate the high molecular weight fraction, the PBR-PIR scrambled rubbers were treated in a Kumagawa extractor and ethyl acetate was allowed to reflux for 12 hours to remove the soluble low molecular weight components.

The GPC chromatograms of solutions in THF of PBR-PIR scrambled rubber at 3h and of the insoluble residue and the soluble extract after extraction in ethyl acetate for 12h are shown in **Fig. 6.9**.

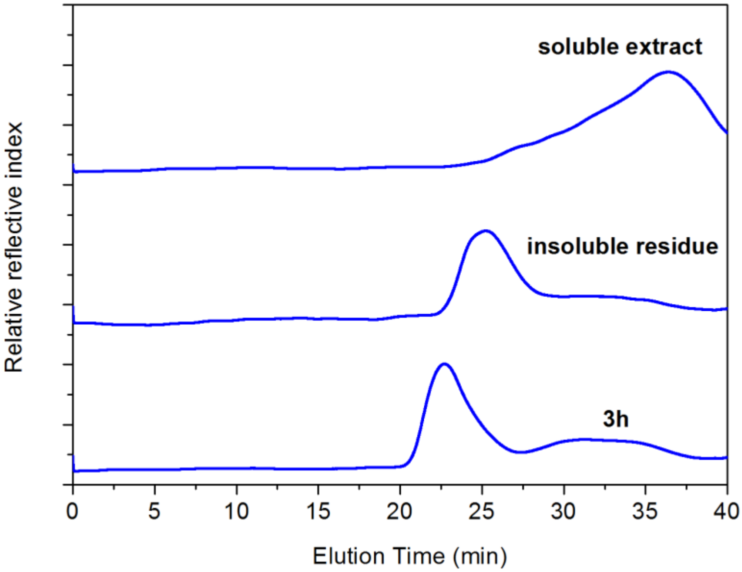

Fig. 6.9. GPC chromatograms of solutions in THF of PBR-PIR scrambled rubber prepared by MCM in presence of G1 after 3h, of the insoluble residue and of the soluble extract after extraction in ethyl acetate for 12h.

The insoluble residue clearly presents a monomodal GPC profile associated with a high molecular weight fraction at 25 min and a single T_g value at -77 °C, as observed from its DSC heating scan in **Fig. 6.10**. The soluble extract also exhibits a single T_g value at -84 °C.

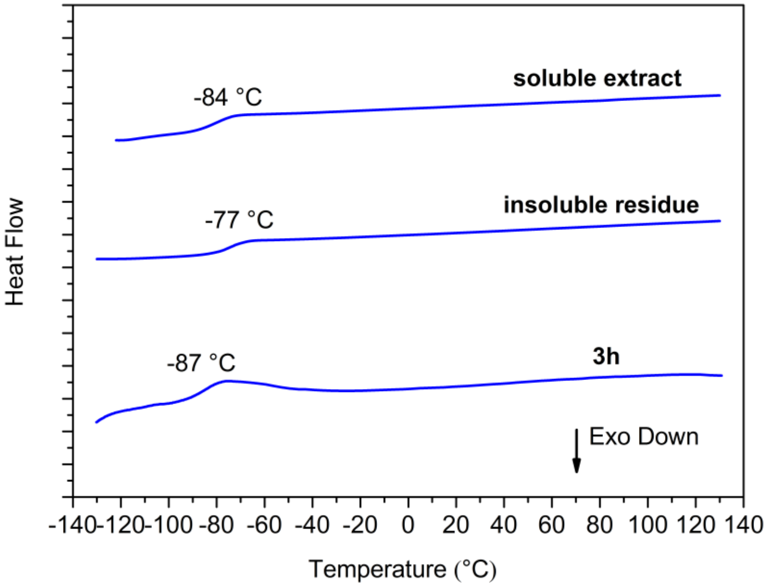

Fig. 6.10. DSC heating scans of PBR-PIR scrambled rubber prepared by MCM in presence of GI after 3h, of the insoluble residue and of the soluble extract after extraction in ethyl acetate for 12h.

Olefinic carbon regions of the ^{13}C-NMR spectra of the insoluble residue (**Fig. 6.11A**) and of the soluble extract (**Fig. 6.11B**) after extraction in ethyl acetate for 12h of PBR-PIR scrambled rubber, prepared by MCM in the presence of GI at 3h. The presence of long PBR and PIR homosequences at 124.8 ppm (I_C), 129.2 ppm (B_C–B_T), 129.4 ppm (B_C), 129.9 ppm (B_T), 135 ppm (I_C) together with signals of junctions of 1,4-*cis* butadiene-isoprene units at 129.8 ppm and 134.7 ppm are observed for both the insoluble residue and the soluble extract. These results indicate that, during the metathesis reaction in the presence of GI, high and low molecular weight fractions of PBR-PIR scrambled rubber are obtained. These fractions essentially differ for the content of I_C units.

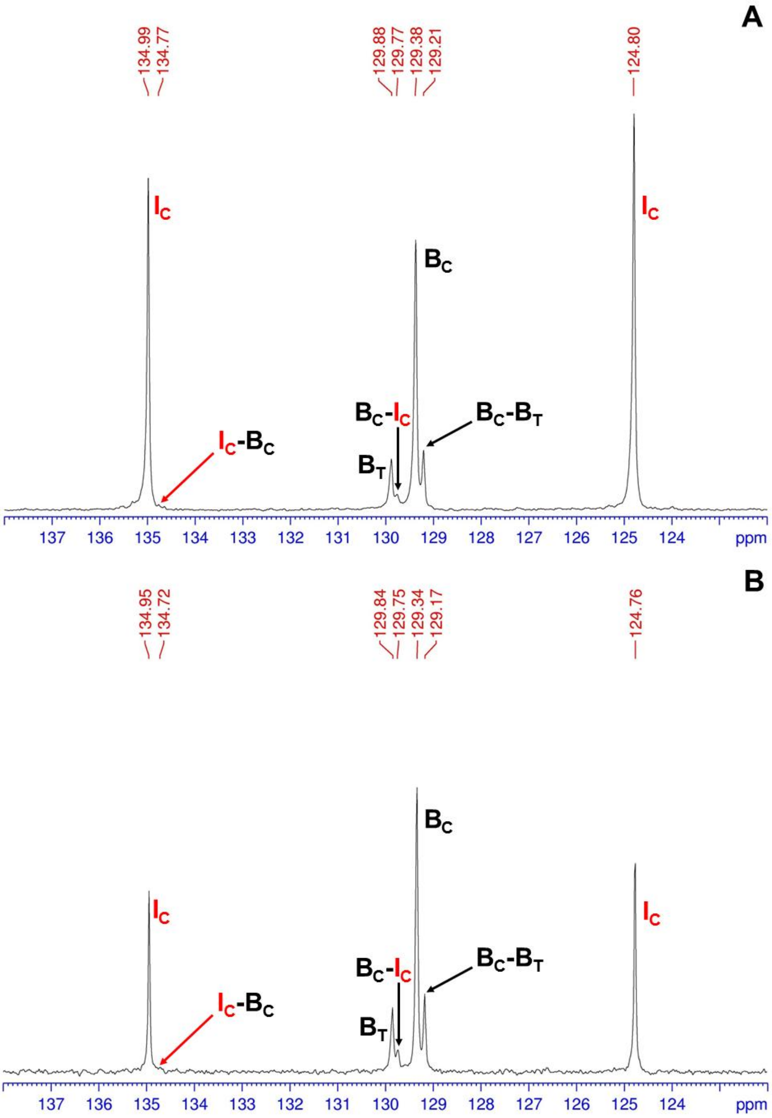

Fig. 6.11. ^{13}C-NMR spectra (100 MHz, in CDCl$_3$, TMS scale) in the olefinic carbon regions of (A) insoluble residue and (B) soluble extract, after extraction in ethyl acetate for 12h of PBR-PIR scrambled rubber, prepared by MCM in the presence of G1 at 3h.

High-*cis* random multiblock PBR-PIR copolymers were successfully prepared by MCM with first generation Grubbs and Hoveyda-Grubbs catalysts in dry hexane. From the viewpoint of both science and technology, the methodology shown here has a high content of innovation, infact it allows to prepare novel rubber materials, starting directly from the suitable commercial rubbers.

6.3 Metathetic Degradation of Rubbers

The metathetic degradation of polydienes was extensively investigated in the literature. Early pioneering studies by Alimuniar *et al.* [21] and Wagener *et al.* [22] on the ethenolysis of polyisoprenes noted the formation of ill-defined mixtures of partially-depolymerized rubber using tungsten-based olefin metathesis catalysts. Plenio and Wolf [23] reported the ethenolysis of natural rubber with second generation Grubbs catalysts, while several studies were conducted on the degradation of the natural rubber in presence of a second generation Grubbs catalysts and of a chain transfer agent, like *cis*-but-2-ene-1,4-diacetate [24] and terpenes, such as *d*-limonene [25] and β-pinene.[26] The degradation of polybutadiene by ADMET [27] and metathetic [28] depolymerizations, as well as the degradation of copolymers containing saturated and unsaturated units [29–32] were also reported.

In this contest, Grubbs and Hoveyda-Grubbs second generation catalysts, G2 and HG2 in **Fig. 5.3**, were found to preferentially degradate PBR-PIR mixtures (for the experimental procedure see paragraph 8.19 in Section IV). The results of the characterization of the metathesis products, obtained in the presence of G2, are reported in the following.

6.3.1 Degradation of Homopolymers

Degradation tests were first performed on each homopolymer in presence of G2 and the GPC chromatograms of solutions in THF of the metathesis products at different times are shown in **Figs 6.12** and **6.13**. In both cases, as the metathesis proceeded, the maxima of the GPC profiles shifted to higher elution times, particularly in the case of PBR (see **Fig. 6.12**), indicating a substantial reduction of the molecular masses ($\overline{M}_n$ = 10 KDa for PBR and $\overline{M}_n$ = 15 KDa for PIR at 24 h). These results indicate that the kinetics of degradation of PBR in presence of G2 is much faster than in the case of PIR.

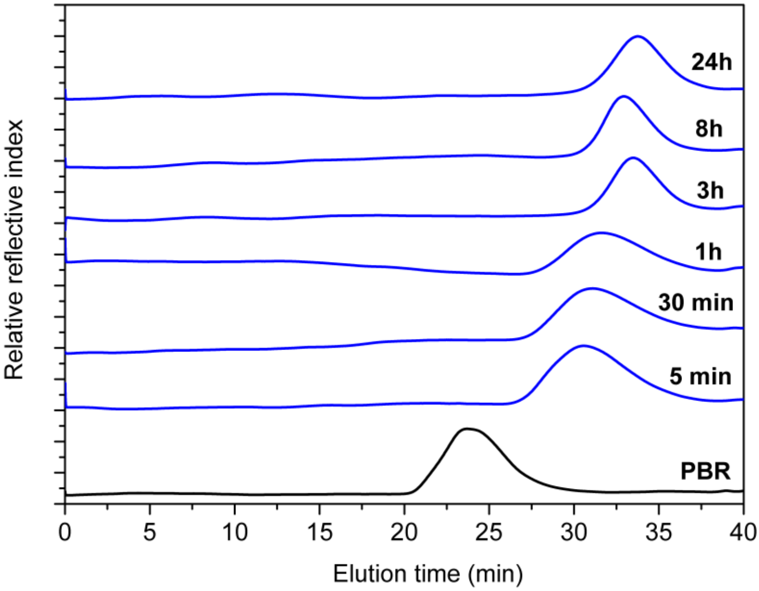

Fig. 6.12. GPC chromatograms of solutions in THF of PBR and the metathesis products, obtained in presence of G2, at different times.

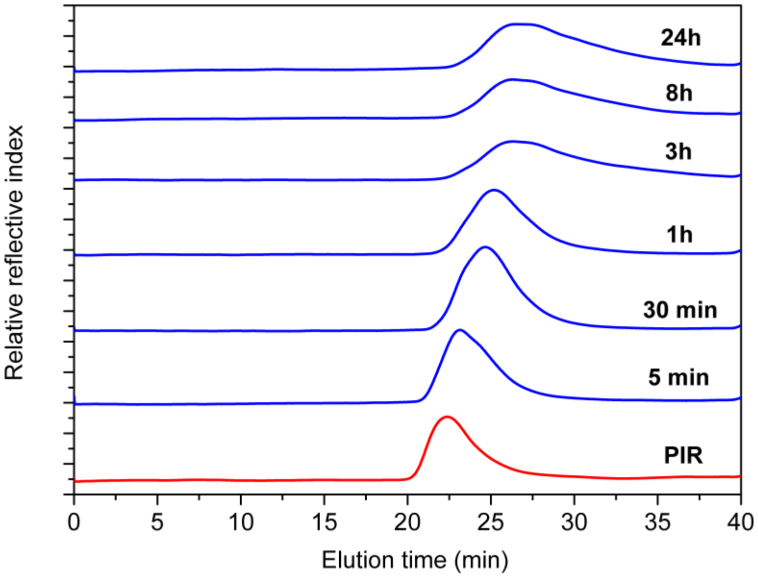

Fig. 6.13. GPC chromatograms of solutions in THF of PIR and the metathesis products, obtained in presence of G2, at different times.

6.3.2 Degradation of PBR-PIR Mixtures

A remarkable reduction of the molecular masses of the metathesis products, obtained from the PBR-PIR 50:50 (%wt.) mixture in presence of G2, is clearly noticeable from the GPC chromatograms at different times presented in **Fig. 6.14**. In particular, starting from a mixture of high molecular weight polymers ($\overline{M}_n$ = 182 KDa for PBR and $\overline{M}_n$ = 376 KDa for PIR, see also **Fig. 6.4**), oligomers with a strongly reduced molecular mass are obtained (the metathesis product at 24 h exhibits $\overline{M}_n$ = 9 KDa).

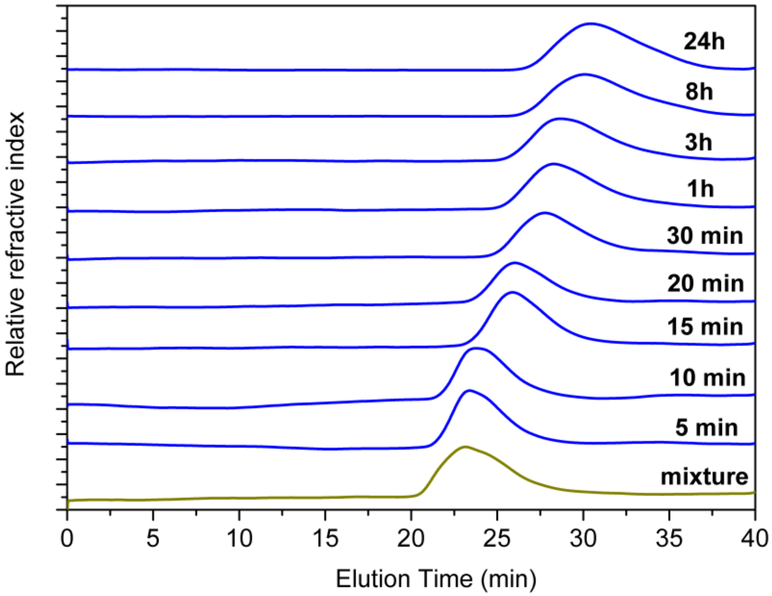

Fig. 6.14. GPC chromatograms of solutions in THF of PBR-PIR 50:50 (%wt.) mixture and of the metathesis products, obtained in the presence of G2, at different times.

A single value of T_g = -72 °C, close to the T_g value of PIR (-65 °C), is observed, at each reaction time, from the DSC heating scans of the metathesis products, obtained from the PBR-PIR 50:50 (%wt.) mixture in presence of G2 (see **Fig. 6.15**).

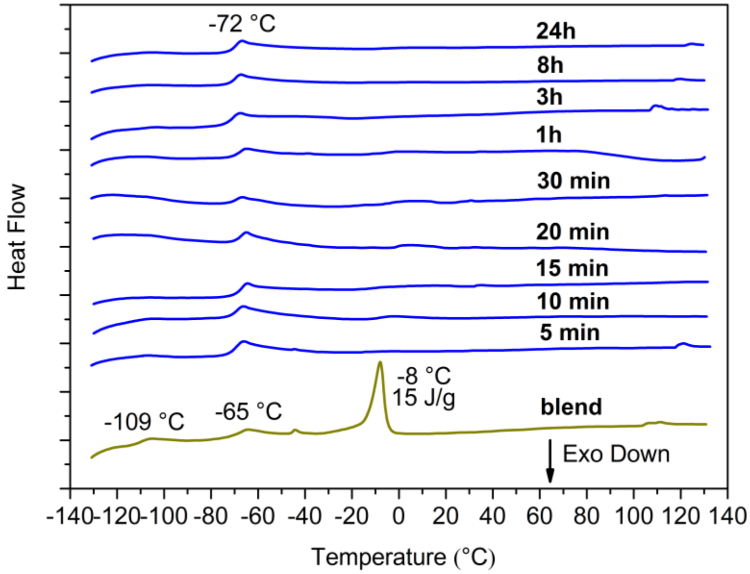

Fig. 6.15. DSC heating scans of PBR-PIR 50:50 (%wt.) blend and of the metathesis products, obtained in presence of G2, at different times.

A content of butadiene units of 14 %mol. was evaluated from the ^{13}C-NMR spectra of the PBR-PIR 50:50 (%wt.) mixture after 30 min of metathesis reaction with G2 in **Fig. 6.16A–B**, indicating that a considerable degradation of PBR occurs at relatively short times.

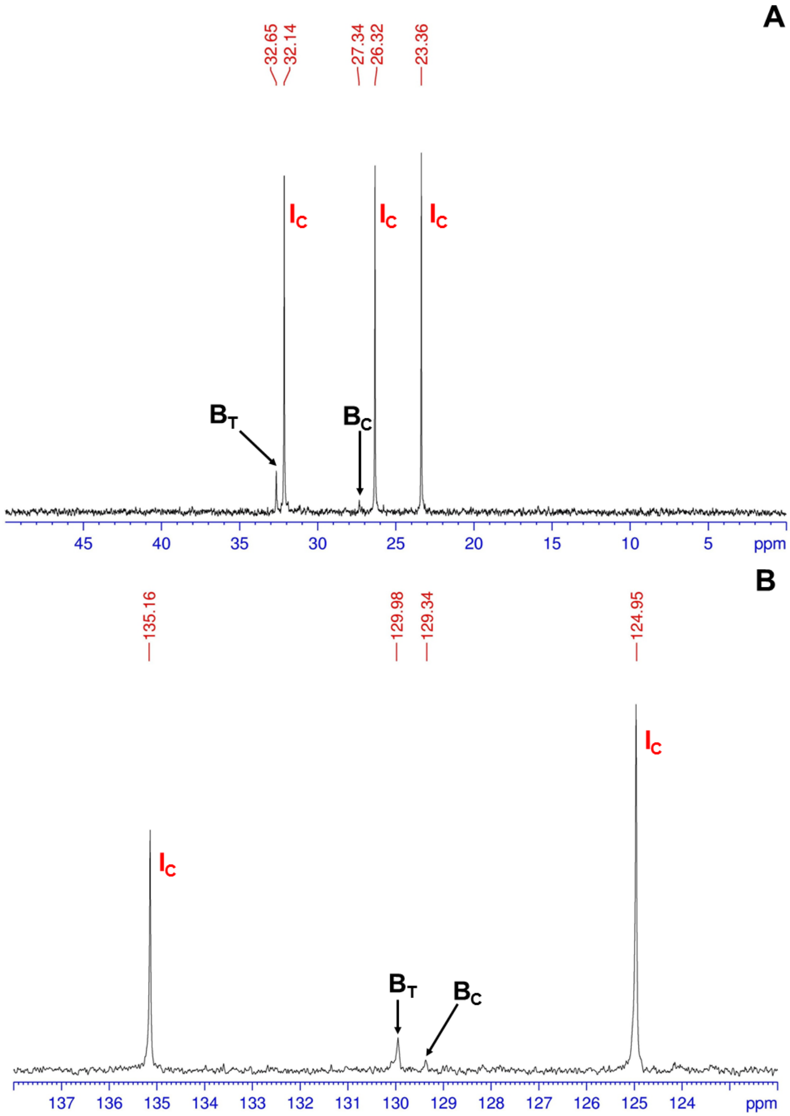

Fig. 6.16. ^{13}C-NMR spectra (100 MHz, in $CDCl_3$, TMS scale) of PBR-PIR 50:50 (%wt.) mixture after 30 min of metathesis reaction with G2: (A) saturated and (B) olefinic carbon regions.

Hence, the use of second generation Grubbs and Hoveyda-Grubbs catalysts was found to be detrimental for the obtainment of random multiblock copolymers of PBR and PIR by MCM, in fact, starting from mixtures of high molecular weight polymers, low molecular weight oligomers are obtained, as a consequence of metathetic degradative processes.

However, the importance of the metathetic degradation in rubber chemistry could be very remarkable, when depolymerization processes of high molecular weight rubbers are desidered, i. e. degradation of rubber parts of end-of-life tires.

References

[1] Y. X. Lu, F. Tournilhac, L. Leibler, Z. Guan. *J. Am. Chem. Soc.* **2012**, *134*, 8424–8427.

[2] H. Otsuka, T. Muta, M. Sakada, T. Maeda, A. Takahara. *Chem. Commun.* **2009**, 1073–1075.

[3] N. L. Wagner, F. J. Timmers, D. J. Arriola, G. Jueptner, B. G. Landes. *Macromol. Rapid. Commun.* **2008**, *29*, 1438–1443.

[4] D. J. Arriola *et al.* US 8048961 B2 Nov. 1, **2011**.

[5] J. R. Hagadorn *et al.* US 0245290 A1 Sep. 27, **2012**.

[6] J. L. White. Rubber Processing: Technology, Materials, Principles Hanser/Gardner Publications, Inc., **1995**.

[7] S. K. H. Thiele, D. R. Wilson, *J. Macromol. Sci. Part C: Polym. Rev.* **2003**, *43*, 581–628.

[8] G. Ricci, A. Sommazzi, F. Masi, M. Ricci, A. Boglia, G. Leone. *Coord. Chem. Rev.* **2010**, *254*, 661–676.

[9] A. Fischbach, R. Anwander. *Adv. Polym. Sci.* **2006**, *204*, 155–281.

[10] G. Ricci, L. Zetta, E. Alberti, T. Motta, M. Canetti, F. Bertini. *J. Polym. Sci. Part A* **2007**, *45*, 4635–4646.

[11] I. G. Hargis *et al.* US 4616065, **1986**.

[12] R. G. Newberg, H. Greenberg, T. Sato. *Rubb. Chem. Technol.*

1970, *43*, 333–355.

[13] A. He, B. Huang, S. Jiao, Y. Hu. *J. Appl. Polym. Sci.* **2003**, *89*, 1800–1807.

[14] Z. Shen, J. Ouyang, F. Wang, Z. Hu, F. Yu, B. Qian. *J. Polym. Sci. Polym. Chem. Ed.* **1980**, *18*, 3345–3357.

[15] L. Friebe, O. Nuyken, W. Obrecht. *Adv. Polym. Sci.* **2006**, *204*, 1–154.

[16] L. Porri, G. Ricci, N. Shubin. *Macromol. Symp.* **1998**, *128*, 53–61.

[17] H. L. Hsieh, H. C. Yeh. *Rubb. Chem. Technol.* **1985**, *58*, 117–145.

[18] Y. Hu, W. Dong, T. Masuda. *Macromol. Chem. Phys.* **2013**, DOI:10.1002/macp.201300383.

[19] T. M. Trnka, R. H. Grubbs. *Acc. Chem. Res.* **2001**, *34*, 18–29.

[20] K. Matsuzaki, T. Uryu, T. Asakura. NMR Spectroscopy and Stereoregularity of Polymers. *Japan Scientific Societies Press*, pp. 41–50, **1996**.

[21] A. Alimuniar, M. A. Yarmo, M. Z. A. Rahman, S. Kohjiya, Y. Ikeda, S. Yamashita. *Polym. Bull.* **1990**, *23*, 119–126.

[22] K. B. Wagener, R. D. Puts, D. K. Smith. *Makromol. Chem. Rapid Commun.* **1991**, *12*, 419–425.

[23] S. Wolf, H. Plenio. *Green Chem.* **2011**, *13*, 2008–2012.

[24] S. S. Solanky, I. Campistron, A. Laguerre, J. F. Pilard. *Macromol. Chem. Phys.* **2005**, *206*, 1057–1063.

[25] A. Martínez, S. Gutiérrez, M. A. Tlenkopatchev. *Molecules* **2012**, *17*, 6001–6010.

[26] S. Gutiérrez, M. A. Tlenkopatchev. *Polym. Bull.* **2011**, *66*, 1029–1038.

[27] J. Marmo, K. Wagener. *Macromolecules* **1995**, *28*, 2602–2606.

[28] M. Chasmawala, T. C. Chung. *Macromolecules* **1995**, *28*, 1333–1339.

[29] P. Thanki, D. Reyx, I. Campistron, A. Laguerre, R. P. Singh. *Eur. Polym. J.* **2004**, *40*, 2611–2616.

[30] K. L. Sedransk, F. C. Kaminski, L. R. Hutchings, G. D. Moggridge. *Polym. Degrad. Stab.* **2011**, *96*, 1074–1080.

[31] S. W. Craig, J. A. Manzer, E. B. Coughlin. *Macromolecules* **2001**, *34*, 7929–7931.

[32] F. Lucas, F. Peruch, S. Carlotti, A. Deffieux, A. Leblanc, C. Boisson. *Polymer* **2008**, *49*, 4935–4941.

Chapter 7

Grafting of Rubbers to Graphene Oxide Layers through Grubbs and Piers Catalyst-Functionalized Graphite Oxides

7.1 Covalent and Non-Covalent Functionalization of Graphene Oxide Layers with Grubbs and Piers Catalysts

The functionalization of graphene oxide layers using covalent or non-covalent approaches improves the dispersion of graphene oxide both in organic solvents and in bulk hydrophobic polymers, such as rubbers.[1]

The non-covalent functionalization of MMT and GO by intercalation of long-chain ammonium salts in their interlayer spaces (see paragraphs 1.2 and 2.5 in Section I) was already discussed (see Section II) to compatibilize such fillers with the rubber matrix.

A good filler dispersion within the polymer matrix generates an extended polymer-filler interface and strong interfacial interactions improve the stress transfer,[2] so the grafting of graphene oxide layers functionalized with metathesis catalysts to rubber chains is expected to combine the mechanical reinforcement with the improved dispersibility.

Grubbs catalyst-functionalized graphene oxide layers were prepared adapting the procedure reported by Longo *et al.* [3] for the covalent functionalization of multi-wall carbon nanotubes with Grubbs catalysts.

The covalent functionalization pathway of GO with G2 is showed in **Scheme 7.1** (for experimental details see paragraph 8.20

in Section IV). Carboxylic groups on GO sheets were first reacted with thionyl chloride, resulting in the corresponding acid chloride (GO-Cl), esterified with ethylene glycol (GO-Gly) and then reacted with 5-acid chloride 2-norbornene (GO-Nor). The metathesis reaction between GO-Nor and G2 produced Grubbs catalyst-functionalized graphene oxide layers (GO-G2).

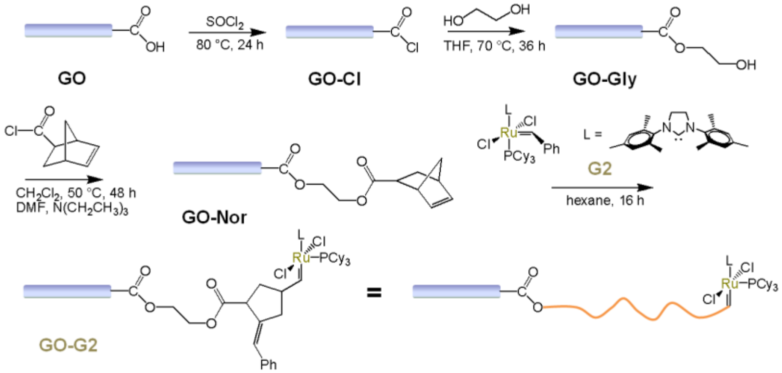

Scheme 7.1. Covalent functionalization pathway of graphite oxide with G2.

The whole functionalization process was followed by acquiring the FTIR spectra, presented in **Fig. 7.1**, of each intermediate product, from L-GO, used as the starting material, to the covalently functionalized graphene oxide layers with G2.

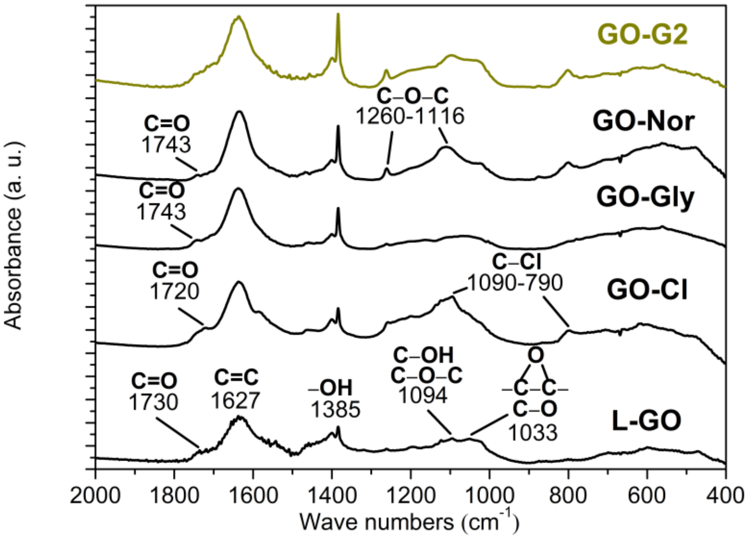

Fig. 7.1. FTIR spectra of: L-GO, the intermediate products of each functionalization step (GO-Cl, GO-Gly and GO-Nor) and the covalent functionalized graphene oxide layers with G2 (GO-G2).

The absorption peaks at 1090 cm^{-1} and 790 cm^{-1} (C-Cl stretchings) and the carbonyl peak at 1720 cm^{-1} confirm the formation of -COCl groups on graphene oxide layers. The shift of the position of the absorption band of the carbonyl groups at 1743 cm^{-1} and the absorption peaks at 1260 cm^{-1} and 1116 cm^{-1} (C-O-C stretching) confirm the esterification reactions with ethylene glycol and with 5-acid chloride 2-norbornene. Similar absorption peaks are present in the FTIR spectrum of GO-G2.

To give further insights regarding the structure of the covalently functionalized products, X-ray diffraction analysis was performed and the results are reported in **Fig. 7.2**.

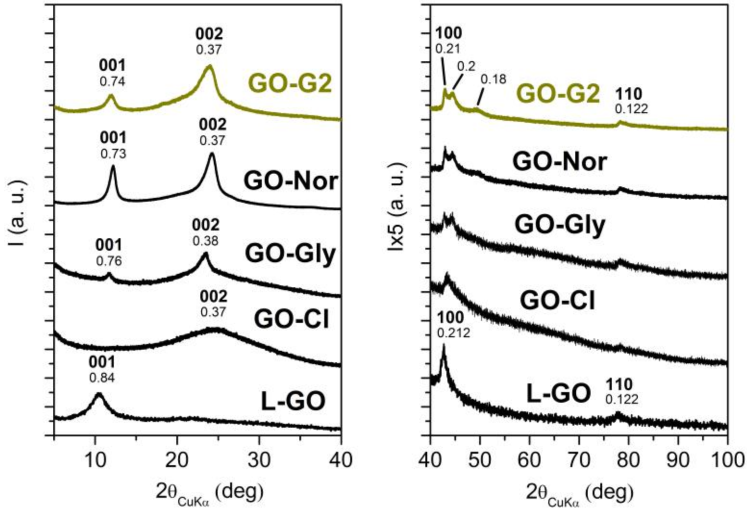

Fig. 7.2. X-ray diffraction patterns (Cu Kα) of: L-GO, the intermediate products of each functionalization step (GO-Cl, GO-Gly and GO-Nor) and the covalent functionalized graphene oxide sheets with G2 (GO-G2).

The treatment of L-GO with thionyl chloride causes the complete exfoliation of GO particles, in fact the pattern of GO-Cl in **Fig. 7.2** shows a very broad halo, centered at $d = 0.37$ nm with a correlation length of about 1 nm.

The reaction of GO-Cl with ethylene glycol, beside the formation of ester bonds (see FTIR spectra in **Fig. 7.1**), generates an ordered intercalate crystalline phase with periodicity $d = 0.76$ nm and a correlation length of about 16 nm.

Further treatments of GO-Gly with 5-acid chloride 2-norbornene (GO-Nor) and G2 (GO-G2), disturb the out-of-plane order of the intercalate crystalline phase ($D_\perp = 8$ nm in GO-G2), while maintaining about the same periodicity. This results are consistent with an intercalated structure with ethylene glycol, covalently functionalized at the edges and on the surfaces of the crystalline domains with G2.

As sketched in **Scheme 7.2**, a non-covalent functionalization of GO was also performed by an ion-exchange reaction of sodium cations of $GO^{-}Na^{+}$ with a phosphinated second generation Piers catalyst (PP2 in **Scheme 7.2**) [4] in water, according to the experimental procedure described in paragraph 8.21 in Section IV.

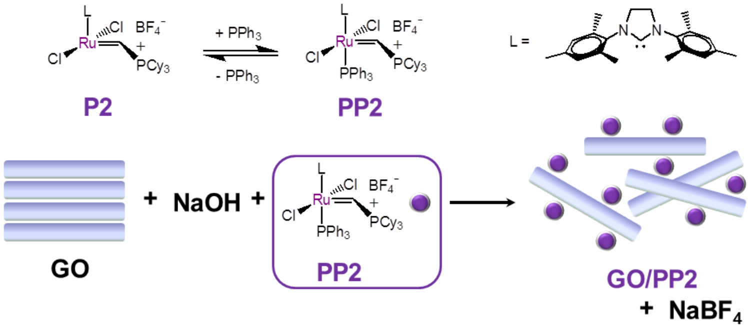

Scheme 7.2. Non-covalent functionalization pathway of graphite oxide with PP2.

Aiming to prevent the deactivation of the metathesis catalyst in aqueous medium a triphenylphosphine ligand was coordinated to the Ru metal center of P2, obtaining PP2. The shift in the position of the signal of the hydrogen bonded to the carbon of the alkylidene ligand from 17.8 ppm in the ^{1}H-NMR spectrum of P2 to 19.8 ppm in the ^{1}H-NMR spectrum of PP2 confirmed that the phosphination reaction successfully occurred.

During the ion-exchange reaction in water, the phosphonium substituent of the alkylidene ligand in PP2 allows to establish ionic interactions with basified GO sheets, that results completely exfoliated after the functionalization, as shown in the GO/PP2 diffraction pattern of **Fig. 7.3**.

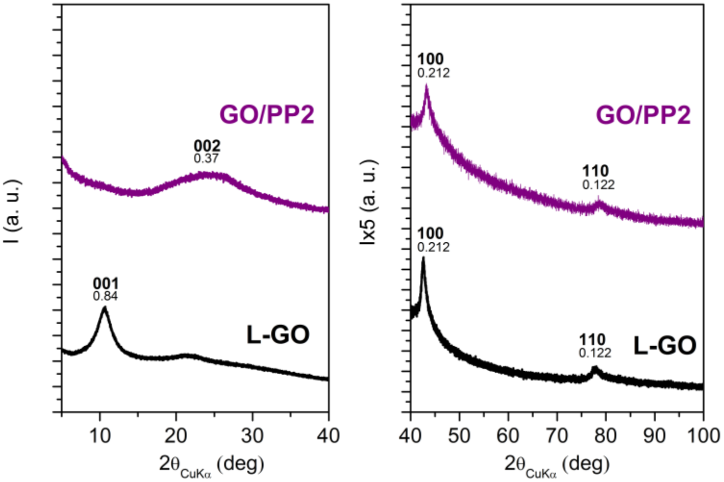

Fig. 7.3. X-ray diffraction patterns (Cu Kα) of: L-GO and the non-covalent functionalized graphene oxide sheets with PP2 (GO/PP2).

The TGA curves in air of GO-G2 and GO/PP2, compared with L-GO in **Fig. 7.4**, show a residual mass of 4.6 %wt. and 12.4 %wt. at 1000 °C, attributed to the formation of RuO_2. The amount of bonded ruthenium on GO-G2 and GO/PP2 was 3.5 %wt. and 9.4 %wt., as evaluated from simple stoichiometry calculations.

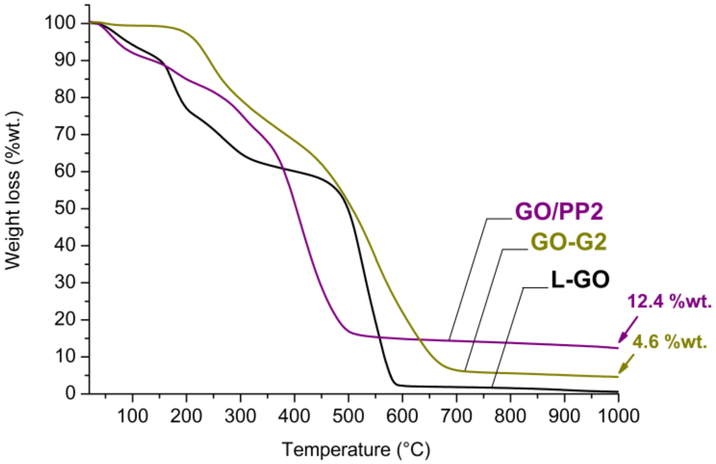

Fig. 7.4. TGA curves in air of L-GO, GO-G2 and GO/PP2.

The results in **Figs 7.1–7.4** confirm that both, the covalent and the non-covalent functionalization of GO were achieved.

7.2 Grafting Reactions of Polyisoprene to Graphene Oxide Layers

Polymer nanocomposites containing graphene oxide or reduced graphene oxide layers as fillers are commonly prepared by solution blending,[5–8] melt blending [9,10] and *in situ* polymerization.[11,12]

However, a very limited literature has investigated rubber nanocomposites filled with graphene oxide or reduced graphene oxide layers, prevailingly prepared by solution blending [13] or latex blending.[14–17]

It is widely acknowledged in the literature that there are two main methodologies for the covalent attachment of polymers to the surface of fillers, which are defined as "grafting to" and "grafting from" methods. The former relies on the covalent bond formation between the functional groups of a preformed polymer and the functionalities on the filler surface. The "grafting from" method, instead, is based on the covalent immobilization of the polymer precursors on the surface of the filler and subsequent propagation of the polymerization in the presence of monomeric species.[18]

In this paragraph, novel rubber nanocomposites, based on polyisoprene grafted to graphene oxide layers (PIR/GO), prepared by reacting PIR with the previously described GO-G2 and GO/PP2 (see the experimental procedure described in paragraph 8.22 in Section IV), are presented.

Plausible grafting mechanisms, according to the Chauvin mechanism of a common cross-metathesis reaction, are proposed in **Schemes 7.3** and **7.4**, for GO-G2 and GO/PP2 with a generic olefin-containing polymer.

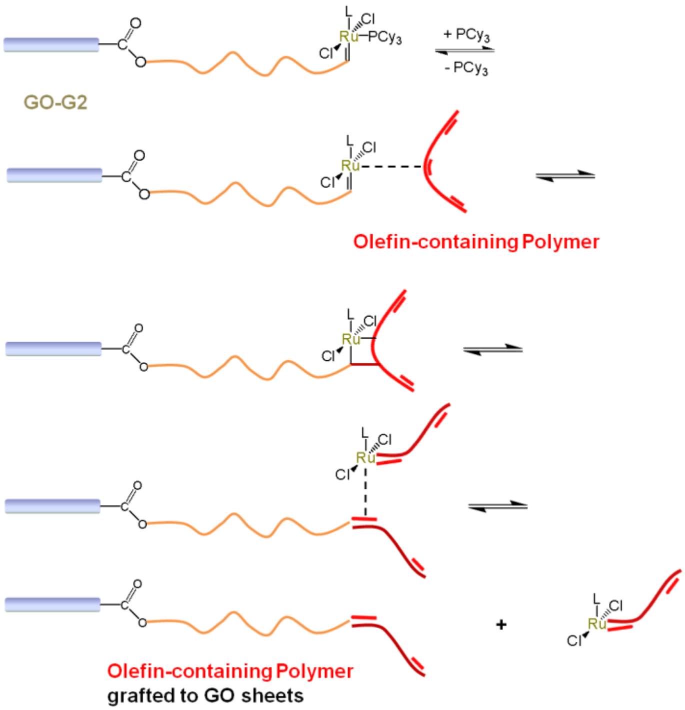

Scheme 7.3. Plausible grafting mechanism of an olefin-containing polymer with graphene oxide sheets in presence of GO-G2.

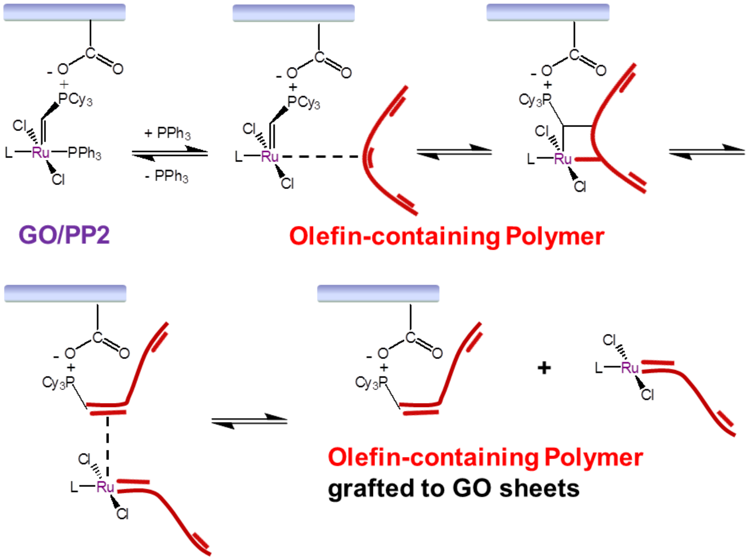

Scheme 7.4. Plausible grafting mechanism of an olefin-containing polymer with graphene oxide sheets in presence of GO/PP2.

After each reaction, the products were treated in a Kumagawa extractor and hexane was allowed to reflux for 12 hours to remove the free (soluble fraction) from the grafted polymer fraction (insoluble residue). The yields of the dried insoluble residues compared with the as prepared grafted rubbers were higher than 95 %wt. and 97 %wt. for PIR/GO composites obtained from GO-G2 and GO/PP2, respectively.

In the X-ray diffraction patterns of PIR/GO samples, obtained from GO-G2 and GO/PP2 in **Fig. 7.5**, the reflections of GO cannot be identified, suggesting that the graphene oxide layers are exfoliated in the polymer matrix, as result of the grafting process.

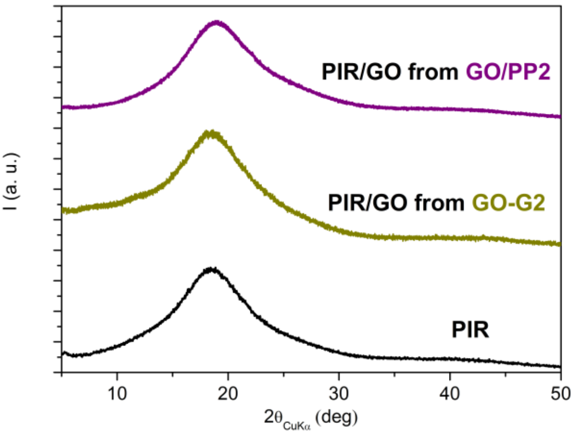

Fig. 7.5. X-ray diffraction patterns (Cu Kα) of: PIR and of PIR grafted to GO sheets (PIR/GO) obtained from PIR dispersions in hexane with 3% wt. of GO-G2 and GO/PP2, respectively.

As shown by the TGA curves in air of PIR/GO samples, obtained from GO-G2 and GO/PP2 in **Fig. 7.6**, the amount of residual RuO_2 at 1000 °C is negligible.

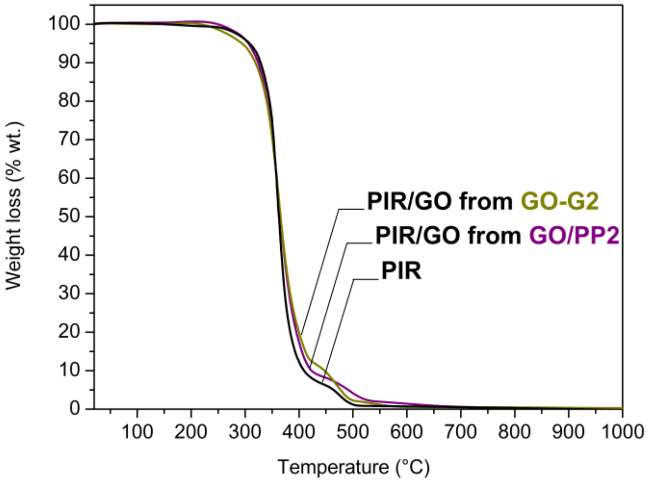

Fig. 7.6. TGA curves in air of: PIR and of PIR grafted to GO sheets (PIR/GO) obtained from PIR dispersions in hexane with 3%wt. of GO-G2 and GO/PP2, respectively.

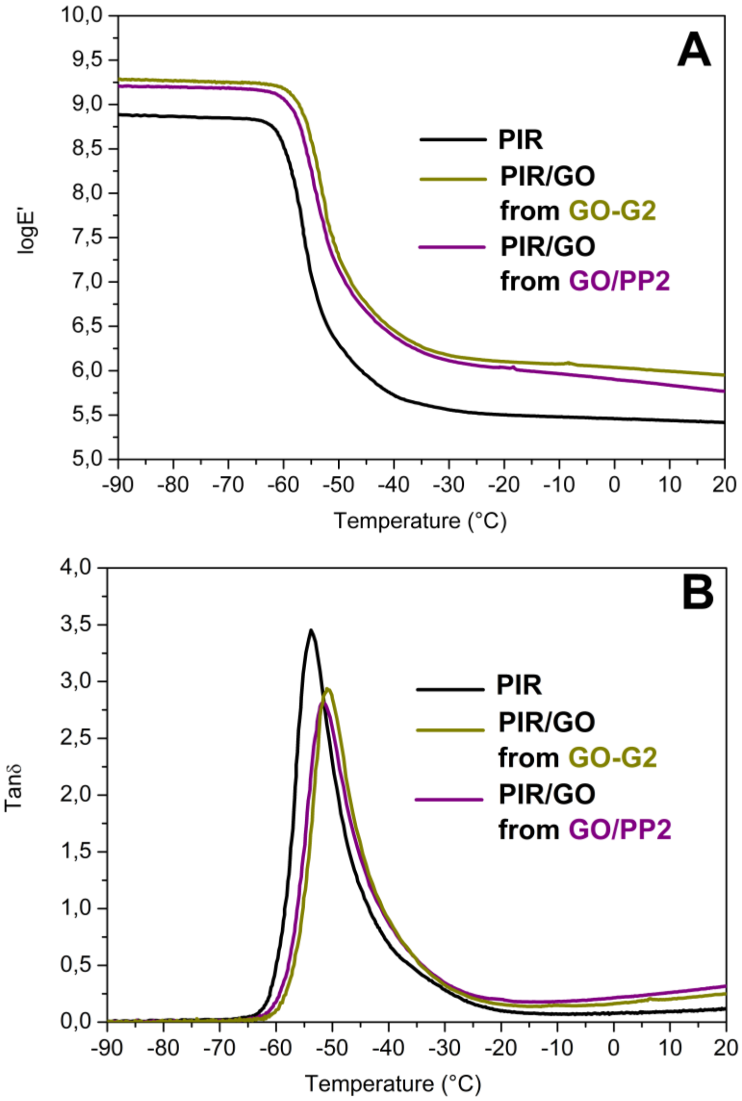

Fig. 7.7. (A) Logarithm of the tensile storage modulus, logE' and (B) loss tangent (tanδ) from -90 °C to 20 °C of: PIR and of PIR grafted to GO sheets (PIR/GO) obtained from PIR dispersions in hexane with 3% wt. of GO-G2 and GO/PP2, respectively. The spectra were recorded in the tensile mode.

Dynamic-mechanical analysis (DMA) of PIR/GO nanocomposites, compared with PIR, are shown in **Fig. 7.7**. PIR/GO nanocomposites show large increases in tensile storage moduli (logE') with respect to the neat PIR (**Fig. 7.7A**), particularly at 20 °C.

The peak temperatures of tanδ (**Fig. 7.7B**) were associated with the glass transition temperatures, in particular slight shifts of 2-3 °C were observed for PIR/GO nanocomposites compared with neat PIR. Moreover, PIR/GO nanocomposites show decreased tanδ peak height and breadth, suggesting strong interfacial bonding between the rubber matrix and graphene oxide layers. These results indicate the restriction of the motion of PIR chains due to the grafting reactions.

In summary, novel rubber nanocomposites, composed by PIR grafted to graphene oxide sheets, were prepared by taking advantage from the cross-metathesis reactions of PIR and functionalized GO samples with Grubbs and Piers catalysts.

Hence, it was here demonstrated that olefin metathesis represents a very powerful tool in rubber chemistry and more in general in polymer chemistry. In fact, it allows to obtain not only novel polymer-polymer materials, but also hybrid polymer-filler nanocomposites with suitably functionalized fillers. In addition, metathesis reactions are able to degradate polymers and copolymers with unsaturated groups.

References

[1] R. Sengupta, M. Bhattacharya, S. Bandyopadhyay, A. K. Bhowmick. *Progr. Polym. Sci.* **2011**, *36*, 638–670.

[2] J. N. Coleman, U. Khan, W.J. Blau, Y. K. Gun'ko. *Carbon* **2006**, *44*, 1624–1652.

[3] C. Costabile, F. Grisi, G. Siniscalchi, P. Longo, M. Sarno, D.

Sannino, C. Leone, P. Ciambelli. *J. Nanosci. Nanotech.* **2011**, *11*, 1–10.

[4] P. E. Romero, W. E. Piers, R. McDonald. *Angew. Chem. Int. Ed.* **2004**, *116*, 6287–6291.

[5] Y. X. Xu, W. J. Hong, H. Bai, C. Li, G. Q. Shi. *Carbon* **2009**, *47*, 3538–3543.

[6] D. Y. Cai, M. Song. *Nanotechnology* **2009**, *20*, 315708.

[7] D. Y. Cai, K. Yusoh, M. Song. *Nanotechnology* **2009**, *20*, 085712.

[8] Q. Wu, Y. X. Xu, Z. Y. Yao, A. R. Liu, G. Q. Shi. *ACS Nano* **2010**, *4*, 1963–1970.

[9] H. B. Zhang, W. G. Zheng, Q. Yan, Y. Yang, J. W. Wang, Z. H. Lu, G. Y. Ji, Z. Z. Yu. *Polymer* **2010**, *51*, 1191–1196.

[10] A. Dasari, Z. Z. Yu, Y. W. Mai. *Polymer* **2009**, *50*, 4112–4121.

[11] A. P. Yu, P. Ramesh, M. E. Itkis, E. Bekyarova, R. C. Haddon. *J. Phys. Chem. C* **2007**, *111*, 7565–7569.

[12] X. S. Zhou, T. B. Wu, B. J. Hu, G. Y. Yang, B. X. Han. *Chem. Commun.* **2010**, *46*, 3663–3665.

[13] X. Bai, C. Wan, Y. Zhang, Y. Zhai. *Carbon* **2011**, *49*, 1608–1613.

[14] Y. H. Zhan, J. K. Wu, H. S. Xia, N. Yan, G. X. Fei. *Macromol. Mater. Eng.* **2011**, *296*, 590–602.

[15] J. S. Kim, J. H. Yun, I. Kim, S. E. Shim. *J. Ind. Eng. Chem.* **2011**, *17*, 325–330.

[16] J. R. Potts, O. Shankar, L. Du, R. S. Ruoff. *Macromolecules* **2012**, *45*, 6045−6055.

[17] J. R. Potts, O. Shankar, S. Murali, L. Dub, R. S. Ruoff. *Compos. Sci. Technol.* **2013**, *74*, 166–172.

[18] D. Tasis, N. Tagmatarchis, A. Bianco, M. Prato. *Chem. Rev.* **2006,** *106*, 1105–1136.

Section IV

Experimental Part

Chapter 8

Materials and Preparation Procedures

8.1 Materials

Pristine sodium MMT was Dellite® HPS from Laviosa Chimica Mineraria S.p.A., with cationic exchange capacity (CEC) equal to 128 mmol/100 g.

The ammonium salt di(hydrogenated tallow)-dimethylammonium chloride was from Akzo Nobel, with Arquad® HC Pastilles as the trade name. The alkyl chain distribution was as follows (as %wt.): $< C_{12} = 1$, $C_{14} = 4$, $C_{16} = 31$, $C_{18} = 64$.

Dellite® 67G was based on MMT as inorganic silicate and was reported in the technical data sheets to have 40 - 45 %wt. as the organic modifier and an average dry particle size in the 7–9 μm range.

Stearic acid and glyceryl tristearate were from Aldrich. 2-stearamidoethyl stearate was from Abril with Abriflo 65 (Abril Industrial Waxes Ltd) as trade name.

The syndiotactic polystyrene (sPS) used in this study was manufactured by Dow Chemicals under the trademark Questra 101. ^{13}C nuclear magnetic resonance characterization showed that the content of syndiotactic triads [1] was over 98%. The mass average molar mass obtained by gel permeation chromotography (GPC) in trichlorobenzene at 135 °C was found to be $\overline{M}_w = 3.2 \times 10^5$ g mol^{-1} with a polydispersity index $\overline{M}_w / \overline{M}_n = 3.9$.

The A-F graphitic samples, listed in **Fig. 2.8** and **Table 2.1**, are the following: A and B are graphites (trade names Timrex C - Therm 011 / 012) from Timcal Graphite & Carbon; C is a ball-milled graphite (trade name Synthetic Graphite 8427®) from Asbury Graphite Mills Inc. D and E are coke and calcinated petroleum coke from Asbury carbons, respectively; F is carbon black N326 obtained from Cabot, with 30 nm as mean particle diameter of spherical primary particles, cetyl trimethylammonium bromide (CTAB) surface area of 85 m^2/g, iodine adsorption number of 84 g/Kg and dibutyl phthalate (DBP) adsorption number of 72 mL/100 g.

Synthetic 1,4-*cis*-polyisoprene was from Nizhnekamskneftechim Export, with trade name SKI3. Synthetic 1,4-*cis*-polybutadiene was from EniChem, with trade name S-0129.

Ingredients for compound preparation were: ZnO (Zincol Ossidi), stearic acid (Sogis), sulfur (Solfotecnica), N-dicyclohexylbenzothiazol-2-sulfenamide (DCBS; Flexsys), N-(1,3-dimethylbutyl)-N′-phenyl-1,4-benzenediamine (6PPD; Crompton), 3-octanoylthio-1-propyltriethoxysilane (NXT; Momentive) and dicumylperoxide (DCUP; Aldrich).

Nitric acid, sulfuric acid, sodium nitrate, potassium chlorate, potassium permanganate, hydrazine monohydrate (65 %), ascorbic acid, sodium hydroxide, hydrochloric acid, 1,2-dichlorobenzene (DCB), first and second generation Ru-based olefin metathesis catalysts (G1, G2, HG1, HG2 and P2), triphenylphosphine, thionyl chloride, dimethylformamide, triethylamine, ethylene glycol, 5-norbornene-2-carboxylic acid, methanol, ethanol, ethyl-vinyl ether, ethyl acetate, deuterated chloroform, deuterated dichloromethane, hexane, tetrahydrofuran (THF), sodium, benzophenone, dichloromethane (CH_2Cl_2), calcium hydride (CaH_2) were purchased from Sigma–Aldrich Company and were reagent quality. These products were used without further purification.

Hexane and THF were distilled from sodium/benzophenone. CH_2Cl_2 was dried on CaH_2 and freshly distilled before use.

8.2 Preparation of Organoclays

MMT was not dried prior to the synthesis of OC. The amount of H_2O in MMT was determined by TGA and it was taken into account for comparing the values of organic content in OC, theoretical and experimentally determined. The preparation of OCs was performed by the group of Prof. Maurizio Galimberti at the Polytechnic of Milan.

The solid state preparation of OCs, in absence or in presence of polar guest molecules, such as stearic acid (SA) or 2-stearamidoethyl stearate (SAES), was performed by the neat reaction of MMT and 2HT in a Centrifugal ball mill S 100 at 380 rpm for 1 h, followed by rotation in a 250 mL flask in air, utilizing a rotavapor at 100 °C. In any preparation the ammonium salt was used in a molar amount corresponding to the CEC of the MMT, while the polar guest substance was used in molar stechiometric amount respect to the ammonium salt. Just as an example, 10 g of MMT and 7.34 g of 2HT were ground in the ball milling to obtain the MMT/2HT organoclay, while MMT/2HT/SA and MMT/2HT/SAES organoclays were obtained by grinding the same amounts of MMT and 2HT, using 3.64 g of SA and 7.59 g of SAES, respectively.

8.3 Extraction of Organoclay with Ethyl Acetate

A standard procedure was adopted for the extraction of OC samples in **Fig. 1.7** with ethyl acetate. The extraction of commercial sample Dellite® 67 G is reported as example. 3 g of Dellite® 67G were placed in a Kumagawa extractor and ethyl acetate was allowed to reflux for 1 hour. A small amount of OC was taken and analyzed through TGA and WAXD analysis. The extraction was protracted to 2, 3, 4, 5, 6 hours and, at each step, a small sample of OC was taken and analyzed through TGA and WAXD analysis.

8.4 Clay Exfoliation by Supercritical CO_2

Exfoliated clay samples were obtained by using a SFX 200 supercritical carbon dioxide extractor (ISCO Inc.). Organically modified clays (typically 10 mg in a 20 mL stainless steel vessel) were processed in $scCO_2$ at 40 °C and 200 bar, for 16 h and 32h under quiescent conditions, in order to promote the diffusion of the supercritical fluid into the clay interlayer space. The system was then rapidly depressurized to atmospheric pressure and the expansion of the $scCO_2$ between the layers caused the clay exfoliation. This procedure was elaborated and performed in collaboration with Dr. Simona Longo of the Department of Chemistry and Biology of the University of Salerno.

8.5 Preparation of sPS/Clay Gels and Aerogels

Dispersions of the clays in DCB were obtained with both as received and exfoliated samples. A clay dispersion was initially prepared by adding the appropriate clay amount in 5 ml of DCB. The mixtures were homogenized for 1 h under magnetic stirring and sonicated in a 5000 mL batch bath ultrasound (Badelin Sonorex RK 1028 H) for 1 h. The preparation of sPS/clay gels and aerogels was performed in collaboration with Dr. Simona Longo of the Department of Chemistry and Biology of the University of Salerno.

sPS/clay gels were prepared, in hermetically sealed test tubes, by heating the clay dispersions above the boiling point of the solvent until complete dissolution of the polymer and the appearance of a transparent and homogeneous solution had occurred. The hot solution was then cooled to room temperature, where gelation occurred. For instance, 655 mg of sPS and 5 mL of 2 %wt. clay dispersion were mixed to obtain clay gels. The overall amount of polymer and clay in the gels was generally fixed to 10 %wt.

Aerogels were obtained by treating sPS/clay gels with a SFX

200 supercritical carbon dioxide extractor (ISCO Inc.) using the following conditions: 40 °C, 200 bar, extraction time 6 h. The prepared s-PS/clay aerogels present a weight composition ranging between 96/4 and 50/50. The aerogels, as prepared from gels with an overall polymer-clay content of 10 %wt., present a porosity close to 90 %.

For monolithic aerogels with a regular cylindrical shape, the total porosity can be estimated from the mass/volume ratio of the aerogel. Then, the percentage of porosity P of the aerogel samples can be expressed as:

$$P = 100 * [1 - (\rho_{app} / \rho_{pol})] \qquad (1)$$

where ρ_{pol} is the density of the polymer matrix and ρ_{app} is the aerogel apparent density calculated from the mass/volume ratio of the monolithic aerogels.

8.6 Preparation of GO with Higher Content of Oxygenated Groups

A 2000 mL three-neck round bottomed flask was flushed with gaseous N_2 and was then immersed into an ice bath.[2] 33 mL of nitric acid and 67 mL of sulfuric acid were fed to the flask under nitrogen and were then stirred obtaining a homogenous mixture. After introducing 5 g of graphite powder under vigorous agitation, 42 g of potassium chlorate was then added very slowly, to minimize the risk of explosion. The reaction mixturewas stirred for 120 h at room temperature. The resulting dark green suspension was poured into a large amount of a 5 %wt. HCl aqueous solution. Centrifugation was then performed at 10000 rpm for 15 min using a Hermle Z 323 K centrifuge. The isolated GO powder was washed twice with 100 mL of a 5 %wt. HCl aqueous solution and subsequently with deionized water. Finally, it was dried at 60 °C for

12 h in an oven.

8.7 Preparation of GO with Lower Content of Oxygenated Groups

120 mL of sulfuric acid and 2.5 g of sodium nitrate were introduced into a 2000 mL three-neck round bottomed flask immersed into an ice bath and 5 g of graphite were added, under nitrogen, with a magnetic stirring.[3] After obtaining a uniform dispersion of graphite powder, 15 g of potassium permanganate were added very slowly to minimize the risk of explosion. The reaction mixture was thus heated to 35 °C and stirred for 24 h. The resulting dark green slurry was first poured into a copious amount of deionized water, and then centrifugated at 10000 rpm for 15 min with a Hermle Z323 K centrifuge. The isolated GO powder was washed twice with 100 mL of a 5 %wt. HCl aqueous solution and subsequently with deionized water. Finally, it was dried at 60 °C for 12 h in an oven.

8.8 Preparation of GOICs

Intercalates with 2HT were prepared in analogy with the procedure reported by Matsuo *et al.* for graphite oxide intercalation compounds with quaternary alkylammonium or alkylpyridinium ions, containing one long hydrocarbon chain.[4] GO powders (100 mg) were dispersed in 0.05 M NaOH solution (20 mL), 2HT (420 mg; 100% CEC) aqueous solution (100 mL) was added in this dispersion and the reaction mixture was stirred at 40 °C for 12 h. The slurry was centrifugated at 10000 rpm for 15 min and the precipitate was washed with deionized water and dried at 60 °C for 12 h in an oven. 280 mg of GO/2HT-L powders were obtained, without any loss of GO.

Analogous intercalates were prepared by adding an excess of 2HT (typically 840 mg; 200% CEC) aqueous solution (100 mL). 320 mg of GO/2HT-H powders were obtained, without any loss of GO.

Intercalates were also prepared by adding SAES (390 mg; corresponding to molar ratio 2HT/SAES = 1:1) alcoholic solution (100 mL ethanol) in the reaction mixture containing the GO dispersion and the 2HT aqueous solution, as reported above. 430 mg of GO/2HT/SAES powders were obtained, without any loss of GO.

More ordered intercalates were prepared by adding GTS (640 mg; corresponding to molar ratio 2HT/GTS = 1:1) alcoholic solution (100 mL ethanol) in the reaction mixture containing the GO dispersion and the 2HT aqueous solution, as reported above. 440 mg of GO/2HT/GTS powders were obtained, without any loss of GO.

8.9 Preparation of GO and GOIC films

Dispersions of GO in deionized water (5 mg/mL) and of GOIC in a mixture of cyclohexane (5 mg/mL) were subjected to sonication in 10 L batches bath ultrasound (Badelin Sonorex RK 1028 H) for 30 min. The dispersions were cast in a Petri dish at 50 °C and ~ 30 μm thick films were obtained.

8.10 Preparation of Chemically Reduced Graphite Oxide

GO powders were chemically reduced using hydrazine monohydrate as reducing agent.[5] 3g of GO were placed in a 4000 mL three-neck flask and then 3000 mL of deionized water were added, till the complete dispersion of the GO powders in water. 30 mL of hydrazine monohydrate were added to the GO dispersion and the mixture was allowed to react under agitation at 80 °C for 24 h. The CRGO powders slowly precipitated as a black solid. This product was, then, centrifugated, washed with deionized water (2x100 mL) and finally dried at 60 °C for 12 h in an oven.

Chemical reduction of GO was also performed using ascorbic acid.[6] 0.5 g of GO were placed in a 200 mL three-neck flask and then 50 mL of deionized water were added, till the complete dispersion of the GO powders in water. 0.5 g of ascorbic acid were added to the GO dispersion and the mixture was allowed to react under agitation at 100 °C for 24 h. The CRGO powders slowly precipitated as a black solid. This product was, then, centrifugated, washed with deionized water and finally dried at 60 °C for 12 h in an oven.

8.11 Graphite Oxide Exfoliation by Ball-Milling

GO powders were introduced in 125 mL ceramic jars (inner diameter of 75 mm) together with stainless steel balls (10 mm in diameter) and were dry-milled in a planetary ball mill (Retsch GmbH 5657 Haan) for 2 h with a milling speed of 500 rpm and a ball-to-powder mass ratio of 10 to 1.

8.12 Solvo-thermal Reduction of Graphite Oxide

Reduced graphite oxide (rGO) dispersions were obtained by adding the appropriate GO amount in 5 mL of DCB, following by solvothermal reduction of GO in a 5000 mL batch bath ultrasound (Badelin Sonorex RK 1028 H) at 100 °C for 2h. This procedure was elaborated and performed in collaboration with Dr. Simona Longo of the Department of Chemistry and Biology of the University of Salerno.

8.13 Preparation of sPS/rGO Gels and Aerogels

The preparation of sPS/rGO gels and aerogels was performed in collaboration with Dr. Simona Longo of the Department of Chemistry and Biology of the University of Salerno. sPS/rGO gels were prepared, in hermetically sealed test tubes, by heating the rGO dispersions above the boiling point of the solvent until complete dissolution of the polymer and the appearance of a homogeneous solution had occurred. The hot solution was then cooled to room temperature, where gelation occurred. The overall amount of polymer and rGO in the gels was generally fixed to 10 %wt.

Aerogels were obtained by treating sPS/rGO gels with a SFX 200 supercritical carbon dioxide extractor (ISCO Inc.) using the following conditions: 40 °C, 200 bar, extraction time 6 h. The prepared sPS/rGO aerogels present a weight composition ranging between 95/5 and 50/50. The aerogels, as prepared from gels with an overall polymer-rGO content of 10 %wt., present a porosity close to 90 %.

8.14 Preparation Organoclays in Rubber Medium

The preparation of OCs in rubber medium was performed by the group of Prof. Maurizio Galimberti at the Polytechnic of Milan. A Brabender with a 50 mL mixing chamber was used as the internal mixer for the preparation of nanocomposites and the following standard procedure was adopted. 37.5 grams of PIR were introduced into the mixer at 80 °C and masticated for 1 min. 2.60 grams of MMT (6.92 phr hundred parts of rubber) and an amount of 2HTCl corresponding to the CEC of MMT (5.08 phr per hundred parts of rubber) were added, in presence of in absence of SA or SAES equal to the molar amount of 2HTCl. Mixing was carried out for 5 min, with rotors rotating at 60 rpm and with an initial temperature of about 100 °C. Nanocomposites were finally homogeneized by passing them 5 times on a two roll mill operating at 50 °C, with the front roll rotating at 30 rpm and the back roll rotating at 38 rpm, and 1 cm as the nip between the rolls.

8.15 Preparation of Rubber/Organoclay Nanocomposites by Melt Blending

The preparation of rubber/OC nanocomposites by melt blending was performed by the group of Prof. Maurizio Galimberti at the

Polytechnic of Milan. A Haake PolyLab with a 180 mL mixing chamber was used as the internal mixer for the preparation of nanocomposites. The following standard procedure was adopted for the preparation of nanocomposites whose formulations are reported in **Table 3.1**. Extracted OC, MMT/2HT and MMT/2HT/SA of paragraph 8.2 were selected as the starting OCs and are renamed as OC 2.5nm, OC 4nm and OC 6nm in the following. PIR was introduced into the mixer at 80 °C and masticated for 1 min. The nanofiller (either OC 2.5nm or OC 4nm or OC 6nm) was added and mixing was carried out for 5 min. The masterbatch was discharged at a temperature in a range from 110 °C to 115 °C and fed again to the mixer after 16 h, leaving it in the mixer at 60 °C and 30 rpm for 1 min. DCUP was then added, and mixing was performed for further 2 min. Compounds were finally homogeneized by passing them 5 times on a two roll mill operating at 50 °C, with one roll rotating at 38 rpm and the other at 30 rpm, and 1 cm as the nip between the rolls.

8.16 Preparation Rubber/Graphite Oxide Intercalation Compound Nanocomposites by Melt Blending

The preparation of rubber/GOIC nanocomposites by melt blending was performed by the group of Prof. Maurizio Galimberti at the Polytechnic of Milan. PIR-based nanocomposites containing different amounts of GO/2HT-H or GO/2HT-L were prepared in an internal mixer Brabender type with a 50 mL mixing chamber. Their formulations are reported in **Table 4.1** and their acronyms indicate both type and amount of filler; for example, in PIR/H-7 and in PIR/L-7, 7 parts per hundred parts of rubber (phr) of GO/2HT-H and 7 phr of GO/2HT-L were used, respectively. A standard procedure was adopted. PIR/H-7 of **Table 4.1** is taken as an example. 32.5 g of PIR were introduced into the mixer at 80 ° C and masticated for 1 min. 2.3 g (7 phr) of GO/2HT-H and 0.23 g of silane NXT, corresponding to 10 %wt. with respect to GO/2HT-H, were added. Mixing was carried out for 5 min at 60 rpm and then the compound was discharged at about 100 °C. After reaching room temperature, the compound was fed again to the mixer, ZnO, SA, and 6PPD were then added, and mixing was performed for further 2 min. Sulfur, DCBS, and CTP were finally added and the compound was discharged at about 60 °C after 2 further min of mixing. Nanocomposites were finally homogeneized by passing them five times on a two roll mill operating at 50 °C; one roll rotated at 38 rpm, the other at 30 rpm, and 1 cm was the nip between the rolls.

8.17 Crosslinking of Rubber Nanocomposites

All rubber nanocomposites were crosslinked by the group of Prof. Maurizio Galimberti at the Polytechnic of Milan. Crosslinking reaction was performed at 170 °C for 20 minutes, by compressing samples in discs. MDR rheometric analysis was conducted using a Monsanto MDR rheometer, the test being carried out at 170 °C, for 20 minutes, at an oscillation frequency of 1.66 Hz (100 oscillations per minute) and an oscillation amplitude of ± 0.5°.

8.18 Macromolecular Cross-Metathesis of High-*cis* Polybutadiene and Polyisoprene

Random multiblock PBR-PIR copolymers were prepared by macromolecular cross-metathesis of high-*cis* PBR-PIR 50:50 (%wt.) mixtures in dry hexane, in presence of GI and HGI catalysts. Tests were also performed on each homopolymer in presence of GI.

In a typical experiment, in glove box, equal amounts of PBR (500 mg) and PIR (500 mg) were dissolved in 40 mL of dry hexane in a septum-capped vial and GI or HGI catalysts (5 mg; 0.036 %mol. and 0.049 %mol. against the total double bond units in the main chain of polymers, respectively) were dispersed in 2 mL of dry hexane in a small vial.

The dispersion of the catalyst was then transferred to the vial containing the polymers via syringe and vigorously stirred at 45 °C for GI metathesis or 60 °C for HGI metathesis. The metathesis reaction was allowed to go for 5 min, 10 min, 15 min, 20 min, 30 min, 1h, 3h, 8h and 24h. Aliquots of the reacting mixture were sampled by syringe at each time and the reaction was stopped by adding 1 mL ethyl-vinyl ether. The obtained product was coagulated in ethanol and, finally, it was vacuum dried at 50 °C overnight. The yields of the scrambled polymers were higher than 95 %wt. from 5 min to 30 min, higher than 90 %wt. from 1h to 8h and approximately 70 %wt. at 24h. The products were also treated in a Kumagawa extractor and ethyl acetate was allowed to reflux for 12 hours to remove the soluble low molecular weight components. The soluble extracts were coagulated in methanol, isolated and then vacuum dried at 50 °C overnight. The insoluble residues were directly vacuum dried at 50 °C overnight. The yields of the insoluble residues compared with the as prepared scrambled polymers were higher than 90 %wt. at 1h, 3h, 8h and approximately 50 %wt. at 24h.

8.19 Metathetic Degradations of Polybutadiene and Polyisoprene and their Mixtures

Metathetic degradations of high-*cis* PBR-PIR 50:50 (%wt.) mixtures in dry hexane were performed by using G2 and HG2 catalysts. Tests were also performed on each homopolymer in presence of G2.

In a typical experiment, in glove box, equal amounts of PBR (500 mg) and PIR (500 mg) were dissolved in 40 mL of dry hexane in a septum-capped vial and G2 or HG2 catalysts (5 mg; 0.035 %mol. and 0.047 %mol. against the total double bond units in the main chain of polymers, respectively) were dispersed in 2 mL of dry hexane in a small vial. The dispersion of the catalyst was then transferred to the vial containing the polymers via syringe and vigorously stirred at 45 °C for G2 metathesis or 60 °C for HG2 metathesis. The metathesis reaction was allowed to go for 5 min, 10 min, 15 min, 20 min, 30 min, 1h, 3h, 8h and 24h. Aliquots of the reacting mixture were sampled by syringe at each time and the reaction was stopped by adding 1 mL ethyl-vinyl ether. The obtained product was coagulated in ethanol and, finally, it was vacuum dried at 50 °C overnight. The yields of the products were slightly higher than 50 %wt. at 5 min and 10 min and always lower than 35 %wt. at each time from 15 min to 24h.

8.20 Covalent Functionalization of Graphene Oxide Layers with Grubbs Catalyst

The following procedure was elaborated and performed in collaboration with Dr. Annaluisa Mariconda of the Department of Chemistry and Biology of the University of Salerno. Grubbs catalyst-functionalized graphite oxide powders were prepared in analogy with the procedure reported by Longo *et al.* for Grubbs catalyst-functionalized multiwalled carbon nanotubes.[7]

In a 500 mL flask, containing 6.2 g of GO powders, 300 mL of thionyl chloride were added under nitrogen and the resulting suspension was stirred for 48 h at 70 °C. The excess of thionyl chloride was evaporated under vacuum, obtaining GO-Cl powders.

20 mL of ethylene glycol and 250 mL of dry THF were added in the same flask. The mixture was stirred for 36 h at 70 °C under nitrogen. The solid product (GO-Gly) was filtered, washed with 300 mL of methanol and dried at 60 °C for 12 h in an oven.

5-norbornene-2-carboxylic acid is converted in the corresponding acid chloride. 10 mL of 5-norbornene-2-carboxylic acid and 33 mL of thionyl chloride were added in a 100 mL flask.

The mixture was stirred at reflux for 24 h under nitrogen. The excess of thionyl chloride was evaporated under vacuum.

In a 250 mL flask, containing 5.1 g of GO-Gly powders, 70 mL of dry CH_2Cl_2, 4 mL of dimethylformamide and 4 mL of triethylamine were added. The mixture was stirred under nitrogen for 48 h at reflux. The solid product (GO-Nor) was isolated by filtration, washed with 300 mL of methanol an 200 mL of CH_2Cl_2 and dried at 60 °C for 12 h in an oven. 4.8 g of GO-Nor powders were obtained.

For each covalent functionalization, 1.2 g of GO-Nor, 400 mg of G2 and 150 mL of dry hexane were added, under nitrogen, in a 250 mL flask. The mixture was stirred for 16 h, at room temperature, under nitrogen. The solid product (GO-G2) was isolated by filtration, washed with CH_2Cl_2, until the disappearance of the characteristic brownish color of the excess of G2 (roughly 500 mL of CH_2Cl_2) and dried at 60 °C for 12 h in an oven. 1.1 g of GO-G2 active powders were obtained.

8.21 Non-Covalent Functionalization of Graphene Oxide Layers with Piers Catalyst

The following procedure was elaborated and performed in collaboration with Dr. Annaluisa Mariconda of the Department of Chemistry and Biology of the University of Salerno. In a 100 mL flask containing a solution of 32 mg of PPh_3 in 30 mL of CH_2Cl_2 dry, 50 mg of second generation Piers catalyst (P2) were added under nitrogen atmosphere and stirred overnight at room temperature. Dichlorometane was then evaporated under vacuum, the phosphinated product (PP2) powders, were finally washed with dry hexane to eliminate the excess of PPh_3.

2 g of GO powders were dispersed in 400 mL 0.05 M NaOH aqueous solution and stirred for 1h at room temperature. The slurry was centrifugated at 10000 rpm for 15 min and the

precipitate was washed with deionized water and dried at 60 °C for 12 h in an oven. 1 g of $GO^{-}Na^{+}$ powders were dispersed in 50 mL of deionized water and directly added in the flask containing PP2. The mixture was homogenized for 1h under magnetic stirring and sonicated in a 5000 mL batch bath ultrasound (Badelin Sonorex RK 1028 H) for 2h at room temperature. The dispersion was centrifugated at 10000 rpm for 15 min and the precipitate was washed with deionized water and dried at 60 °C for 12 h in an oven.

8.22 Grafting of Polyisoprene to Grubbs and Piers Catalyst-Functionalized Graphene Oxides

1 g of PIR was dissolved in 40 mL of hexane, subsequently 3 %wt. of GO-G2 or GO/PP2 powders were added to the PIR solution. The mixture was stirred for 3 h at 45 °C, after it was coagulated in ethanol and, finally, vacuum dried at 50 °C overnight. The products were also treated in a Kumagawa extractor and hexane was allowed to reflux for 12 hours to remove the free (soluble fraction) from the grafted polymer fraction (insoluble residue). The soluble extracts were coagulated in methanol, isolated and then vacuum dried at 50 °C overnight. The insoluble residues were directly vacuum dried at 50 °C overnight. The yields of the dried insoluble residues compared with the as prepared grafted rubbers were higher than 95 %wt. and 97 %wt. for PIR/GO composites obtained from GO-G2 and GO/PP2, respectively.

References

[1] A. Grassi, C. Pellecchia, P. Longo, A. Zambelli. *Gazzetta Chimica Italiana* **1987**, *117*, 249–250.

[2] L. Staudenmaier. *Ber. Dtsch. Chem. Ges.* **1898**, *31*, 1481–1487.

[3] W. S. Hummers, R. E. Offeman. *J. Am. Chem. Soc.* **1958**, *80*,

1339.

[4] Y. Matsuo, T. Niwa, Y. Sugie. *Carbon* **1999**, *37*, 897–901.

[5] S. Stankovich, D. A. Dikin, R. D. Piner, K. A. Kohlhaas, A. Kleinhammes, Y. Jia, Y. Wu, S. T. Nguyen, R. S. Ruoff. *Carbon* **2007**, *45*, 1558–1565.

[6] R. Wissert, P. Steurer, S. Schopp, R. Thomann, R. Mülhaupt. *Macromol. Mater. Eng.* **2010**, *295*, 1107–1115.

[7] C. Costabile, F. Grisi, G. Siniscalchi, P. Longo, M. Sarno, D. Sannino, C. Leone, P. Ciambelli. *J. Nanosci. Nanotech.* **2011**, *11*, 1–10.

Chapter 9

Characterization Techniques

9.1 Wide Angle X-ray Diffraction

Wide-angle X-ray diffraction (WAXD) patterns were obtained by an automatic Bruker D8 Advance diffractometer, in reflection, at 35 KV and 40 mA, using the nickel filtered Cu Kα radiation (1.5418 Å). The *d*-spacings were calculated using Bragg's law and the observed integral breadths (β_{obs}) were determined by a fit with a Lorentzian function of the intensity corrected diffraction patterns, according to the procedure described by Iwashita *et al.* [1] The instrumental broadening (β_{inst}) was also determined by fitting of Lorentzian function to line profiles of a standard silicon powder 325 mesh (99%). For each observed reflection, the corrected integral breadths were determined by subtracting the instrumental broadening of the closest silicon reflection from the observed integral breadths, $\beta = \beta_{obs} - \beta_{inst}$. The correlation lengths perpendicular to hkℓ planes ($D_{hk\ell}$) were determined using Scherrer's equation.

$$D_{hk\ell} = \frac{K\lambda}{\beta_{hk\ell} \cos \theta_{hk\ell}} \tag{1}$$

where λ is the wavelength of the incident X-rays and $\theta_{hk\ell}$ the diffraction angle, assuming the Scherrer constant $K = 1$.

A more accurate WAXD analysis was carried out for samples A-F of **Fig. 2.8**. The correlation lengths (D) and the lattice strains (ε) were estimated by applying the Williamson and Hall method,[2] which was successfully applied to carbon materials.[3–5]

$$\frac{(\beta_{obs}-\beta_{inst})}{\lambda}\cos\theta=\frac{K}{D}+2\varepsilon\left(\frac{2\sin\theta}{\lambda}\right) \qquad (2)$$

The out-of-plane correlation lengths ($D_{\perp}$) and lattice strains ($\varepsilon_{\perp}$) were obtained using the 002, 004, 112 and 006 reflections, while the in-plane correlation lengths ($D_{\parallel}$) and lattice strains ($\varepsilon_{\parallel}$) were determined from the 100 and 110 reflections. The shape anisotropy was determined by the ratio $D_{\parallel}$ / $D_{\perp}$, while the strain anisotropy was evaluated by the ratio $\varepsilon_{\perp} / \varepsilon_{\parallel}$.

WAXD measurements were also obtained with an automatic Philips powder diffractometer, in transmission, by using a cylindrical camera (radius = 57.3 mm). The WAXD patterns of GO and GOIC films of **Fig. 2.18** were recorded on a BAS-MS imaging plate (FUJIFILM) and processed with a digital imaging reader (FUJIBAS 1800). In particular, to recognize the kind of crystalline orientation present in films, photographic X-ray diffraction patterns were taken by placing the film sample parallel to the axis of the cylindrical camera and by sending the X-ray beam parallel (EDGE measure) to the film surface.

The degree of the different kinds of uniplanar orientation of the crystallites with respect to the film plane has been formalized on a quantitative numerical basis using Hermans' orientation functions, in analogy to that one defined for the axial orientation:

$$f_{hkl}=(3\overline{\cos^2 x_{hkl}}-1)/2 \qquad (3)$$

by assuming $\overline{\cos^2\chi_{hkl}}$ as the squared average cosine value of the angle, x_{hkl}, between the normal to the film surface and the normal to the hkℓ crystallographic plane.[6–8]

Since, in our cases, a $\theta_{hk\ell}$ incidence of X-ray beam is used, the quantity $\overline{\cos^2 \chi_{hkl}}$ can be easily experimentally evaluated:

$$\overline{\cos^2 x_{hkl}} = \overline{\cos^2 \chi_{hkl}} = \frac{\int_0^{\pi/2} I(\chi_{hkl}) \cos^2 \chi_{hkl} \sin \chi_{hkl} d\chi_{hkl}}{\int_0^{\pi/2} I(\chi_{hkl}) \sin \chi_{hkl} d\chi_{hkl}} \qquad (4)$$

where $I(\chi_{hkl})$ is the intensity distribution of a hkℓ diffraction on the Debye ring and χ_{hkl} is the azimuthal angle measured from the equator.

The diffracted intensities $I(\chi_{hkl})$ of eq. 4 were obtained by EDGE patterns, as collected by using a cylindrical camera, by the azimuthal profile at a constant 2θ value. Because the collection was performed at constant 2θ values and in the equatorial geometry, the Lorentz and polarization corrections were unnecessary.

In these assumptions, f_{hkl} is equal to 1 and -0.5 if hkℓ planes of all crystallites are perfectly parallel and perpendicular to the plane of the film, respectively.

9.2 Fourier Trasform Infrared Spectroscopy

Fourier transform infrared spectra (FTIR) spectra in transmission mode with 2.0 cm^{-1} resolution, were recorded with a BRUKER Vertex70 spectrometer equipped with a deuterated triglycine sulfate (DTGS) detector and a KBr beam splitter. The powder specimens were diluted with KBr of spectroscopic grade. The frequency scale was internally calibrated to 0.01 cm^{-1} with a He-Ne laser and the noise was reduced by signal averaging 32 scans.

9.3 Differential Scanning Calorimetry

The differential scanning calorimetry (DSC) was carried out under nitrogen in the suitable temperature range for each material at a heating or cooling rate of 10 °C/min on a TA instruments DSC 2920. Two heating and one cooling run were consecutively carried out in a cycle and the peak maxima were considered as the transition temperatures.

9.4 Thermogravimetric Analysis

Thermogravimetric analysis (TGA) of the layered nanofillers was carried out on a TG 209 F1, manufactured by Netzsch Geraetebau, from 20 to 800 °C, at a heating rate of 10 °C, under N_2 flow. TGA curves were also obtained for scrambled rubber samples, Grubbs catalyst-functionalized graphene oxides and grafted rubbers to graphene oxide sheets from 20 to 1000 °C, at a heating rate of 10 °C, under air flow.

9.5 Elemental Analysis

Elemental analysis was performed with a Thermo FlashEA 1112 Series CHNS-O analyzer, after pretreating samples in an oven at 100 °C for 12 h, in order to remove the absorbed water.

9.6 BET Surface Area Measurements

Nitrogen adsorption at liquid nitrogen temperature (-196 °C) was used to measure surface areas of the samples with a Nova Quantachrome 4200e instrument. Before the adsorption measurement, clay and carbon-based powders were degassed at 100 °C under nitrogen flow overnight to remove water, while polymeric aerogels were degassed at 40 °C, in the same conditions. The surface area values were determined by using 11-point Braunauer-Emmett-Teller (BET) analysis.[9] All measures were performed in collaboration with Dr. Simona Longo of the Department of

Chemistry and Biology of the University of Salerno.

9.7 Scanning Electron Microscopy

The morphology of the samples was characterized by means of a scanning electron microscope (SEM, Zeiss Evo50 equipped with an Oxford energy dispersive X-ray detector). Low energy was used (5 keV) to obtain the highest possible surface resolution. Before imaging, all specimens were coated with gold using a VCR high resolution indirect ion-beam sputtering system. The coating procedure was necessary to prevent surface charging during measurement and to increase the image resolution.

9.8 Trasmission Electron Microscopy

TEM analysis on rubber nanocomposites was performed by Dr. Lucia Conzatti at the CNR, Institute for Macomolecular Studies (ISMAC)-UOS Genova with a Zeiss EM 900 microscope applying an accelerating voltage of 80 kV. Ultrathin sections (about 50 nm thick) of cross-linked specimens were obtained by using a Leica EM FCS cryo-ultramicrotome equipped with a diamond knife (sample temperature: –130 °C). Before the TEM analysis, eGO samples were dispersed and sonicated in isopropanol, then 10 μL of the dispersion were were deposited on Assing copper grids coated with carbon film.

9.9 Back Titration of Graphite Oxides

The cation-exchange-capacity of the GO samples (CEC) was determined by the back titration of sodium hydroxide solution (0.05 M, 50 ml) of GO (100 mg) by 0.05 M hydrochloric acid solution, according to the procedure reported by Matsuo *et al.* [10]

9.10 Gel Permeation Chromatography

Gel permeation chromatography (GPC) was performed with a

Waters Breeze GPC system was equipped with a refractive index (RI) detector using a set consisting of four Styragel HT columns with (10^2, 10^3, 10^4, and 10^5 Å pore size) and 10 μm (particle size). THF was used as eluent at 35 °C at a flow rate of 1.0 mL min^{-1}. The calibration curve was established with polystyrene standards.

9.11 NMR Spectroscopy

^{13}C-NMR spectra were recorded by using a Bruker AVANCE 400 spectrometer (400 MHz for ^1H and 100 MHz for ^{13}C). The chemical shifts were referenced to tetramethylsilane (TMS) ($\delta = 0$ ppm) using the residual proton impurities of the deuterated solvents as internal standards. Rubber samples were prepared by dissolving 100 mg of compound in 2 mL of deuterated chloroform ($CDCl_3$). ^1H-NMR spectra of P2 and PP2 catalysts in deuterated dichloromethane (CD_2Cl_2) were also recorded.

9.12 Raman Spectroscopy

The Raman characterization was performed by the group of Dr. Pellegrino Musto at the CNR, Institute of Chemistry and Technology of Polymers (ICTP) Pozzuoli. Raman spectra were obtained by a confocal Raman (HORIBA Jobin Yvon LabRAM Aramis) microscope, equipped with a He-Ne laser at a wavelenght of 633 nm. Raman spectra of samples in **Fig. 2.25** were fitted with Lorentzian functions for the D, G and D'-band, in order to estimate the full width at half maximum of the D-band ($FWHM_D$), chosen as the in-plane structural ordering parameter.[11]

9.13 Dynamic-Mechanical Analysis

Dynamic-mechanical properties of sPS/OC aerogels were studied using a Triton dynamic-mechanical thermal analyzer. The spectra were recorded in the three-point bending mode, on samples with the following dimensions: length 15 mm, width 10 mm and thickness 2 mm. The storage modulus was obtained, as a function of temperature, at a frequency of 1 Hz and an amplitude of 0.03 mm. The heating rate was 2 °C/min in the range of 0, +100 °C.

The tensile storage modulus and the loss tangents of PIR/GO nanocomposites were determined via dynamic-mechanical analysis at a frequency of 1 Hz and an amplitude of 0.03 mm. The spectra were recorded in the tensile mode from -90 °C to -20 °C, with a heating rate of 2 °C/min.

9.14 Tensile Tests

Tensile tests were performed by the group of Prof. Maurizio Galimberti at the Polytechnic of Milan with ISO 3 dumbbell. Composites were homogeneized by passing them at the two roll mill at 40 °C, for 10 times. Disks 2 mm thick and with 56 mm as the diameter were obtained therefrom by vulcanizing the composites for 20 minutes at 170 °C with 150 bar pressure. Dumbbell, 2 mm thick, 8.5 mm wide, 50 mm long and with 15 mm as the distance between the grips were then taken from these disks. Tensile tests were performed at Room Temperature by an Instron dynamometer (model 3366) on three dumbbells at cross-head rate of 100 mm/min.

9.15 Strain Sweep Tests

A Monsanto R.P.A. 2000 rheometer was used to measure dynamic mechanical properties of the rubber nanocomposites. All measures were performed by the group of Prof. Maurizio Galimberti at the Polytechnic of Milan. The adopted experimental procedure is described as follows. Raw samples were kept in the instrument at 50 °C for 90 s, a strain sweep (0.1 - 100% strain) was then performed at 50 °C. Afterwards, the curing was carried out at 170 °C for 20 min, with a frequency of 1.667 Hz and an angle of 6.98% (0.5 rad). The cured samples were allowed to recover in the instrument for

180 min at 50 °C. Data were finally obtained with a strain sweep (0.1 - 100% strain) performed at 50 °C with a frequency of 1 Hz.

9.16 Crosslinking Tests

The behavior of the crosslinking reaction of the rubber nanocomposites was studied at 170 °C with a Monsanto oscillating disc rheometer MDR 2000 (Alpha Technologies, Swindon, UK). All measures were performed by the group of Prof. Maurizio Galimberti at the Polytechnic of Milan.

References

[1] N. Iwashita, C. R. Park, H. Fujimoto, M. Shiraishi, M. Inagaki. *Carbon* **2004**, *42*, 701–714.

[2] F. Williamson, W. Hall. *Acta Metall.* **1953**, *1*, 22–31.

[3] T. Ungár, J. Gubicza, G. Tichy, C. Pantea, T. W. Zerda. *Composites Part A* **2005**, *36*, 431–436.

[4] D. Poirier, R. Gauvin, R. A. L. Drew. *Composites Part A* **2009**, *40*, 1482–1489.

[5] S. A. Manafi, M. H. Amin, M. R. Rahimipour, E. Salahi, A. Kazemzadeh. *Nanoscale Res. Lett.* **2009**, *4*, 296–302.

[6] R. J. Samuels. In Structured polymer properties, New York: John Wiley & Sons; **1971**, Chapter 2, p. 28.

[7] M. Kakudo, N. Kasai. X-ray diffraction by polymers, Amsterdam: Elsevier; **1972**, Chapter 10, p. 252.

[8] L. E. Alexander. In X-ray diffraction methods in polymer science, New York: Krieger RE, editor; **1979**, Chapter 4, p. 210.

[9] S. Brunauer, P. H. Emmett , E. Teller. *J. Am. Chem. Soc.*, **1938**, *60*, 309–319.

[10] Y. Matsuo, T. Miyabe, T. Fukutsuka, Y. Sugie. *Carbon* **2007**, *45*, 1005–1012.

[11] J. M. Vallerot, X. Bourrat, A. Mouchon, G. Chollon. *Carbon* **2006**, *44*, 1833–1844.

Conclusions

In a nutshell, new layered nanofillers for rubber nanocomposites, based on clays and graphitic materials, were prepared and deeply characterized. Pristine MMT and a graphite G with high surface area, also exhibiting a high shape anisotropy, were selected as the starting materials. GO samples were obtained by oxidation of G with both Staudenmaier and Hummers methods. A complete control over the degree of order and the periodicity of the nanofiller structures was achieved.

First of all, the intercalation chemistry of MMT and GO with long-chain amphiphilic guest molecules was investigated in order to obtain properly modified fillers with improved compatibility with the rubber matrix. Two different procedures were adopted: the solid state preparation of OCs was performed in a centrifugal ball mill, while GOICs were prepared with the help of water and ethanol. Ordered OC and GOIC structures with bulky guest molecules and with large interlayer spacings, also exhibiting a high crystalline order in the interlayer space were obtained, in absence or in presence of polar long-chain co-intercalants.

Disordered structures were also obtained at the solid state by using different methods. In particular, exfoliation of OCs was induced by supercritical CO_2 treatments, while chemically modified graphenes were prepared in bulk quantities by chemical, mechanical and solvo-thermal treatments of GO powders. Furthermore, monolithic sPS aerogels filled with exfoliated clays or graphenes were found to preserve the exfoliation state of the fillers and, due to their thermoplastic nature, are proposed as masterbatches for composite processing.

Rubber nanocomposites were prepared by melt blending PIR with OCs or GOICs. Results obtained for rubber/OC nanocomposites confirmed that only low molecular mass substances, such as the compensating cations and, optionally, further polar molecules, are intercalated in the clay interlayer space, being the intercalation of hydrophobic polymer chains highly unlikely to occur. The GOICs were evenly dispersed in the PIR matrix and were found to be prevailingly exfoliated. OCs and GOICs exhibited reversible thermal transitions, both at the solid state and in the rubber matrix, corresponding to the recovery and the loss of the order in the packing of long hydrocarbon tails of the compensating cation associated to each lamella. Tensile and dynamic-mechanical properties of the nanocomposites were appreciably affected by the nanofiller structures, namely by the interlayer distance. However, a larger amount of the long hydrocarbon chains did not lead to a substantial increase of mechanical reinforcement: the long hydrocarbon chains seem to act as plasticizer, compensating the reinforcing effect of the nanofiller layers.

Metathesis reactions were used to prepare innovative polymer-polymer and filler-polymer materials, containing rubber macromolecules. High-*cis* random multiblock PBR-PIR copolymers were successfully prepared by MCM with first generation Grubbs and Hoveyda-Grubbs catalysts in dry hexane, while second generation Grubbs and Hoveyda-Grubbs catalysts were found to preferentially degradate rubbers. Finally, novel rubber nanocomposites, composed by PIR grafted to graphene oxide sheets, were prepared by taking advantage from the cross-metathesis reactions of PIR and functionalized GO samples with Grubbs and Piers catalysts.

Acknowledgements

These three years I have spent at the University of Salerno have been a wonderful part of my life and here, I would like to distinguish and express my special thanks:

To my tutor Prof. Gaetano Guerra, for the effective guidance, support and encouragement during the entire work. He always taught me how much imagination and willfulness can be important to get good results, I will never forget his passion for one of the most beautiful jobs ever existed, the scientific research.

To Prof. Pasquale Longo, Prof. Maurizio Galimberti, Dr. Luca Giannini, Dr. Thomas Hanel and Dr. Angela Lostritto for generously giving precious advices and for sharing ideas and research activities.

To my family, who guided me in all my choices, enjoying all my successes. I owe a great deal to them for the person that I'm today.

To Sheila for the love that we share everyday of our lives. She came into my life as a hurricane, filling my days with her brightness, intelligence and beauty. She has always supported me in good and bad times, giving me the strength and the motivations to go on and to make my best.

To Mario Maggio and Simona Daniele for the commitment and dedication that they have shown during their graduation thesis under my supervision.

I truly thank all the guys of my research group, Antonio Avallone, Simona Longo, Graziella Ianniello, M. Rosaria Acocella, with whom I have established a friendship beyond the employment relationship and all the people I have met in the laboratories, Alessandra Perfetto, Annaluisa Mariconda, Antonio Buonerba and Carmen Talotta, particularly Annarita Noschese and Assunta De Nisi for the funny lunch times.

Finally, I would like to thank the guys from the Polytechnic of Milan, Valeria Cipolletti, Sara Musto and Vineet Kumar for useful discussions.

A dreamer is one who can only find his way by moonlight, and his punishment is that he sees the dawn before the rest of the world.

Oscar Wilde